PNNL-28362

Pacific Northwest
NATIONAL LABORATORY
Proudly Operated by Battelle Since 1965

Ultrasound Modeling and Simulation: Status Update

December 2018

Gerges Dib
Michael R. Larche
Matthew S. Prowant
Richard E. Jacob
Pradeep Ramuhalli
Aaron A. Diaz

NRC Program Manager: Carol A. Nove

Prepared for the U.S. Nuclear Regulatory Commission
under a Related Services Agreement with the U.S. Department of Energy
CONTRACT DE-AC05-76RL01830

U.S. DEPARTMENT OF ENERGY

PACIFIC NORTHWEST NATIONAL LABORATORY
operated by
BATTELLE
for the
UNITED STATES DEPARTMENT OF ENERGY
under Contract DE-AC05-76RL01830

PNNL-28362

Ultrasound Modeling and Simulation: Status Update

Gerges Dib
Michael R. Larche
Matthew S. Prowant
Richard E. Jacob
Pradeep Ramuhalli
Aaron A. Diaz

December 2018

NRC Program Manager: Carol A. Nove

Prepared for
the U.S. Nuclear Regulatory Commission
under a Related Services Agreement
with the U.S. Department of Energy
Contract DE-AC05-76RL01830

Pacific Northwest National Laboratory
Richland, Washington 99352

Summary

The Pacific Northwest National Laboratory (PNNL) is conducting confirmatory research for the U.S. Nuclear Regulatory Commission for establishing standard methods of modeling and simulation to assess the effectiveness and reliability of ultrasonic inspections of nuclear power plant (NPP) components. This work is part of an ongoing effort to define best practices required for using computational models for ultrasonic testing (UT) reliability applications. In addition to model validity (i.e., the ability of a model to accurately reproduce all conditions of interest for a particular application), a number of other factors need to be taken into account, such as computational complexity, uncertainty in model predictions, and the ability to extrapolate findings from model predictions to realistic scenarios. In this part of the ongoing effort, we focus on beam modeling and evaluating the use of both beam models and flaw models for simulating weld inspections. We evaluate the dynamic ray tracing model capability for handling smoothly varying heterogeneous materials, as this approach is often applied for simulating UT behavior in weld geometries.

Two types of beam models based on two commercial simulation software platforms common to the NDE nuclear industry, CIVA and UltraVision, are compared. The two software platforms implement different approaches to modeling the ultrasound beam, and this assessment assumes correctness of the implementation. Differences observed in the computed beam between the two software platforms are not surprising, given that different types of models are being compared. The dynamic ray tracing model (CIVA implementation of beam models) is used to evaluate beam simulation of austenitic weld inspection. This is done by attempting to reproduce empirically measured sound beams using simulations. Challenges in this approach are seen due to the complexity of weld modeling and the large number of parameters required to define welds.

The correlation between beam amplitude incident onto flaws and the expected response amplitude from the flaw is also investigated. Beam simulations using 23 different types of single- and dual-element probes are used to extract an amplitude metric representing the sound beam amplitude incident onto flaws of different dimensions. Then, this metric is compared with the maximum expected response amplitudes from circumferentially oriented crack-like flaws of different depths. This study shows the complex relationship between flaw scattering and incident beams, thus limiting the interpretability of beam simulations for NDE reliability. Different types of normalizations and methods to quantify access limitations are also considered in this study.

To further understand the ability to use flaw models to simulate ultrasonic weld inspection, a welded specimen with a machined reflector (saw-cut flaw) was scanned using different types of transducers. Those measurements are compared with simulated results using the dynamic ray tracing model in CIVA. This work illustrates the importance and the necessity for requiring well characterized weld properties as model inputs.

Finally, initial work in transducer characterization is conducted to illustrate the possible variations in performance of transducers that have similar specifications. This study shows that even with the same transducer specifications and manufacturers, the frequency response and near-field distance of transducers can vary significantly. This variance is likely to have a direct effect on signal-to-noise ratio and must be taken into account when conducting model-based studies of ultrasonic inspections.

Acknowledgments

The work reported here was sponsored by the U.S. Nuclear Regulatory Commission (NRC) under Pacific Northwest National Laboratory (PNNL) Project No. 70555 (NRC-HQ-60-17-D-0010). Ms. Carol Nove is the NRC Contracting Officer Representative and Program Manager. PNNL would like to thank Ms. Nove for her guidance and technical direction over the course of this work and for providing a technical review of the contents of this technical letter report. The authors also thank Ms. Kay Hass for her assistance in technical editing of this document, and the peer reviewers for their feedback on the contents.

PNNL is operated by Battelle for the U.S. Department of Energy under Contract DE-AC05-76RL01830.

Acronyms and Abbreviations

ASME	The American Society of Mechanical Engineers
BW	bandwidth
CASS	cast austenitic stainless steel
FDM	finite difference method
FEM	finite element method
FFT	fast Fourier transform
GTD	geometric theory of diffraction
ISI	inservice inspection
MINA	Modelling Anisotropy from Notebook of Arc Welding
NDE	nondestructive examination/evaluation
NPP	nuclear power plant
NRC	U.S. Nuclear Regulatory Commission
NRR	Office of Nuclear Reactor Regulation
PAUT	phased array ultrasonic testing
PNNL	Pacific Northwest National Laboratory
RF	radio frequency
SNR	signal-to-noise ratio
TRL	transmit-receive longitudinal
UT	ultrasonic testing
UV	UltraVision
WSS	wrought stainless steel

Contents

Figures

Tables

1.0 Introduction

Computer modeling and simulation has the potential for providing a cost- and time-effective alternative to experiments for evaluating the reliability of ultrasonic inspections. Computer simulations are idealized representations of ultrasonic wave generation, propagation, and interaction with discontinuities in materials. The idealized models are approximations that do not capture all of the complexity of the physics of ultrasound, but are often sufficient for the purposes of explaining empirical results.

Two approaches for modeling have traditionally been used in ultrasonic nondestructive examination/evaluation (NDE). Beam models allow visualization of energy propagation from a specific transducer within a given geometry. Beam models usually require less computational time and allow one to directly visualize the simulated sound field to understand how it propagates within the material (Rose 2004). In addition, beam models provide information (energy distribution within a 3D volume with potentially complex microstructures), which is often hard to obtain by experiment. Thus, beam models may be seen as complementary to empirical measurements, especially for probe design. However, such models do not show how the sound field interacts with geometrical features and defects that might be present within the material.

Flaw response models, on the other hand, compute the result of ultrasound beam interactions with flaws in materials while accounting for specimen boundaries. The results are represented as the radio frequency (RF) signal response received by a search unit at each scan location. While these models are capable of simulating the response from flaws and geometrical features, they usually require longer computational times than beam models. Therefore, flaw response models may be useful for replacing experiments for assessing and qualifying ultrasonic testing methods.

It is important to keep in mind that several key factors that may limit the reliability of ultrasonic testing are often difficult to represent or not represented at all in models and simulations. For instance, microstructural anisotropy and material noise can only be approximated in simulation models, while measurement noise and human factors are not incorporated into ultrasonic models. The result of these approximations and omissions become sources for potential uncertainties in interpreting the results of ultrasonic models.

As a result, there is a need for establishing standard methods of applying modeling results to assess the effectiveness of ultrasonic inspection of nuclear power plant (NPP) components. The effectiveness of an inspection requires identification of the signal from a flaw in the material and whether such a signal can be distinguished above the noise background.

This technical letter report describes the most recent research findings from technical evaluations conducted at the Pacific Northwest National Laboratory (PNNL) to begin to address these needs.

1.1 Objectives

The primary objectives of the work described in this report were to evaluate the effectiveness of beam models with respect to quantifying volumetric coverage and flaw detection capability, and to evaluate both beam models and flaw response models for simulating welded geometries. Included in the evaluation was the identification of key variables in typical simulation models that influence coverage extent and flaw detection capability.

Several factors may influence the effectiveness of such models and include:

- Material anisotropy in weld materials and the consequent variations in beam propagation paths.
- Applicability of beam models to assess flaw detection capability, based on beam amplitude thresholds and flaw specular reflection amplitudes at different probe positions.
- Potential metrics to assess coverage extent from ultrasonic beam models in isotropic and anisotropic (weld) materials.

It is important to realize that complete, 100% volumetric coverage may not correlate with the ability to detect all flaws in the covered volume. The work described in this report attempts to quantify the correlation between ultrasonic beam characteristics as established using simulation models, and both the simulated and empirically measured responses from flaws using different materials and inspection parameters.

The work described in this report is a step toward establishing standard methods of applying simulation models to assess the effectiveness of inspections of NPP components and will inform the development of guidance documents for conducting, interpreting and applying the results of ultrasonic modeling within the context of ultrasonic inspections of Class 1 components in NPPs. We expect that insights from this research, once completed, will help determine best practices for the use of ultrasound models of specular and diffracted flaw responses to assess flaw detection capability (incorporating model uncertainty, model error, and expected experimentation errors and variations). We also expect that the research will help identify strengths and weaknesses in common ultrasonic models that may be used in 2D and 3D simulation of ultrasonic inspection and quantify the information required to verify results obtained from simulation models.

Note that we distinguish between the terms “model” and “simulation.” Models are mathematical representations (approximations) of the physics of ultrasound propagation and interaction in materials. We define a simulation as the instance of running a model using a software implementation (commercially available or research-grade) with a specific set of input parameters and boundary conditions. Because of model approximations and potential implementation errors, simulation results are not expected to be exact representations of reality.

In this report, we identify and address three key areas for modeling and simulation:

- Evaluate the relevant information that beam models provide, especially with regard to insonification levels and volumetric coverage.
- Evaluate different approaches for modeling welds, and conduct a validation study to evaluate accuracy of current state-of-the-art, semi-analytical models for weld representation.
- Provide a methodology for using flaw response models for model-assisted investigation of parameters influencing in-field examination reliability.

1.2 Report Organization

Section 2.0 of this technical report provides an overview of modeling and previous work at PNNL and elsewhere. Section 3.0 provides a comparison of different commercial tools for computing beam models, with the goal of determining the variance in computed results from different tools. Section 4.0 discusses beam models and measurements in austenitic welds, while Section 5.0 describes research for quantifying correlations between beam metrics and

flaw responses for the purposes of quantifying flaw detection capability from beam models. Section 6.0 expands the research described in Section 5.0 to flaws in the vicinity of austenitic welds. Section 7.0 describes initial research toward quantifying the variability in inspection parameters in the field with a focus on transducer performance variability. This variability will need to be accounted for in simulations if a realistic assessment of ultrasonic inspection effectiveness is to be obtained from simulations. Finally, Section 8.0 summarizes the research to date, draws conclusions, and describes ongoing and planned future research in this technical area. Section 9.0 lists references cited in this report.

2.0 Background and Previous Work

Ultrasound modeling and simulation for ultrasonic testing (UT) of NPP components provides insight about sound field propagation and expected backscatter from flaws of interest. Simulations have the potential to be an essential complementary tool for personnel when examining complex geometries or using advanced sensors such as phased arrays for providing insight into understanding the dynamics within those complex scenarios. In this section, an overview of the theoretical aspects of ultrasound modeling is provided, and a few commonly used models for simulating ultrasound propagation and ultrasound interaction of discontinuities (i.e., flaws) are described.

2.1 Overview of Modeling

Linear wave propagation in solids and fluids is described by the wave equation. The solutions of the wave equation give particle displacements at all positions and times within a propagation medium and, hence, all the wave propagation characteristics. Analytic solutions to the wave equation in complex structures are not known, and computational methods are needed to describe wave propagation in these structures. Approaches to compute wave dynamics in complex structures are based on standard numerical solutions to the wave equation, such as the finite difference method (FDM) and the finite element method (FEM). These approaches solve the complete wave field in the structure and provide an exact solution to the wave equation if the computation is based on sufficiently high time and spatial resolutions. It is well known that FEM and FDM become more computationally expensive as the model geometry size increases via a required increase in the number of elementary computational domains or as the frequency increases (Bathe 2014) via a required increase in the time-step resolution. Using such methods to accurately model typical UT inspections (frequencies up to 5 MHz, thousands of scan points, multiphysics, and geometries larger than 164 cm^3 [10 $in.^3$]) are prohibitively expensive using standard computer processing units. With the advent of graphics processing units (GPUs) for solving linear equations, specialized software for wave-field propagation has been developed and optimized for use with GPUs (e.g., Pogo, Huthwaite 2014; SpecFEM3D, CIG 2015).

Due to the prohibitive computation cost of FEM and FDM methods, the UT modeling community has focused on approximate high-frequency modeling techniques. High-frequency approximations are appropriate for most conventional inspection techniques used in UT, because examination wavelengths are typically smaller than flaws and geometrical features of interest.

The most common approximation technique is based on asymptotic ray theory (Červený 2001), which models ultrasound waves as straight lines (rays) emanating from a transducer source. A limitation of this approach is that changes between multiple interfaces should be smooth, with large changes in material properties or interface shapes being undesirable (Brokešová 2006). Another important limitation is that it only solves for direct-wave rays emanating from a source. This differs from FEM/FDM methods, which solve the complete wave field and its interaction with material features and defects. When using the asymptotic ray model, special care must be taken when computing all possible reflections from specimen boundaries or interfaces. Asymptotic ray theory is the basis for CIVA software (EXTENDE S.A., Massey, France) commonly used within the NDE nuclear industry (Calmon et al. 2006).

Another high-frequency approximation of the wave equation is the multi-Gaussian beam model (Jeonga and Schmerr 2007; Schmerr Jr. and Song 2007). The multi-Gaussian beam model is an approximate paraxial solution to wave propagation, which assumes that the wave diverges only by a small angle relative to the normal to the transducer surface. Thus, its accuracy decreases as one moves away from the direct line along the transducer center. This model type has been the basis for the UTSim software being developed by Iowa State University (ISU 2018).

Beam models allow the visualization of the ultrasound beam as it propagates in a medium, but they do not account for the interaction of the beam with complex boundaries such as a flaw. The two most common flaw response models are the Kirchhoff approximation, which is an integral solution of wave scattering from a flaw (Schmerr Jr. and Song 2007), and the geometric theory of diffraction (GTD) (Keller 1962; Darmon et al. 2013), used to compute diffraction from flaw tips. The reduced accuracy of the Kirchhoff approximation when computing specular echoes from rough flaws or for beams with high incident angles is well studied in the literature (Ogilvy 1986; Thorsos 1988; Shi et al. 2015).

A major challenge for ultrasound modeling is the ability to compute the wave field as it propagates through complex microstructures. Such microstructures occur in coarse-grained materials such as cast austenitic stainless steel (CASS) and in austenitic welds commonly encountered in NPPs. Of particular interest for NPP inservice inspection (ISI) is wave propagation in austenitic welds and the resulting interaction of the ultrasound wave with flaws that may exist near the weld.

2.2 Wave Propagation in Austenitic Welds

Austenitic welds are commonly used in NPP piping and are a challenging medium for UT due to their anisotropic nature. As such, there has been significant interest in developing models for these types of materials. From the perspective of modeling, they introduce complexity in defining their geometrical shape, material properties, and heterogeneous microstructures.

The cooling solidification process in welding results in coarse-grain dendritic structures such as those illustrated in Figure 2.1, preferentially oriented perpendicular to the heat dissipation direction. This preferred dendrite growth direction results in elastic anisotropy, and the boundaries between the dendritic structures result in heterogeneous grains where the crystallographic direction changes within each grain. This weld structure results in attenuation that varies with wave propagation direction. In addition, effects of attenuation are increased due to the ultrasound beam being bent, or redirected, along the ultrasonic wave propagation direction with the highest wave velocity (Kupperman and Reimann 1980).

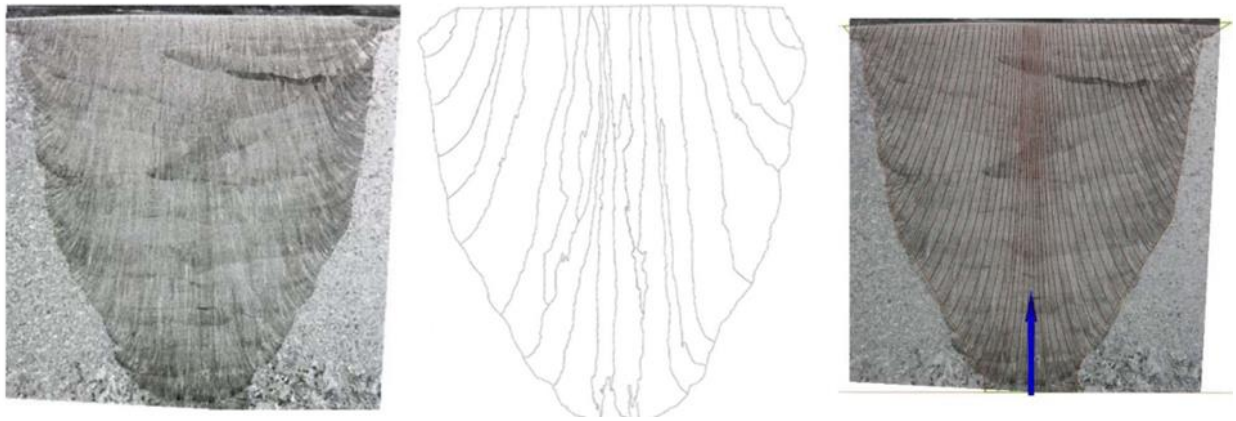

Figure 2.1. Macrograph showing the dendrites within a weld (*left*), the dendrites boundaries defining multiple homogeneous regions of the weld (*middle*), and parametric definition of continuously changing domains (*right*). The parametric definition (right figure) requires a reference coordinate system, as indicated by the blue arrow.

Several studies developed techniques to measure the anisotropic stiffness matrix of dendrites within the austenitic welds (Kupperman and Reimann 1980; Chassignole et al. 2000; Sakamoto et al. 2012). Knowledge of the stiffness matrix, which represents the elastic material properties as a function of crystalline direction, is required for complete ultrasound model specification for welds and other anisotropic materials. In anisotropic materials in general, pure longitudinal and transverse (shear) wave modes (orthogonally polarized wave modes) will not exist. Instead, the wave modes are usually quasi-longitudinal and quasi-transverse (Rokhlin et al. 1986). The effects of anisotropy on the propagation of these wave modes is represented by slowness curves, which describe the changes in the inverse of wave velocity (termed slowness) with orientation. In anisotropic materials, the quasi-longitudinal wave mode refers to the wave mode with the highest velocity, and quasi-transverse refers to the slower wave modes. Figure 2.2 shows an example of the slowness curves for stainless steel. As seen from these curves, the quasi-longitudinal (QL) wave mode shows nearly isotropic behavior with weak dependence on propagation direction relative to crystallographic orientation (a nearly circular slowness curve). The second quasi-transverse mode (vertical shear wave mode QT2) shows a more significant dependence on direction. These curves are used in simulations to represent the effects of anisotropy on wave propagation and reflection/refraction at boundaries.

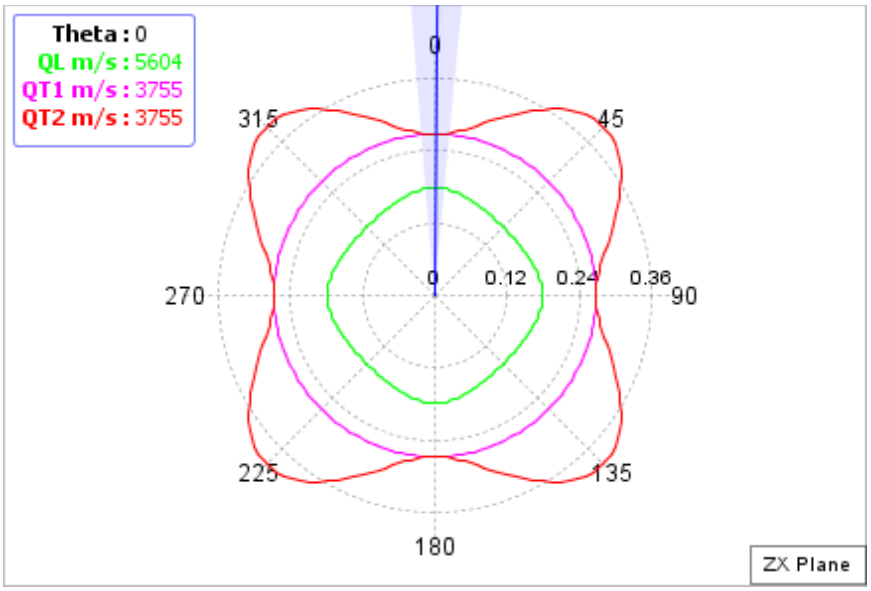

Figure 2.2. Slowness curves for steel with cubic symmetry. The green curve shows the quasi-longitudinal (QL) wave model (least slow mode), and the other two modes are the quasi-transverse wave modes. In this polar plot, the angle is the propagation direction, and the radial axis is the wave velocity.

In addition to measuring the anisotropic properties of the weld dendrites, another requirement for modeling welds is to use the appropriate representation of heterogeneity. Two common approaches for this are described here.

In the first approach, the weld is represented as a set of homogeneous domains, which can be traced by edge detection using weld macrographs such as the one shown in Figure 2.1. Gardahaut et al. (2012) use image processing of the macrographs to estimate the dendritic homogeneous regions and their orientations. Another technique called MINA (Modelling Anisotropy from Notebook of Arc Welding) incorporates crystalline growth models, information contained in the welding report, and macrographic images and microstructural imaging such as electron back-scattered diffraction to obtain accurate estimates of weld microstructure parameters (Moysan et al. 2003; Moysan et al. 2012). Ray models or finite element models can then be used to compute ultrasound propagation through these regions. Beam refraction, reflection, and the specified domains' boundaries would then control the extent to which the overall weld microstructure affects ultrasound propagation. A limitation of this approach is that the defined homogeneous domains must have dimensions larger than the minimum wavelength when used with ultrasound ray tracing models. In addition, the difference in impedance between adjacent domains should be small. Another practical limitation of this approach is that one needs to define the crystallographic direction of each domain independently. This would require defining a large number of parameters for a single weld, which is likely to increase uncertainty in the simulation definition. Moreover, this approach is highly dependent on the image processing algorithm used to detect edges in the macrograph, which further contributes to uncertainty. Nevertheless, this method has been used for modeling welds using ray models in CIVA and FEMs (Jezzine et al. 2013; Szávai et al. 2016).

The second technique for modeling welds is to define a smoothly changing crystallographic orientation. A commonly used analytic model of crystallographic orientation of welds has been developed by Ogilvy (1985). Figure 2.3 shows the parameters used in the Ogilvy model. A local

reference coordinate (shown by the arrow) is defined in the *X*-*Z* plane. θ is the local grain orientation relative to this reference, *D* is half of the weld root width, α is half the angle that the weld boundary makes with the normal to the specimen backwall, *T* is proportional to the tangent of the grain axes at the weld's boundary with the base material, and η (where $0 \leq \eta \leq 1$) is a measure of how fast the grain orientation changes along the x-axis. Equation (2.1) describes the orientation and shape of the modeled crystallographic orientations.

$$\tan\theta = \frac{T(D + z\tan\alpha)}{x^{\eta}} \tag{2.1}$$

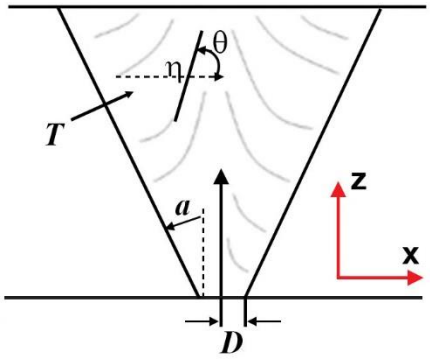

Figure 2.3. Definition of the Ogilvy geometrical weld model.

An example of the Ogilvy parametrization of the crystallographic direction of a weld macrograph is shown in Figure 2.4 (right). The crystallographic orientation is modeled to be continuously varying, and it follows the lines described by the equation. The changes in the weld morphology computed using the Ogilvy parametrization as a function of T are shown in Figure 2.4. Having a continuous analytic equation describing the crystallographic orientation of grains at each point in the weld removes much of the heuristics required in the previous approach.

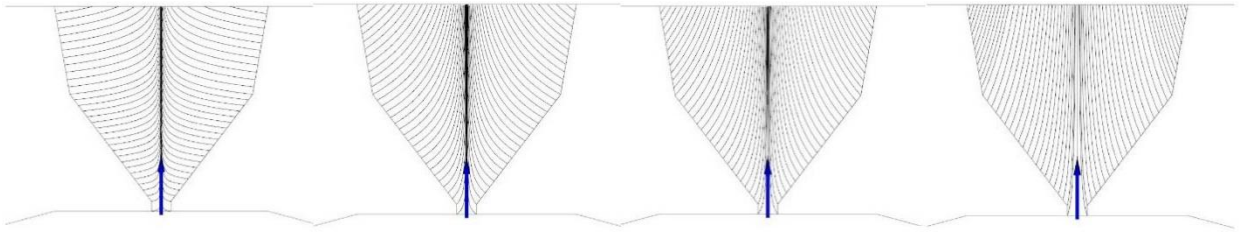

Figure 2.4. Different weld morphologies controlled by the value of T. From left to right, T = 0.1, 0.5, 1, 2.

Compared with the multiple dendritic domains method, the Ogilvy analytic description reduces the number of parameters required to specify the weld and provides a convenient approximation for integrating weld information into a model. However, the smooth variations of material properties as a function of location requires sound propagation models that can support such variations. A modification of the classical ray tracing method, described as dynamic ray tracing, has been developed to handle smoothly varying material properties (Červený 2001; Gardahaut et al. 2014a).

In addition, FEMs can innately handle position-dependent material stiffness matrices (Apfel et al. 2005). However, one would need to implement a tensor transformation law based on the Ogilvy weld parametrization for appropriate representation of the weld in these models.

Attempts have also been made to validate weld models by comparing simulation predictions of B-scans and flaw specular amplitudes with experiments (Chassignole et al. 2008; Gardahaut et al. 2014b). In most validation studies, the flaw specular echo amplitudes are reasonably similar between simulation and experiment. However, the echo-dynamics and reflections from geometrical structures tend to differ between simulation and experiment, and there is currently no definitive approach to assessing the accuracy of models based on echo-dynamics.

2.3 Representation of Noise in Models

The methods described above for modeling beams in isotropic materials and in welds, and computing scatter from flaws, only compute the "signal" component of a UT inspection and ignore any factors that may introduce noise. Noise is any signal that may affect or interfere with the reliability of detecting a flaw signal. In ray-based methods, which are the main topic of this report, a ray is traced from the transducer to a given point in the specimen, and its trajectory is computed based on all interfaces it crosses. The attenuative effects on the propagating ray due to beam redirection can be handled using the dynamic ray tracing model. In the case of coarse grained materials, such as CASS, representation of such structures using Voronoi diagrams (Jenson et al. 2009) has been suggested for modeling the attenuative effects of coarse structures on the propagating rays. No scattering is computed here, and therefore any coherent signals resulting from the grain structures (i.e., structural noise) are ignored.

The ability to model noise is important if the models will be used to estimate UT reliability. We define noise in UT to be from three separate sources: geometric noise, structural noise, and thermal/electronic noise.

Geometric noise refers to any echo that is reflected from specimen boundaries or weld interfaces, such as the weld root, counterbore, or crown. Those reflections appear as specular responses in ultrasound composite view images, and can often be traced back to their reflective source, if the geometry is well known. We also refer to this type of noise as "clutter" because it clutters UT scan images and often resembles flaw responses, rendering it difficult to detect and discriminate flaws, especially if they lie near geometric features with high response amplitudes. This type of noise is computed by models using ray tracing and the Kirchhoff approximation; however, the Kirchhoff integral needs to be computed for all specimen interfaces and boundaries, which significantly increases the computation time.

Structural noise refers to the coherent backscatter of ultrasound due to scattering from grain boundaries. This type of noise generally only occurs in coarse-grained materials, such as CASS or austenitic welds. Structural noise, in software tools such as CIVA, is modeled using a random distribution of point-like scatterers with arbitrary density and reflectivity (Mahaut et al. 2006). Thompson and Margetan (2002) developed a model based on previous literature to handle noise effects and provided a general stochastic noise model for UT.

Finally, thermal/electronic noise refers to the additive noise $n(t)$ inherent in electronic measurement equipment (such as scanner motor noise and amplifier noise) and is simply modeled as additive white noise, typically with a Gaussian distribution.

In general, simulation software are only concerned with geometric and structural noise. This is because they require physics-based principles to be able to realistically reproduce these types of noise.

The simulation of noise from any of these sources is not considered in the work described in this report. The focus instead has been on a fundamental, noise-free, assessment of the ability of simulations to provide qualitative insights into inspection technique reliability. Ongoing research is addressing the question of effectively simulating the impact of noise on inspection capabilities. The results of this ongoing research will be described in future reports.

2.4 Motivation for Current Work

The ability to accurately simulate beam propagation through complex materials such as welds, and the beam interaction with defects in the vicinity of welds, is important to assess whether a proposed inspection technique is reliable. Inherent in this are the need to accurately simulate:

- Ultrasound beams, propagating from the transducer through the material, to assess whether the applied energy is capable of reaching the inspection volume. Also of interest is the variability in results from different simulation models, as this helps in quantifying the impact of model and parameter selection.
- Flaw responses (specular reflected amplitude, tip-diffracted amplitude, and echo-dynamics), to determine if a reasonable flaw response signal is achievable.
- Effects of material inhomogeneity, microstructure, and geometry, all of which contribute to the signal-to-noise ratio (SNR) and influence the ability to reliably detect flaw signal responses and discriminate these responses from non-flaw signal responses.

These issues are examined further in the research described in this report.

3.0 Comparison of Beam Models

As discussed previously, ultrasonic beam simulations provide valuable information about sound intensity within the specimen as well as the sound propagation direction. While useful for assessing insonification of desired volumes within a component, differences in computed beam profiles between different simulation tools can make it difficult to obtain reasonable confidence in probe design and insonification volume calculations. These differences are usually due to differences in the models implemented in common ultrasonic simulation tools. Therefore, there is a need to determine the level of variability one may expect across commonly used ultrasonic beam simulation tools.

Here, the focus is limited to UltraVision (UV, Zetec, Snoqualmie, WA) and CIVA, tools that are commonly used for modeling ultrasonic NDE in the nuclear power industry, as a first cut at quantifying the variance in computed results. CIVA and UV use different wave propagation models. CIVA uses ray tracing theory to model ultrasound beam propagation, while UV uses a modified angular spectrum propagation model. In addition, UV only allows the simulation of isotropic materials; no interactions with flaws or geometric structures such as counterbores can be simulated. Note that the focus of the work described in this section is on quantifying differences and not on validating the tools themselves.

3.1 Beam Simulation Canonical Cases

PNNL conducted beam simulations for a total of 23 probes, including single-element shear wave probes and dual-element transmit-receive longitudinal (TRL) probes. Table 3.1 summarizes the parameters of the shear wave probes, including the center frequency, the probe diameter, and the beam incidence angle in steel. Table 3.2 summarizes the parameters of the longitudinal wave probes. The probes were selected based on commonly used parameters for ultrasonic ISI in NPPs.

Table 3.1. Single-Element Shear Wave Probe Parameters Used in Beam Simulation Studies

Probe Number	Frequency in MHz	Diameter in Inches (mm)	Beam Incidence Angle in Degrees
1	1.00	0.5 (12.7)	45
2	1.50	0.5 (12.7)	45
3	2.25	0.5 (12.7)	45
4	3.50	0.5 (12.7)	45
5	5.00	0.5 (12.7)	45
6	2.25	0.25 (6.35)	45
7	2.25	0.375 (9.5)	45
8	2.25	0.75 (19.05)	45
9	2.25	0.5 (12.7)	30
10	2.25	0.5 (12.7)	60
11	2.25	0.5 (12.7)	70
12	2.25	1.00 (25.4)	45

Table 3.2. Dual-Element Longitudinal Wave Probe Parameters Used in Beam Simulation Studies

Probe Number	Frequency (MHz)	Element size in mm x mm (inches x inches)	Beam Incidence Angle (Degrees)	Focus Depth in mm (inches)
13	1.00	20×34 mm (0.79 x 1.34)	45	39 (1.54)
14	1.50	20×34 mm (0.79 x 1.34)	45	39 (1.54)
15	2.00	20×34 mm (0.79 x 1.34)	45	39 (1.54)
16	4.00	20×34 mm (0.79 x 1.34)	45	39 (1.54)
17	2.00	15×25 (0.59×0.98)	45	39 (1.54)
18	2.00	7×14 (0.28×0.55)	45	39 (1.54)
19	2.00	20×34 mm (0.79 x 1.34)	30	39 (1.54)
20	2.00	20×34 mm (0.79 x 1.34)	60	39 (1.54)
21	2.00	20×34 mm (0.79 x 1.34)	45	50 (1.9)
22	2.00	20×34 mm (0.79 x 1.34)	45	70 (2.76)
23	2.00	20×34 mm (0.79 x 1.34)	45	25 (0.98)

Beam simulations for the 23 probes were run in both CIVA and in UV. No mode conversions were computed. That is, only longitudinal wave modes were computed for longitudinal probes, and only shear modes were computed for shear probes. This simplification reduces the complexity of the assessment and allows for direct comparison of pure modes without the need to account for mode-conversions that are usually not considered for analysis in UT. The same parameter specifications were used as inputs in both CIVA and UV for each probe.

The beam profiles for the shear wave probes (Probes 1–12) are shown in Figure 3.1. The beam profiles have greater spatial extent and persist for greater distances in the CIVA simulations than in the UV simulations. This trend can be observed for all combinations of frequencies, element sizes, and beam angles considered in this study. Similar trends can be seen for the dual-element TRL probes (Probes 13–23) in Figure 3.2. Similarities with CIVA and UV can be seen in terms of the near-field to far-field transition distance for the shear wave probes and the focal distance for the zone-focused dual-element transducers. In Figure 3.3, the beam amplitudes from the two software tools are compared at the backwall of the specimen (specimen thickness was 50 mm [1.97 in.] in these simulations). With respect to CIVA simulations, UV had consistently lower beam amplitude at the backwall (normalized to maximum beam amplitude) with one exception (Probe 22). On average, the maximum beam amplitudes at the backwall were 13% lower in UV compared with those in CIVA.

Although CIVA and UV use different models to simulate transducer beam profiles (angular spectrum vs. ray tracing), it is not clear if observed differences are solely due to the different models. It is possible that differences in handling boundary conditions and propagation across the transducer wedge-specimen interface may also be contributing factors, as might the methods used to model transducer excitation signals and to account for coupling of the energy into the specimen. In addition, the physical quantity (pressure, displacement, or particle velocity) used as the independent variable may differ between the two software packages. Thus, without full knowledge of the underlying model, the specific source(s) of the observed differences cannot be identified with any degree of confidence, and therefore one cannot claim that UV will consistently under-estimate the beam amplitude and beam width relative to CIVA.

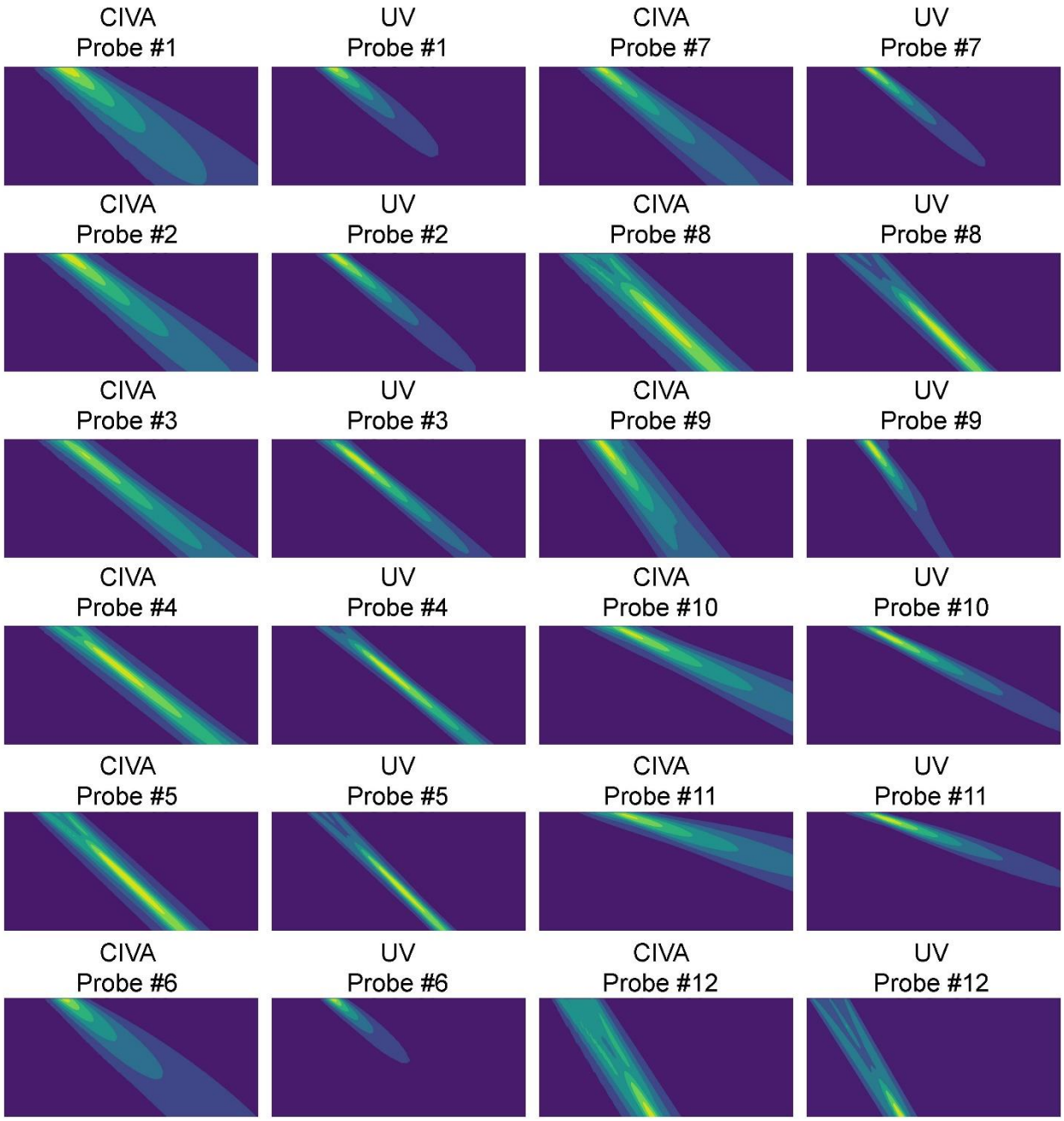

Figure 3.1. Beam simulations for the 12 shear wave probes using CIVA and UV. The specifications of the probes are indicated in the title of each beam as (frequency, diameter, beam angle, mode). The color map color range for each simulation shown is normalized relative to its own maximum amplitude.

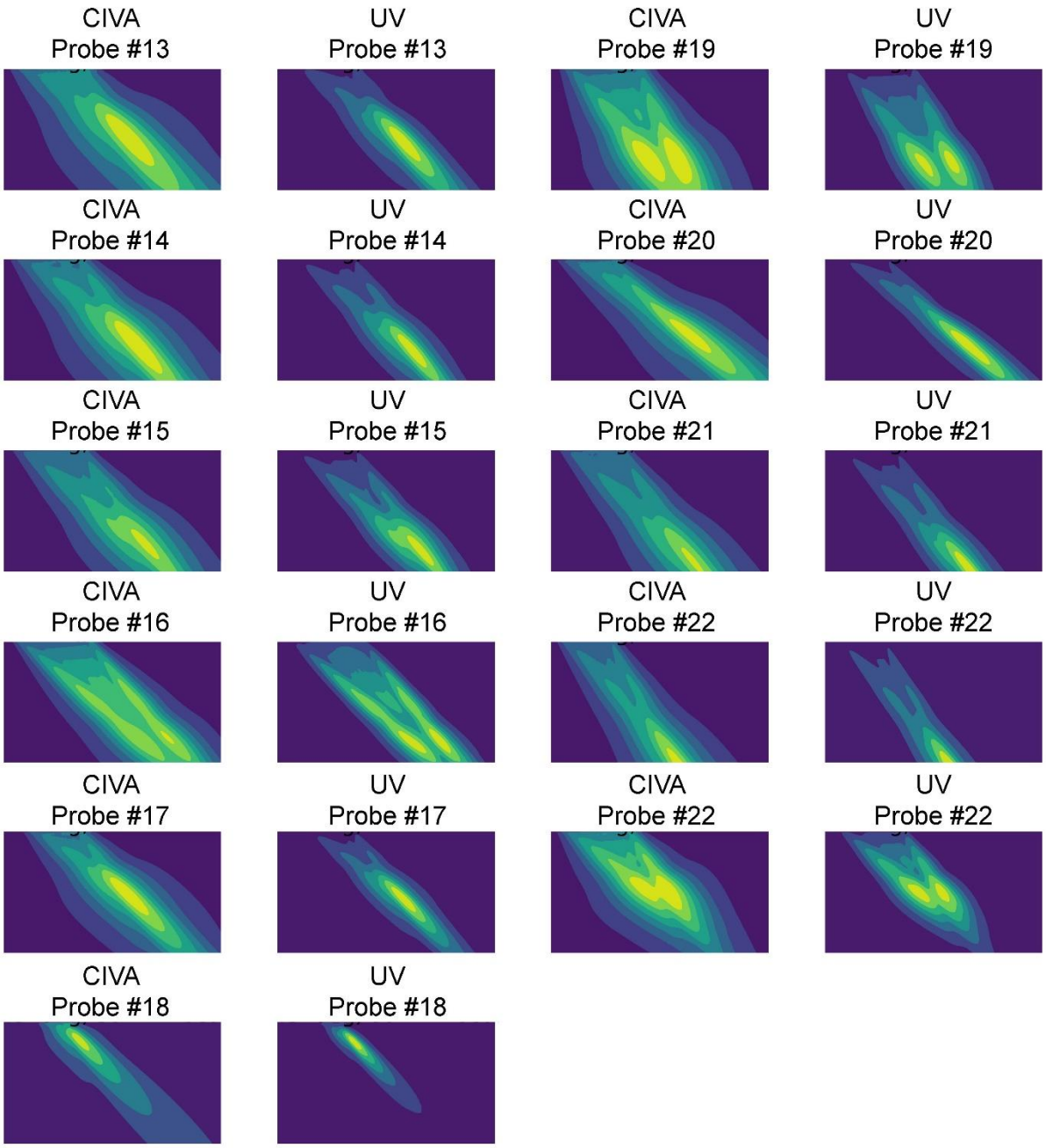

Figure 3.2. Beam simulations for the 11 dual-element transmit receive longitudinal wave probes using CIVA and UV. The specifications of the probes are indicated in the title of each beam as (frequency, diameter, beam angle, mode). The color map color range for each simulation shown is normalized relative to its own maximum amplitude.

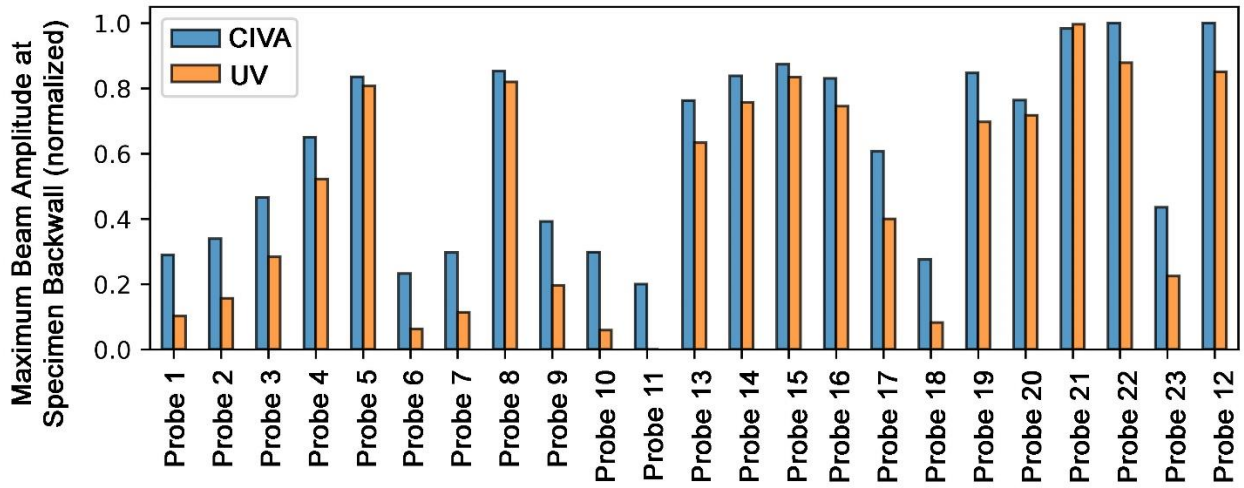

Figure 3.3. Computed beam maximum at specimen backwall (50 mm [1.97 in.] depth) for each of the 23 probes in CIVA and in UV. Each simulation was normalized to its own maximum beam amplitude.[1]

3.2 Discussion

The relative beam amplitude at the backwall (relative to its own maximum beam amplitude) is indicative of the fraction of energy from that probe that is available for interaction with a flaw at the backwall. The spatial extent also provides insights into the volume of material that is insonified, while the relative amplitude distribution within the beam (beam structure) is again a likely measure of the energy distribution within the volume that is available for interaction with a flaw.

The results indicate a difference in the relative beam amplitude at the specimen backwall (relative to the maximum beam amplitude of the probe), and potentially in the structure of the beam, when comparing the results from the two software packages examined here. CIVA indicates a larger relative amplitude at the backwall than UltraVision in 22 out of the 23 probes examined. In addition, the computed relative backwall amplitude for shear wave probes from the two software packages appears to show larger differences in general than those computed for the longitudinal wave probes. The data from these 23 probes also show overall beam structures that are similar; however, the spatial extent of the computed beams from CIVA are larger. It is not clear whether these observations hold in general for other probes, and which of the two sets of simulation results are closer to reality. This last question requires empirical measurements of beam profiles to validate the simulations. Such measurements are underway and will be reported in future reports.

[1] The fact that probe 12 is not illustrated in sequence is not relevant to the information in this figure.

The results observed in this comparison point to the possibility of several factors that may influence the computed beam profiles. These factors are largely due to model and model implementation differences, along with the parameters (e.g., frequency, element size, angle, focal depth) used to represent the transducer. Of these, only the parameters that represent the transducer are controllable by the user, resulting in limited ability to reduce the overall variability in the beam simulations. Consequently, users attempting to use any simulation software (whether the two identified here, or others) need to have an understanding of the models implemented and the resulting capabilities and limitations of these models prior to drawing conclusions.

4.0 Beam Models in Austenitic Welds

While there may be some variability in beam simulations between different simulation software, the presence of welds or other inhomogeneous anisotropic materials can significantly alter the beam propagation path. It is not clear whether simulation models can capture these effects in a realistic manner, at a level of accuracy sufficient for the end-user to make judgments (with confidence) on insonification of the necessary volume or flaw detectability. To address this, simulations of beam propagation in realistic weld geometries are necessary, along with empirical measurements of the beam as it passes through the weld. In combination with simulations and measurements of the beam in regions of isotropic homogeneous materials (such as most base materials far from the weld), we can obtain insights into the adequacy of weld models, simulation procedures, essential variables for obtaining reasonably accurate results, and the physics of ultrasound in complex materials.

In this section, a novel empirical method for measuring cross-sectional beam profiles propagating through austenitic steel welds is described. This measurement technique allows one to visually observe the beam as it propagates through a weld, including its skewing and scattering through the weld's dendritic regions. Those measurements would then allow an analysis of the simulated beam counterparts. The studies in this section are limited to phased-array ultrasonic testing probes, as these probes enable the transmitted beam to be focused onto a surface.

4.1 Materials, Probes, and Experiment Setup

A large pipe segment (mockup 3C-022) is shown in Figure 4.1 and described in Anderson et al. (2011). The base material is Schedule 80, ASTM 358 grade 304 wrought stainless steel (WSS) with approximately 36 mm (1.4 in.) wall thickness. The mockup contains three single-V girth welds (308/308L stainless steel) joining four cylinders made of the base material. The weld crowns were machined down to allow improved access for translation of ultrasonic transducers. Two specimens were extracted, each containing different welds. Thin slices were cut from the edges of the two specimens for polishing and etching to reveal the dendritic structures of the welds. Macrographs of the slices are shown in Figure 4.3, revealing that two different manufacturing processes resulted in a significant difference in the weld dendritic structures. Specimen 1 contains a weld that was manufactured using an air-backed welding technique while the pipe section was held vertically. Specimen 2 contains a weld that was manufactured using water-backed welding while the pipe section was held horizontally. Specimen 1 has an asymmetrical dendritic structure with the weld long axis shifted to the right, whereas Specimen 2 has a symmetric dendritic structure. Both specimens contain a defect on the far side of the weld, one being a saw-cut notch and the other an electro-discharge machined notch. Finally, the specimens were cut such that the edges were vertical, and a perpendicular surface was milled along the axial extent of the sample, as shown in Figure 4.2, for placement of the probe.

Figure 4.1. Mockup 3C-022 from which the two specimen samples were cut for this work. Note that there are three cuts in this pipe, but only two were used.

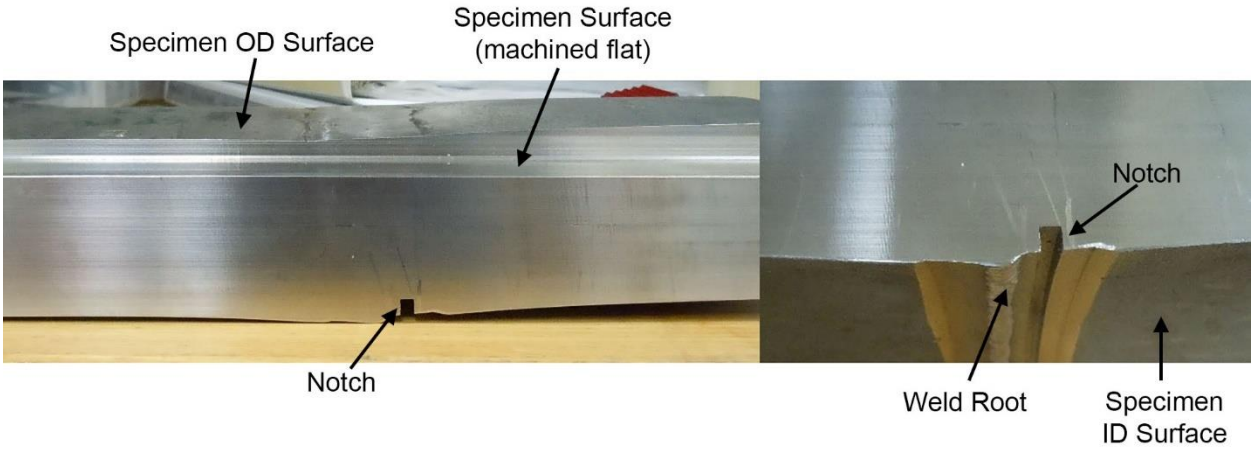

Figure 4.2. Photograph of Specimen 2 with a saw-cut notch. *Left*: Side view of the specimen showing the machined flat top face. *Right*: Bottom of the specimen, showing the weld root and counterbore.

Figure 4.3. Macrographs of the weld within Specimen 1 (*left*) and Specimen 2 (*right*).

A 2.0 MHz phased-array ultrasonic testing transducer (Figure 4.4, *left*) (dual array, arranged in a TRL configuration) was used to map the ultrasonic beam after it had passed through austenitic weld material or WSS base material. To map the side profile of the beam, the transmit probe was mounted on a wedge and placed on the machined section of each specimen. The beam was focused onto the surface of the specimen, representing the middle plane of a standard TRL configuration that would be simulated in software.

The positioning of the probe on the specimen is shown in Figure 4.4 (*right*). The probe was positioned at two locations to obtain two beam maps at each angle (30°, 45°, and 60°) for each specimen. In the first location, the front of the wedge was positioned above the weld root, obtaining a beam that propagated through the weld. The probe was them moved 60 mm (2.36 in.) away from the weld to obtain a beam map that only propagated through the base metal. We describe the beam mapping process next, and note that the equipment used and much of the measurement setup is similar to that used in previous sound field mapping studies (Crawford et al. 2014).

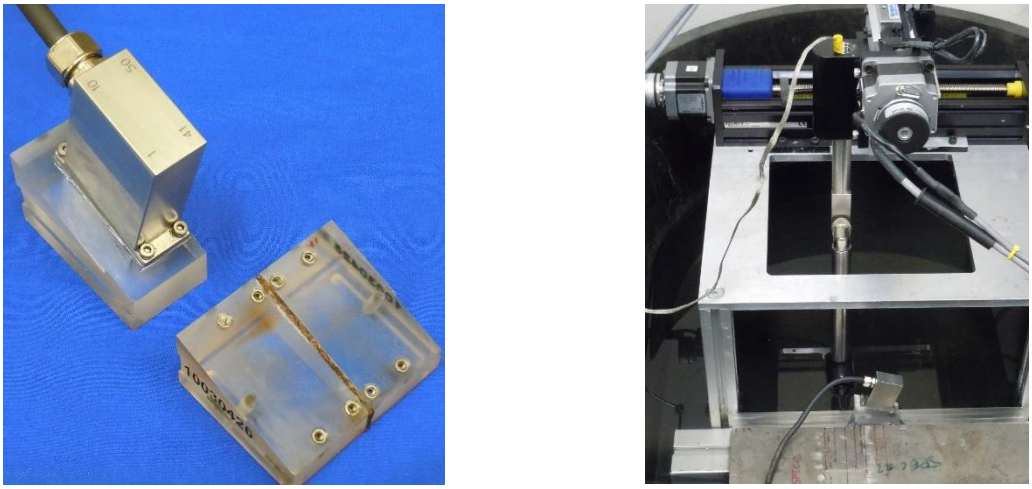

Figure 4.4. Phased-array probe (transmit only) used for transmitting a beam through the specimen (*left*). Only half of the wedge was used (the full wedge is shown for comparison). The probe is shown positioned on a specimen for beam mapping (*right*).

The pulser-receiver used was a Zetec DYNARAY Lite with a LEMO adapter attached to the receive port to access individual pins. Pin 34 of the receiver port was connected to a pinducer, while the transmitter port was connected to the PAUT probe. The PAUT transducer was defined in UV to function as if it were operating in a TRL configuration, using the standard focal law calculator and defining the wedge as twice the width (as if a whole wedge, and therefore both the transmit and receive arrays, existed on the part). Once focal laws were calculated, all receive probe elements were disabled except one, which was the pinducer connection. All other delays, angles, and offsets were set to zero to prevent display errors. Figures 4.5 and 4.6 show screenshots from UV of the setup to illustrate this process.

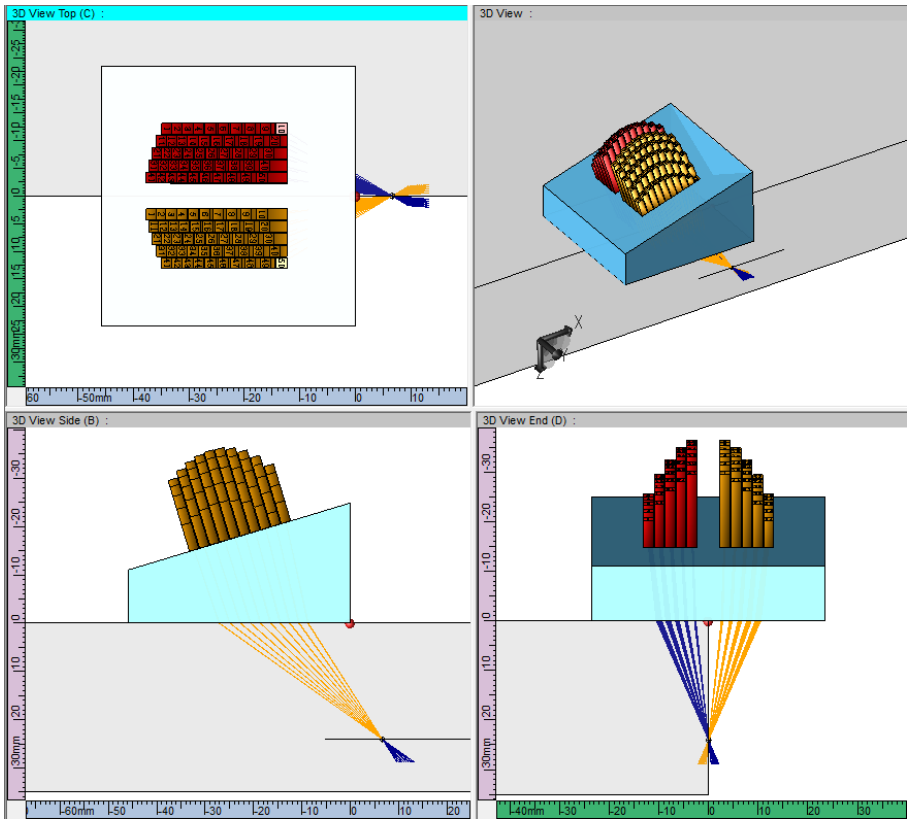

Figure 4.5. Probe with focal law on specimen edge. Focal laws for both transmit and receive probes are shown, but only the transmit focal laws were used.

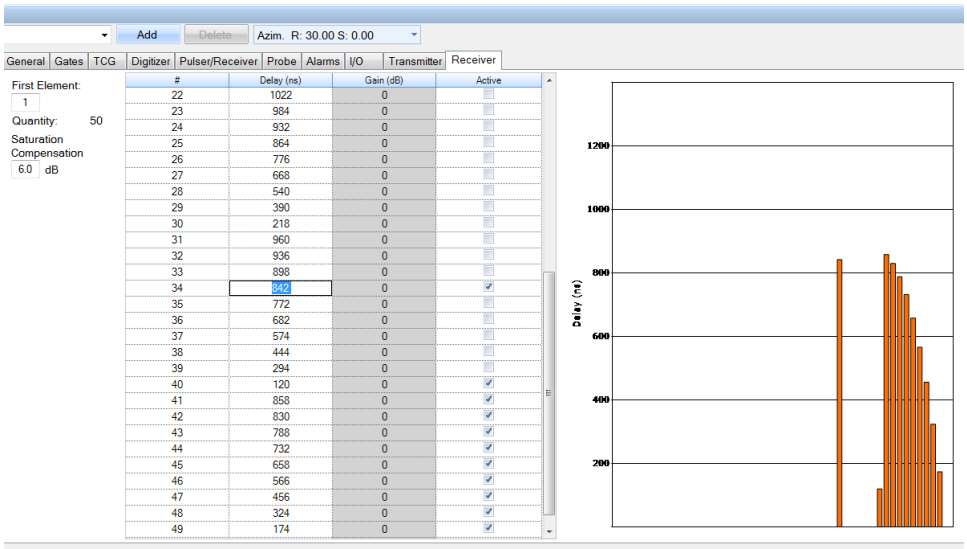

Figure 4.6. Focal law delays. This figure shows that all receive elements were turned off except the pinducer connection (Pin 34).

Data were collected by raster scanning the pinducer parallel to the machined face of the specimen (Figure 4.7) while the transmitter probe pulsed simultaneously. A slight standoff (~0.2 mm [0.008 in.]) was maintained between the face of the pinducer and the specimen in an immersion environment to allow coupling without introducing any surface friction noise. The

scan therefore shows the sound interaction with the face of the specimen as well as the time information as to when that signal arrives. Any scattering of the sound away from that face will not be seen by the pinducer, much like a simulation on a single plane. Because of the water immersion, any shear modality that does not convert to longitudinal upon interacting with the water interface will not be detected. A common reference origin was used for all the scans, placed at the edge of the machined surface and the weld center line. All raster scans were collected across the entire height of the specimen and with 0.5 mm (0.02 in.) spatial resolution for both the vertical and horizontal axes.

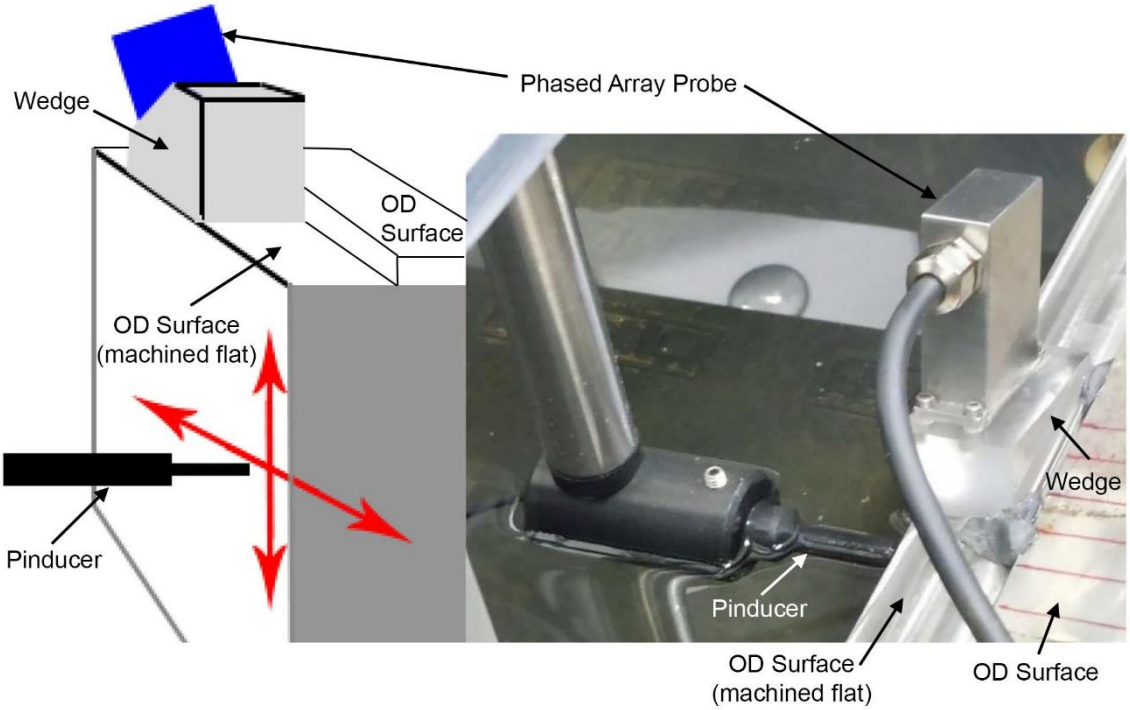

Figure 4.7. Pinducer arrangement for face mapping. The red arrows indicate the direction of motion of the pinducer.

4.2 Simulations in CIVA

Each of the measured beam scenarios was simulated using CIVA. All required probe parameters were obtained from the probe design specification. The specimen base material was specified as isotropic with density 7800 kg/m^3, shear wave velocity 3230 m/s, and longitudinal wave velocity 5800 m/s. The material properties for the weld (predefined in CIVA) were specified to have cubic symmetry with C_{11} = 245 GPa, C_{12} = 145 GPA, and C_{44} = 110 GPa. These material properties were selected based on literature values (Chassignole et al. 2009; Gardahaut et al. 2014b; Szávai et al. 2016); these are also the default values provided in CIVA's library of materials.

The weld was modeled using the Ogilvy geometric parameterization (see Section 2.2), with initial values for *D* and *α* specified to be 1.6 mm (0.06 in.) and 37.5° based on the weld morphology, and T and η set to 1 initially. The slowness curves in the *X*–*Z* plane (defined in Section 2.2 and shown in Figure 2.2) were used to represent the effects of anisotropy in the weld. The macrographs for both specimens were used to fine-tune the parameters of the Ogilvy model. An overlay of the Ogilvy-derived crystallographic orientations and the macrographs is shown in Figure 4.8. In addition, the location of the probe relative to the weld is also shown. All simulations were run with direct beam computation only, and no mode conversions were computed.

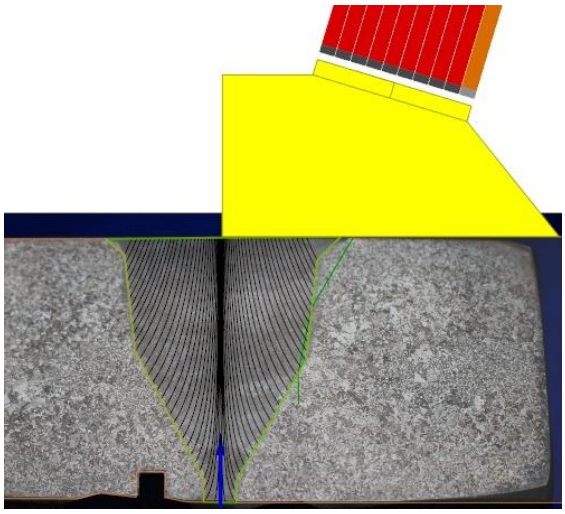

Figure 4.8. Relative position of probe and weld and description of weld in CIVA using the Ogilvy model. Specimen 2 is shown.

4.3 Results and Discussion

Both the simulation and experimental results for the three angles of the phased array probe in the two specimens are shown in Figure 4.9 and Figure 4.10. A median filter was applied to the experiment beams to reduce the measurement noise.

The figures show the presence of some beam skewing in the ultrasound beams as they propagate through the weld. At higher angles, the experimentally obtained beam appears to have a smaller spatial extent than the simulated beam. This is likely due to the fact that attenuation is not explicitly included in the simulation results shown but does play a role in the measurements. Attenuation in the weld tends to be direction-dependent and increases with increasing beam angle relative to the long axis of the weld. In addition, the higher angles tend to result in greater scattering of ultrasound from the weld microstructure and result in increased noise and potentially sub-optimal beam shapes for flaw detection. Note that the data shown in Figures 4.9 and 4.10 reflect the results of median filtering to reduce the level of noise. Therefore, beam formation and propagation is reduced with higher angles even under ideal conditions.

A comparison of the experimentally obtained data with those from simulations indicates that, in most cases, the simulations over-estimate the relative beam amplitudes at the specimen backwall and the beam sizes. This is especially true with higher beam angles. We also measured the effective beam angle as the direction of highest energy of the beam based on the simulated and experimental beam profiles shown in the figures above; see Table 4.1. In most cases, the simulated angle deviates from the empirical angle, which is likely due to uncertainties in the material properties used in computing the empirical phased-array delay laws and simulation results.

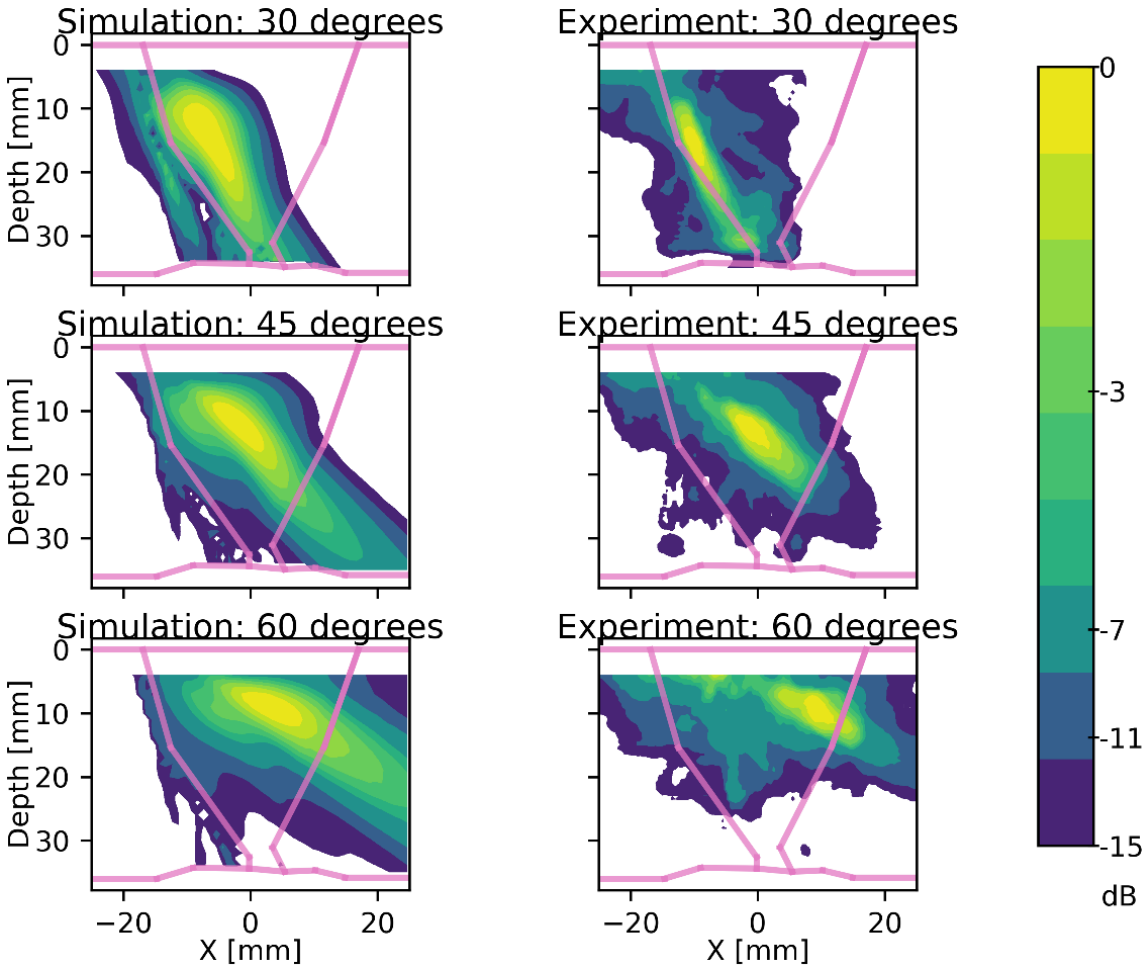

Figure 4.9. Simulated and experimental sound beams using the phased array probe at 30°, 45°, and 60° angles through Specimen 1. The weld root is located at X=0 mm. Each beam map is normalized to itself.

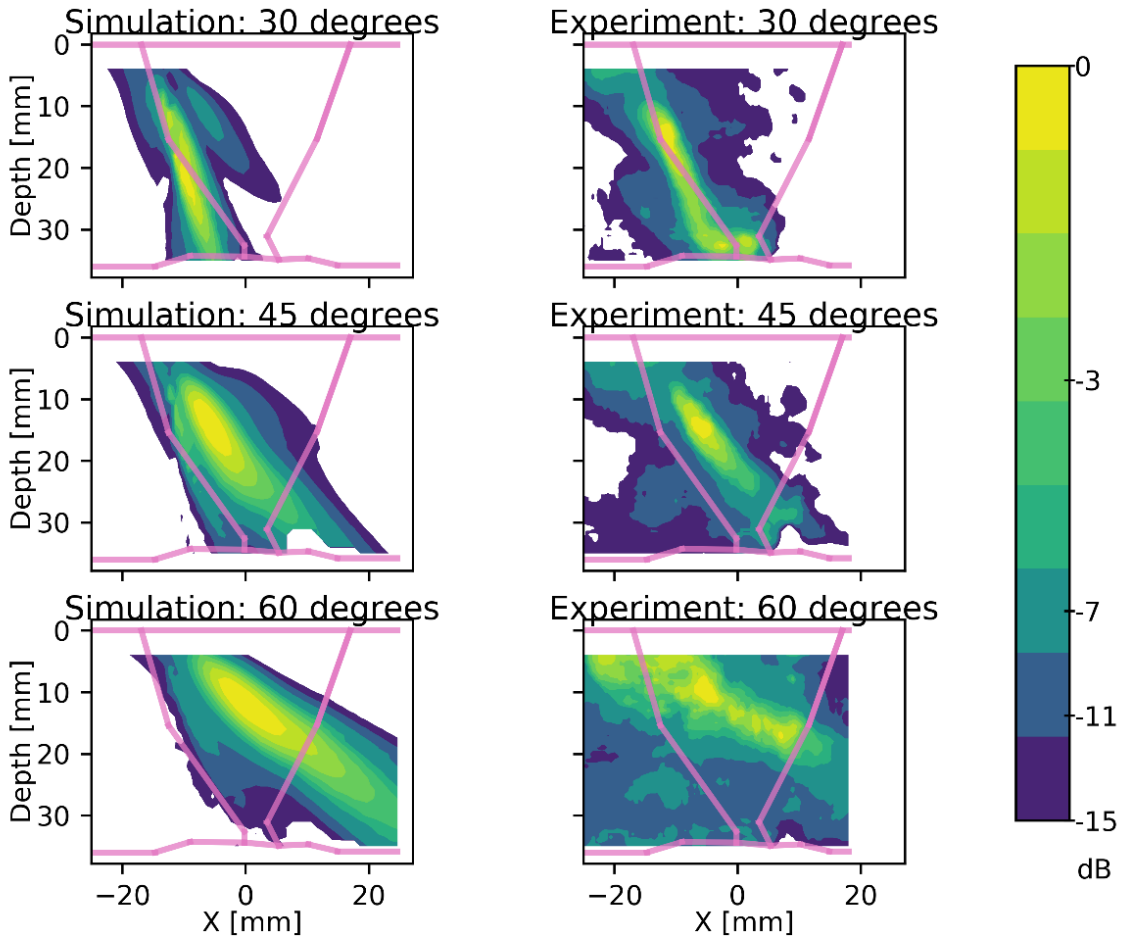

Figure 4.10. Simulated and experimental sound beams using the phased-array probe at 30°, 45°, and 60° angles through Specimen 2. The weld root is located at X=0 mm. Each beam map is normalized to itself.

Table 4.1. Computed Effective Beam Angle for Experiments and Simulations

Specimen	Probe	Focus Angle, degrees	Actual Angle Experiment, degrees	Actual Angle Simulation, degrees
1	PAUT	30	23.5	27.8
		45	48	42.1
		60	58.7	60.4
2	PAUT	30	20.8	16.6
		45	38	39.4
		60	63	51.5

Overall, factors contributing to the differences between simulation and experimental beam models are summarized as follows:

1. No attenuation was considered in the simulations, which might be of high significance for ultrasound propagation in austenitic welds.
2. The weld geometry and microstructure definition were obtained from the macrographs but were approximated by the Ogilvy model.
3. The elastic material properties for the weld regions were not measured and were taken from the literature. The uncertainties in the stiffness matrix is another factor contributing to simulation uncertainties.

The quantification of the above factors is an ongoing effort. A good estimate of the confidence in these simulations should be available once these factors have been quantified. Subsequently, results may be used to estimate the applicability of the Ogilvy weld parameterization and the dynamic ray tracing model to such weld geometries that are common in the nuclear power industry.

5.0 Beam Models as Surrogates for Flaw Models

Beam models allow for the visualization and computation of the ultrasound beams (sound fields) within a specimen of interest and provide valuable information about how a sound field emanates from the transducer and propagates through the material. Such information can be important for designing probes to meet specific design requirements. Another use of beam models has been for determining the ability of probes to detect flaws and for computing coverage volumes. Currently, however, there is no consensus on how beam simulations might be used to assess flaw detection capability or to compute coverage volumes.

Figure 5.1 shows the cross section of a beam within an isotropic plate. The beam is shown as a contour plot with color gradations corresponding to −3 dB steps and limited to the range between −12 dB (purple) and 0 dB (yellow). The beam amplitude incident onto the backwall of the plate is −12 dB relative to the maximum beam amplitude at the near-field/far-field transition distance. Open questions about the ability of the specified probe to detect the crack shown in Figure 5.1 include whether:

- the specified beam amplitude (−12 dB) is sufficient to detect a back-wall connected crack of some significant size;
- a larger amplitude at the backwall (say −6 dB) from a second probe with different key characteristics (frequency, size, beam angle, wave mode) will result in better overall detection performance;
- absolute beam amplitude based on the total power transmitted by the probe correlates better with detection performance than relative beam amplitude (relative to the near-field distance, a normalization approach used frequently within industry);
- flaws that are not fully insonified (especially near the corner with the backwall) are still capable of producing a reasonable ultrasonic response, and the correlation between the degree of flaw insonification and the flaw response/detection capability.

Indeed, many of those questions arise from a missing but crucial piece of information—how a flaw (such as the one shown in Figure 5.1) interacts with an applied ultrasound beam. Ultrasound beam interaction with cracks is a non-linear phenomenon; thus, one would expect that answering such questions without having access to flaw scattering models would be challenging, if not impossible.

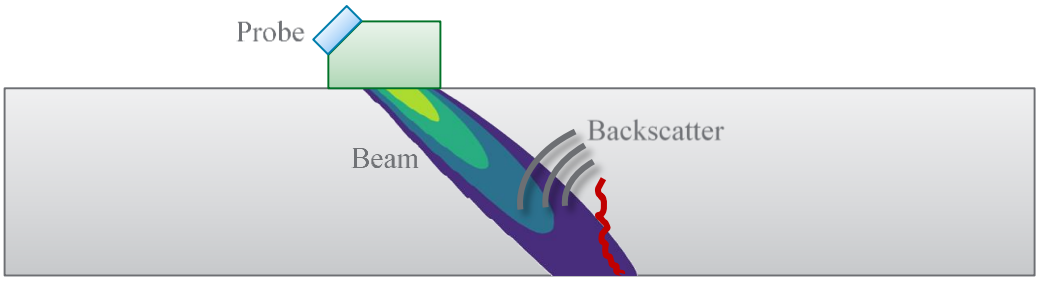

Figure 5.1. Cross-sectional view of a beam simulation. The amplitude of the beam incident at the back-wall is −12 dB relative to the maximum beam amplitude (which is always at the near-field/far-field transition point). The beam contours show color gradations in −3 dB steps.

In this section, we describe results of research performed with the objective of determining if beam models can be reliably used as surrogates for flaw response models and therefore be used for determining detection capability.

We investigated the amount of information that a beam model conveys about the expected amplitude from a flaw based on two scenarios:

- The probe is allowed full-scan access to the specimen surface, and thus direct beam incidence onto the flaw for full echo-dynamic recording is possible.
- The flaw does not lie within the direct path of the beam. This is similar to a limited-access scenario, where the scannable area on the specimen surface is limited, and flaw scattering from the beam fringes is needed to insonify such flaws.

5.1 Methodology and Simulations

To address the questions posed above, we computed a beam metric representing the amount of beam energy incident on the flaw. Then, we compared the beam metric to the maximum flaw backscatter amplitude received by the probe.

In this study, we considered different probe and flaw configurations. Specifically, we used the same 23 probes (single-element refracted shear, and dual-element TRL) described in Section 3.1. The beam simulations, using CIVA only, are shown in Figure 5.2. The probe parameters (frequency, element size, angle, and depth of focus) were then varied (one parameter at a time with the others kept constant) using the parameter ranges described in Section 3.1.

Grouping the 23 probes into categories where only one parameter was changed at a time allowed the capability to visualize the effects of each probe parameter on the relationship between the beam metric and the maximum flaw backscatter amplitudes. The WSS specimen used in these simulations was assumed homogeneous and isotropic with thickness 50 mm (1.97 in.), a density of 7800 kg/m^3, a longitudinal wave speed of 5900 m/s, and a shear wave speed of 3230 m/s.

In addition to beam simulations, flaw response simulations were conducted for each probe using eight different flaw sizes. In the flaw response models, a scan was simulated with the probe positioned on the specimen surface and scanned across the flaw centerline. The scan range was different for each probe to ensure that all significant echoes from the flaw were recorded. The flaws were backwall-connected, rectangular notches with height shown in Table 5.1. All flaw lengths were 50.8 mm (2.0 in.). In cases where flaw amplitude normalization was applied, the flaw amplitudes were normalized relative to the 10% through-wall flaw, which was set to 0 dB. Figure 5.3 shows an example of a B-scan using a 12.5 mm (0.5 in.) diameter shear wave probe at 1 MHz with a 45° beam angle and a 25% through-wall notch height.

Table 5.1. Notch Heights

Notch	% Through-wall Height	Through-wall Depth (mm)	Through-wall Depth (in.)
1	5	2.5	0.1
2	10	5.0	0.2
3	15	7.5	0.3
4	20	10.0	0.4
5	25	12.5	0.5
6	35	17.5	0.7
7	50	25.0	1.0
8	75	37.5	1.5

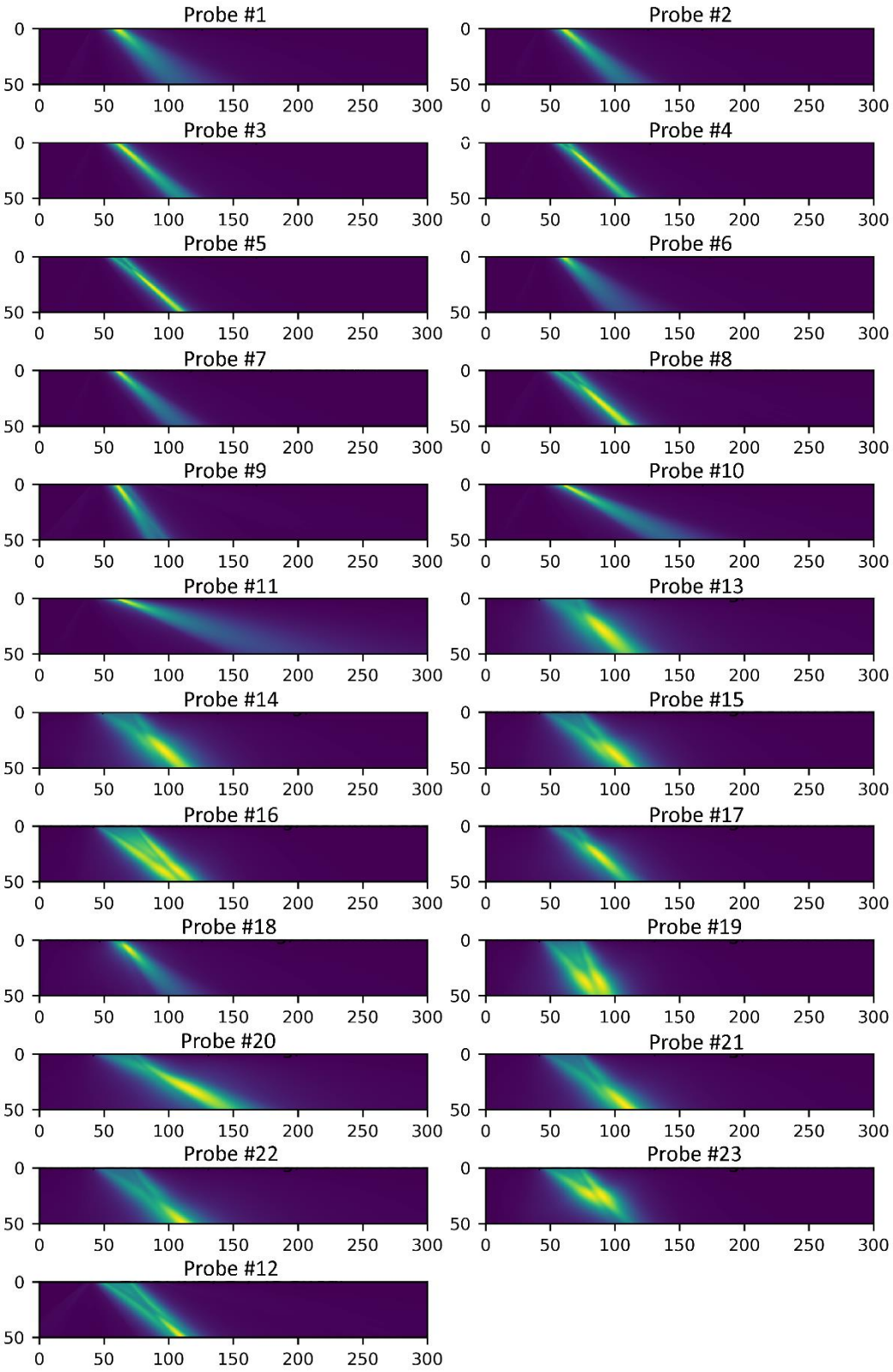

Figure 5.2. The cross-sectional beam simulations for all 23 probes. The color map ranges for each beam are independent. That is, each beam has its own color map normalized to span its independent minimum to maximum range.

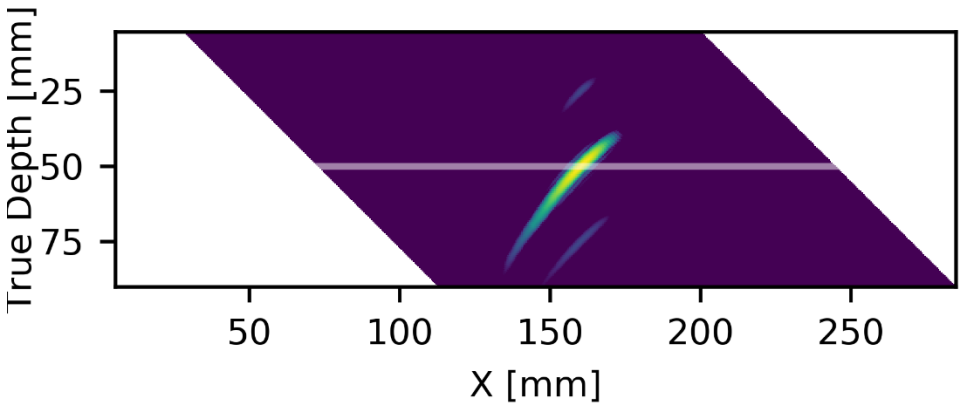

Figure 5.3. Example of a B-scan generated using a single-element shear probe. The horizontal line across the B-scan indicates the location of specimen back wall.

For all simulations (including beams and flaw responses), no mode-conversion computations were enabled in order to reduce the computational time. That is, for the shear-wave probes, only shear modes were computed, and for longitudinal-wave probes, only longitudinal modes were computed.

5.2 Full Access and Insonification

In the full access scenario, the probe was able to fully scan across the specimen surface. Thus, for the flaw response simulations, the flaw backscatter amplitude was simply computed by taking the maximum value of the B-scan. Since the material was isotropic and mode conversion was not computed, the B-scan maximum amplitude corresponds to the flaw backscatter amplitude.

For the beam simulations, we defined the maximum total beam amplitude at the flaw (referred to as the beam metric) and used it as a surrogate for the total incident energy on the flaw (Figure 5.4). We first computed the beam amplitude along the depth for a single probe scan position (right panel in Figure 5.4). The amplitude within the shaded region (flaw height) was integrated to give the total beam amplitude at the scan position. This process was repeated for each scan position, resulting in the total beam amplitude as a function of scan position (bottom panel in Figure 5.4). Since the probe had full access, we selected the maximum value of this curve (total beam amplitude) as the beam metric value. This is shown as the red dot on the curve in the bottom panel of Figure 5.4. For comparison, we also computed a second metric, using only the maximum amplitude of the beam incident onto the flaw. The results for both metrics were similar, and in the following we describe our analysis using the maximum total beam amplitude metric because it is more rigorous.

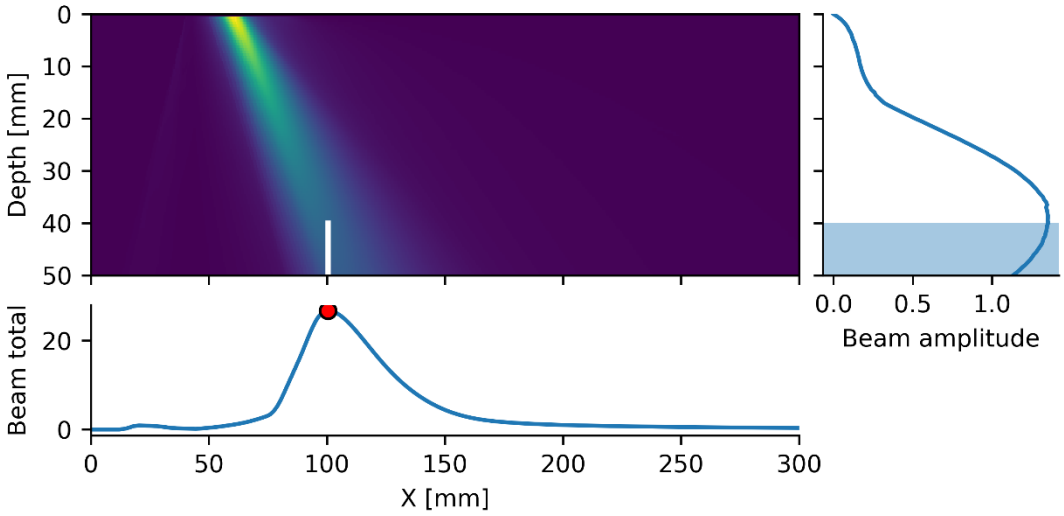

Figure 5.4. Computation of the total beam amplitude incident onto flaw.

In the following section, we consider normalized and non-normalized versions of the beam and flaw backscatter amplitude. In the non-normalized version, the absolute values of the B-scans and beam as computed by the model are used to compute the metrics for the eight different notch heights, and the results are described in Section 5.2.1. In the normalized analyses (described in Section 5.2.2), the amplitudes of the B-scans of the eight notches are normalized relative to the maximum amplitude of the response from the 10% (5 mm [0.2 in.]) through-wall notch. Each beam simulation is normalized relative to its own maximum amplitude, which occurs at the near-field/far-field transition distance.

5.2.1 Non-normalized Metrics

For shear wave probes, each of the three parameters—frequency, diameter, and angle—were changed one at a time. The nominal values (used when the parameter was not varied) were 2.25 MHz, 12.7 mm (0.5 in.), and 45° for frequency, element diameter, and beam angle, respectively. Figure 5.5 shows the beam metric and the flaw backscatter amplitude for single-element shear wave transducers at the eight different notch heights between 2.5 mm (0.1 in.) and 37.5 mm (1.48 in.).

When the element size and beam angle were held constant and only the frequency was varied (left panel in Figure 5.5), the flaw backscatter amplitude increased with the beam metric. In addition, lower frequencies appeared to result in a larger beam metric and flaw backscatter amplitude. We see similar trends when only the probe diameter was changed (center panel in Figure 5.5). In this case, when the diameter increased, both the beam metric and flaw backscatter amplitude increased. However, when the beam angle was varied, backscatter amplitude was largely independent of the beam metric (right panel in Figure 5.5), with beam metric and backscatter amplitude showing a maximum at 45°. Also, the 30° and 60° angle probes gave nearly the same flaw backscatter amplitudes, while the beam metric for the 30° probe was higher than that of the 60° probe. Thus, this shows a scenario where the beam energy incident on the flaw increases with no corresponding increase in flaw backscattered energy. Note that for a given frequency the flaw amplitude levels off after the beam metric reaches some peak value, suggesting that larger beam metrics do not give higher responses. The same effect is present for the probe diameter.

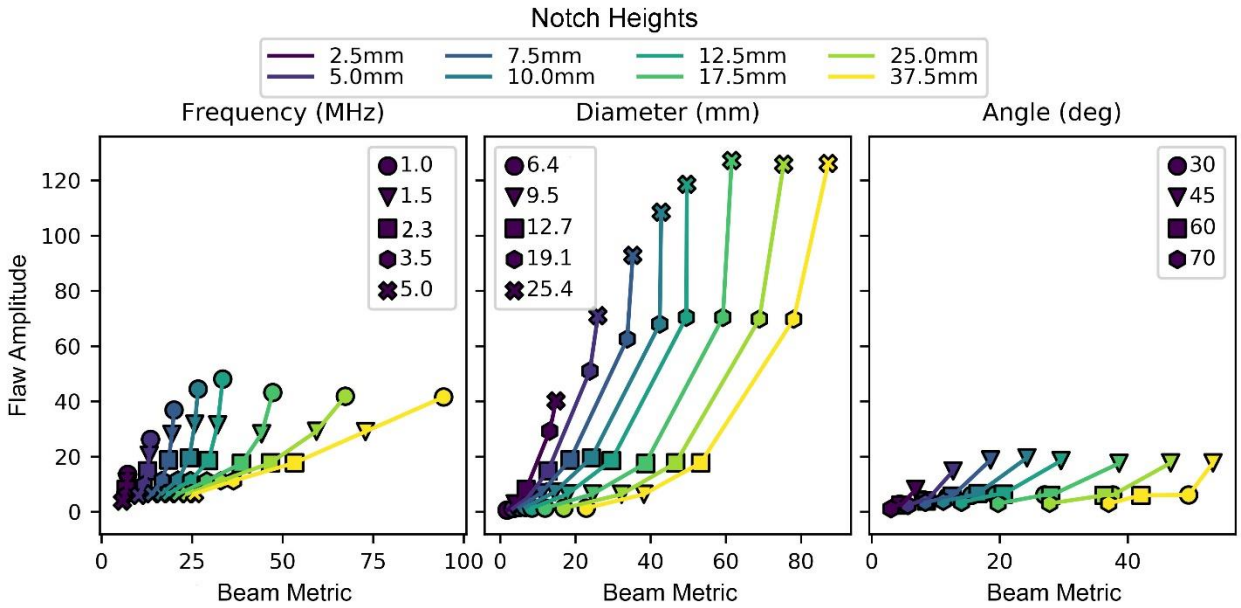

Figure 5.5. Beam metric vs. flaw backscatter amplitude for shear wave probe and for eight different notch heights. One probe parameter was changed at a time: frequency (*left*), diameter (*center*), and beam angle (*right*).

For the dual-element longitudinal wave probes, four parameters were changed, one at a time—frequency, probe size, angle, and focal distance—with their nominal values being 2 MHz, 34×20 mm (0.8×1.34 in.), 45°, and 39 mm (1.54 in.) for frequency, rectangular element size, beam angle, and focal depth, respectively. Figure 5.6 shows the relation between beam metric and flaw backscatter amplitude. For frequency and element size (left two panels in Figure 5.6), there are trends similar to those of the shear wave probes in Figure 5.5. For beam angle variation (third panel from left in Figure 5.6), the 45° shear wave probe achieved the largest backscatter amplitude for all flaws; however, the 30° probe achieved a larger beam metric. This again shows a scenario where a larger flaw backscatter amplitude does not directly correlate with more sound incident onto the flaw. Similar conclusions are reached by examining the change in focal depth (right panel in Figure 5.6). A probe with 25 mm (0.98 in.) focal depth has smaller flaw backscatter amplitude relative to the other probes with larger focal depth. However, the beam metric for the 25 mm (0.98 in.) focus probe was larger than both the 39 mm and 50 mm (1.54 in. and 1.97 in.) focus probes.

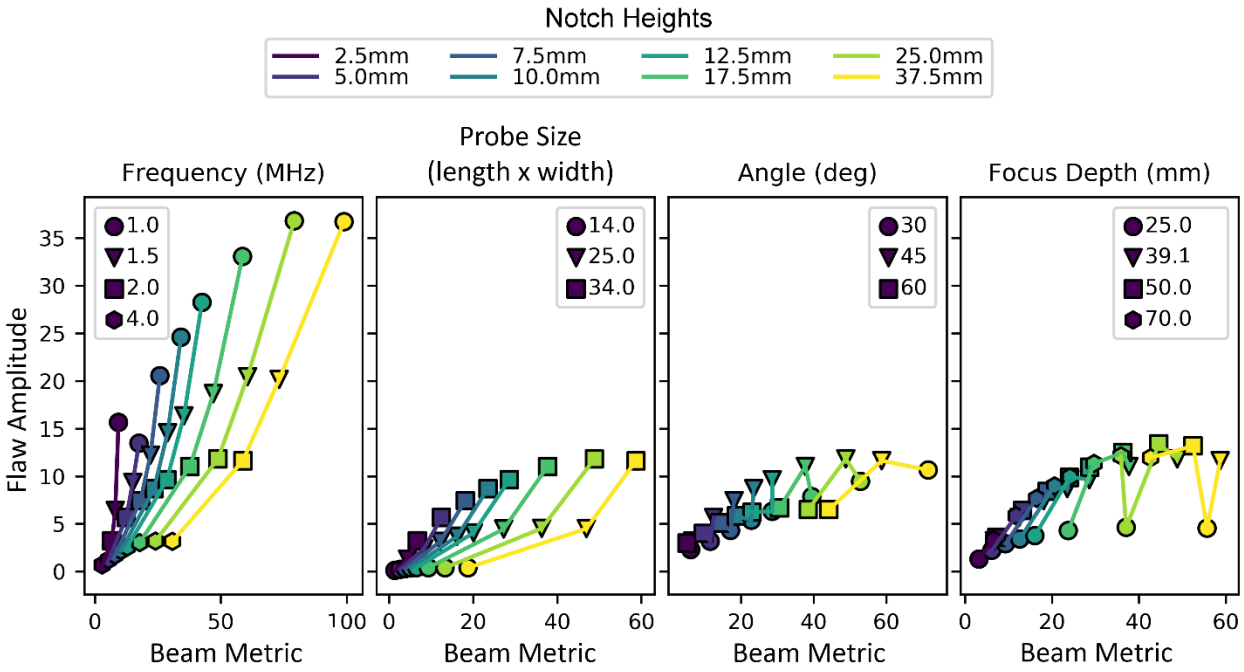

Figure 5.6. Beam metric vs. flaw backscatter amplitude for transmit receive longitudinal probes and for eight different notch heights. One probe parameter was changed at a time from left to right: frequency, probe size (length x width), beam angle, and focal distance.

Overall, Figures 5.5 and 5.6 show that the relationship between maximum beam metric and flaw backscatter amplitude is a complex function of flaw scattering physics, incident beam energy on the flaw, and each of the probe parameters (frequency, size, angle, and focus). This function is non-linear, making it difficult to deduce expected relative backscatter between two probes from a given flaw, even when only a single parameter is changing. The analysis above attempts to define a metric that approximates the amount of beam energy incident on the flaw. However, these approximations do not convey the complete physics of ultrasound interaction with the flaw. Thus, the best approach to using simulations to determine flaw detection capability will need to be based on flaw backscatter models or the wave equation itself, and not a simplified assessment of ultrasound beam-based volumetric coverage.

Combining the data from all the probes provides some insight into the use of beam amplitudes for inferring flaw detectability. Figure 5.7 shows the resulting plot of the beam metric against the flaw backscatter amplitudes. As seen from the data, there is a general positive correlation between the beam metric and flaw amplitude. However, as expected, there is no monotonic trend between the beam metric and flaw backscatter amplitude. The two probes with the lowest beam metric for each flaw are the smallest shear probe and smallest TRL probe. They also have lower flaw amplitudes than all other probes. However, for the remaining larger probes, there is no particular relationship between beam and flaw amplitudes.

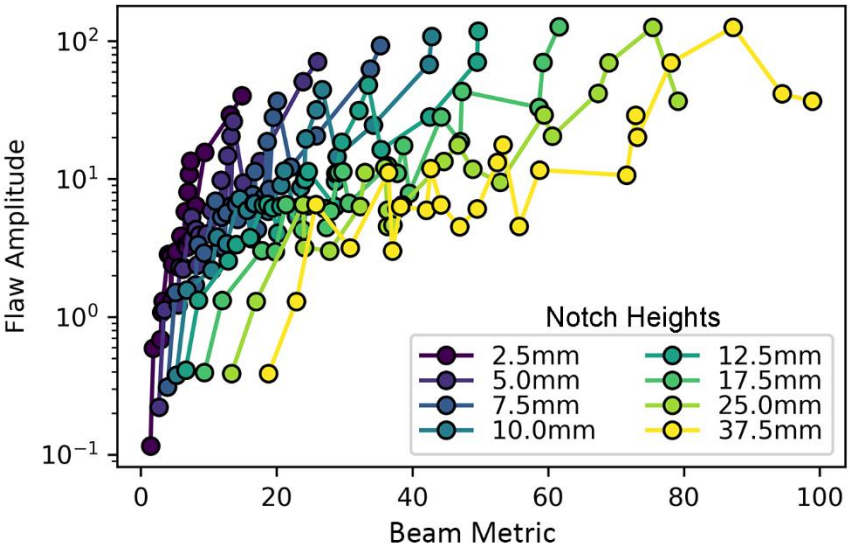

Figure 5.7. Flaw amplitude vs. beam metric for all different probes.

Results support the idea that, in general, a probe designed to have greater beam energy at the expected flaw location is expected to result in larger flaw amplitudes. Similar data using merely the beam amplitude at the flaw location instead of the beam metric did not show any correlation with flaw amplitudes. This is to be expected and is an indication of the fact that flaw return amplitudes are a function of the total beam energy that interacts with the flaw and not merely the beam energy amplitude at the flaw location. Thus, any conclusions that are drawn on flaw detectability from simulation-based beam volumetric coverage will need to be based on an understanding of the interaction of the applied ultrasound energy with the flaw. Note also that these insights are based on the raw (non-normalized) amplitudes and energy calculated from the simulation results and, as such, do not account for differences in the transmitted power from the different transducers.

5.2.2 Normalized Metrics

Normalization, or calibration, is commonly used in UT to obtain repeatable measurements from flaws and correct for variations due to equipment and environmental conditions. This type of calibration is often achieved by scaling the response from a known flaw size to a fraction of full screen height (typically 80%–100%). All data are then scaled by this same factor. Thus, the normalized flaw amplitude is always referenced to the amplitude from a known flaw, and this eliminates the effects of variable transmitted power on the received signal amplitude. In our simulations, we used the amplitude from a 5 mm (0.2 in.) (10% through-wall) notch as the reference for normalization.

In addition to flaw signal normalization, beam normalization is also common and reflects a situation where the maximum amplitude of the beam is normalized to unit amplitude (0 dB). Note that some beam models only compute normalized beam amplitudes. This additional normalization step also eliminates the dependency of the beam metric on the transmitted power. The normalized beam metric only depends on the rate at which the beam amplitude is reduced with propagation distance. However, this rate of decay is a non-linear function of the probe parameters considered in this study (frequency, size, angle, focal depth).

Figure 5.8 shows the normalized beam metric versus the normalized flaw amplitude for the shear wave probes. As seen from comparing Figure 5.8 to Figure 5.5 (the non-normalized case), the normalization resulted in different trends. Note that in the normalized case, the 5 mm (0.2 in.) flaw (10%) did not change in flaw amplitude, as it was used for normalization and was always set to 0 dB. However, the beam metric changed, as different probes produced different maximum total beam amplitudes on the flaw.

Increases in frequency (left panel in Figure 5.8) resulted in an increasing flaw amplitude with the beam metric for the flaw smaller than the reference flaw. However, flaws larger than the reference flaw showed the opposite trend, where the flaw backscatter amplitude decreased as the beam metric increased. This can be somewhat counterintuitive. In this case, the beam amplitude data for each probe presented in Figure 5.8 was normalized with respect to the maximum amplitude within the beam. The normalization counteracted the effects of reduced transmitted power at higher frequencies seen from simulations. At the same time, increasing frequency resulted in a tighter beam pattern (see Figure 5.2) and a greater fraction of the energy incident on the flaw, resulting in an increase in the beam metric. Note that this only applies for shallow flaws; at some point the flaw is so large that there is no practical difference in the normalized beam metric with a tighter beam.

On the other hand, the normalized flaw amplitude is a function of the beam interaction with the flaw as well as the amplitude generated by beam interaction with a reference flaw. Assuming a 45° incidence on the corner of the flaw, the rate at which the raw reference flaw signal and the signal from the flaw of interest change with frequency are different (see Figure 5.5). The result, in this case, appears to be a decrease in the normalized flaw signal with an increase in frequency.

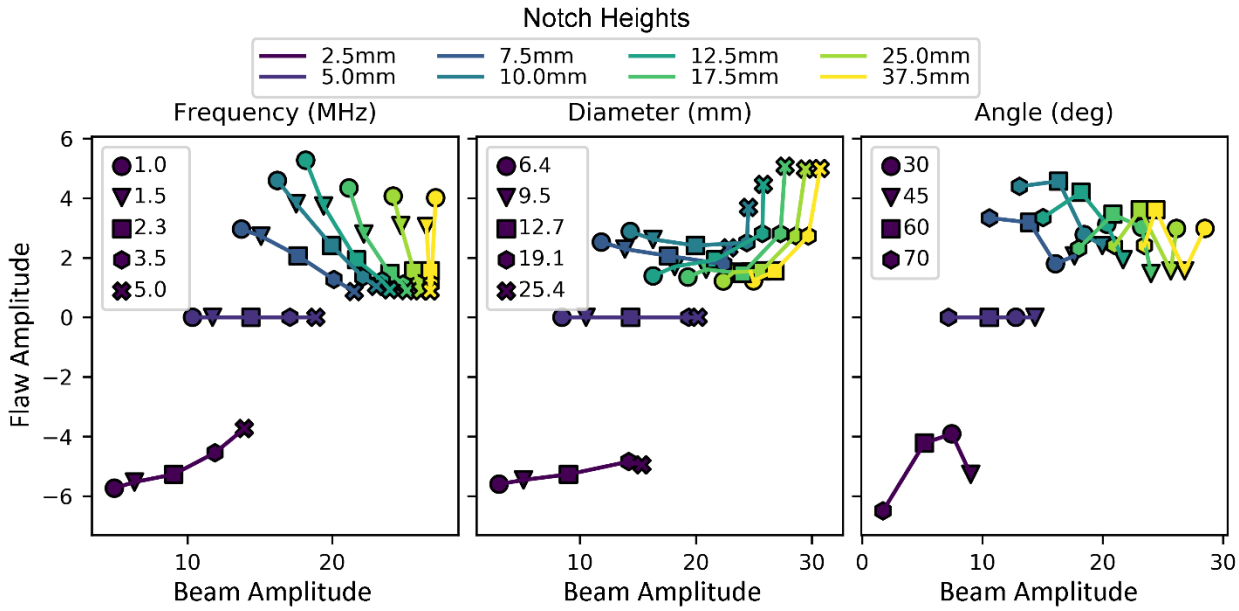

Figure 5.8. Normalized beam metric vs. normalized flaw backscatter amplitude for the shear wave probes and for eight different notch heights. One probe parameter was changed at a time—frequency (*left*), diameter (*center*), and beam angle (*right*).

Figure 5.8 shows that the effects of varying incident angles and beam focusing as a result of increased element sizes are not monotonic. As described in the previous section, this is due to the non-linear dependency of flaw amplitude on the incident beam for both the reference flaw and the flaw of interest.

Figure 5.9 shows the normalized beam metric versus normalized flaw backscatter amplitude for the TRL probes and may be compared to the data shown in Figure 5.6. Note that for a 1.0 MHz probe (left panel in Figure 5.9), the flaw with height 2.5 mm (0.10 in.) has an amplitude larger than the reference flaw with height 5 mm (0.20 in.). The likely source of this discrepancy was the overlap of the tip diffracted signal with the specular response, resulting in constructive interference, and hence the slightly larger amplitude than the reference flaw.

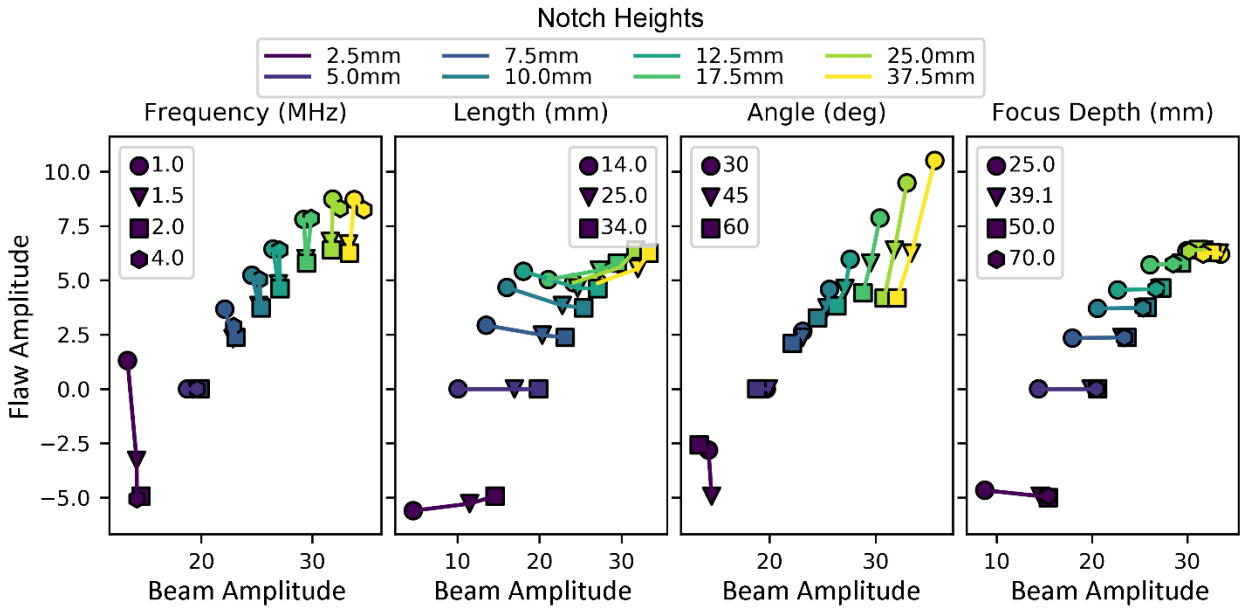

Figure 5.9. Normalized beam metric vs. normalized flaw backscatter amplitude for the TRL probes with eight different notch heights. One probe parameter was changed at a time from left to right—frequency, probe size (length x width), beam angle, and focal distance.

The combination of data from all 23 simulated probes for each of the 8 different notches demonstrates no consistent relationship between the normalized beam metric and normalized flaw amplitudes (Figure 5.10), unlike the non-normalized case. This is likely due to the normalization process removing effects related to variations in the overall beam profiles. The results illustrate the influence of transducer parameter specification on simulation results and indicate that unknown normalization effects in simulation software may impact the interpretation of simulation results. The primary conclusion that may be drawn, therefore, is that interpretation of beam simulation results in terms of flaw detection capability is challenging. One way to assess UT reliability with models is to use flaw response models. However, additional challenges are inherent for assessing UT reliability, even with flaw response models, as adequate care must be taken to address unknowns in model implementation and normalization procedures, uncertainties in material property specification, and uncertainties in transducer parameters.

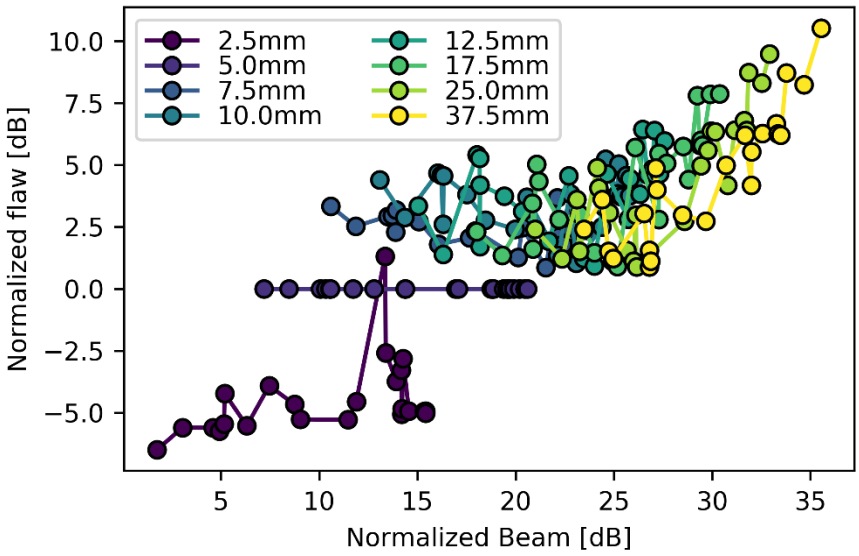

Figure 5.10. All different probes using the normalized beam metric.

5.3 Partial Access and Insonification

In the partial access scenario, the probe is limited to scanning only a portion of the specimen surface. In practice, this might be due to several factors, such as physical limitations due to surface geometry or the presence of other components. A complete assessment of the reliability of flaw detection under limited access conditions is outside the scope of this report. Here, we extend the study in Section 5.2 and evaluate the possibility of quantifying flaw detection using beam simulations when the probe is limited in its ability to scan fully over the flaw.

A scenario where a probe has limited access is shown in Figure 5.11. The access limitations in scanning limit the ability to obtain complete echo-dynamic data from the flaw. As a result, the flaw amplitude is likely to be limited, particularly if the scan is unable to capture the specular reflection from the flaw corner. For example, Figure 5.11(middle), shows the case where the ultrasound beam within the scan range would not insonify the flaw. The graphic shows a cross section of the scan volume (darker region) assuming the probe's scan range as shown and the ultrasound beam at each probe position is thresholded at −20 dB. Figure 5.11(bottom) shows a case where partial insonification of the flaw is possible and the flaw corner is within the insonification volume (again, assuming a −20 dB threshold on the ultrasound beam at each probe position).

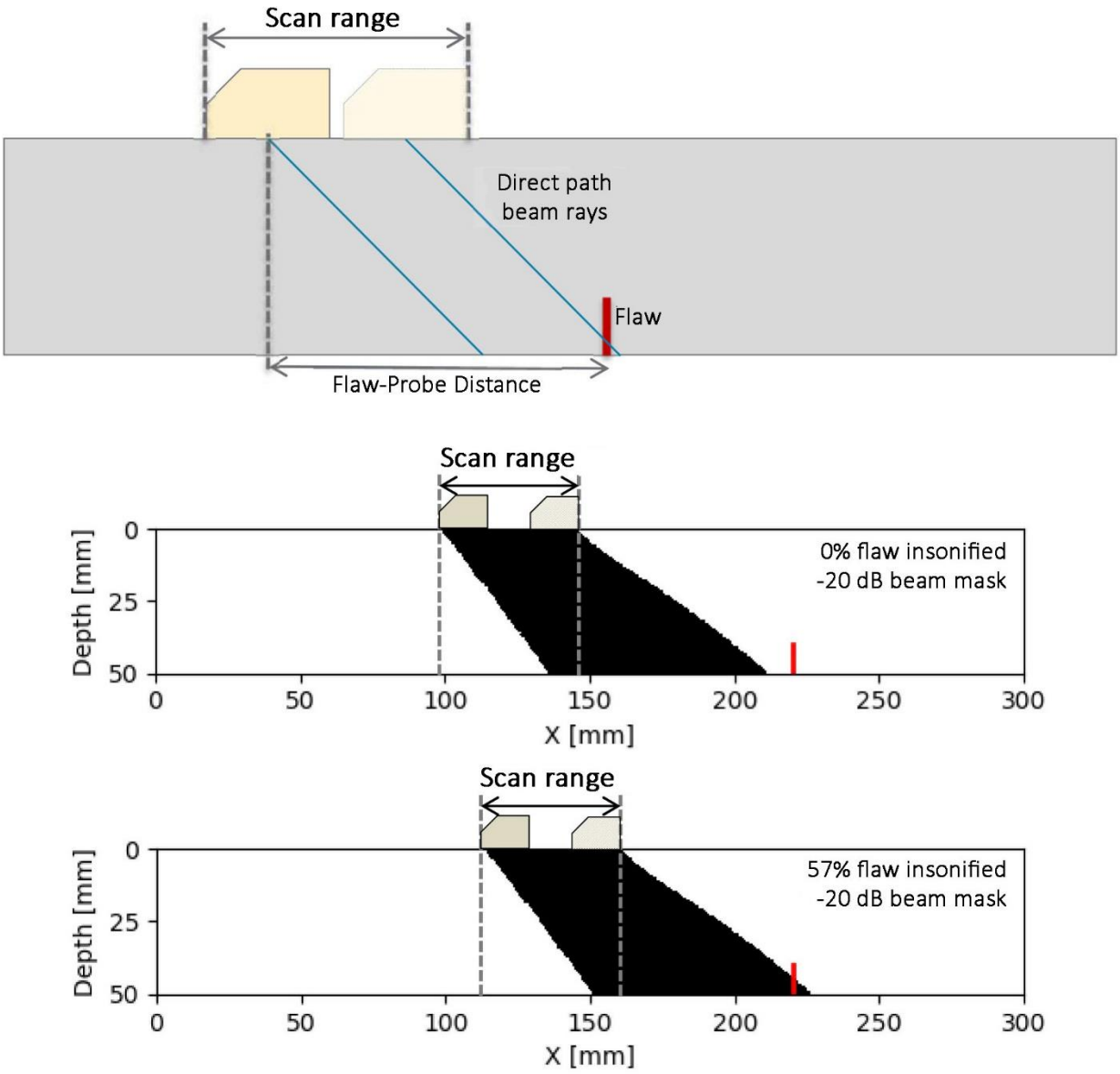

Figure 5.11. Example of a scenario where a probe has a limited scan range due to access restrictions at the specimen surface. The middle panel shows no flaw insonification and the bottom panel shows partial flaw insonification.

Results presented in the previous section indicate that the relation between flaw backscatter and the beam is highly non-linear. Therefore, inferring relative flaw amplitude based on beam simulations is challenging.

In this section, we limit the probe's scan range so that the full flaw echo-dynamics are not captured. We then compute the maximum flaw signal as the flaw-to-probe distance varies, as defined in Figure 5.11. As an example, Figure 5.12 shows the B-scan and the total effective beam incident onto a 25 mm (0.98 in.) notch (50% through-wall), using a 1 MHz, 0.5-inch diameter, 45° shear wave probe. The partial scan means that the complete echo-dynamic signal is not available (evident in the partial responses in the B-scans in Figure 5.12). Figure 5.12, right, shows the volume covered by the composite beam obtained by overlaying the beam

simulations from all scan locations. These simulations show that the beam energy does not fully insonify the flaw under a partial access scenario.

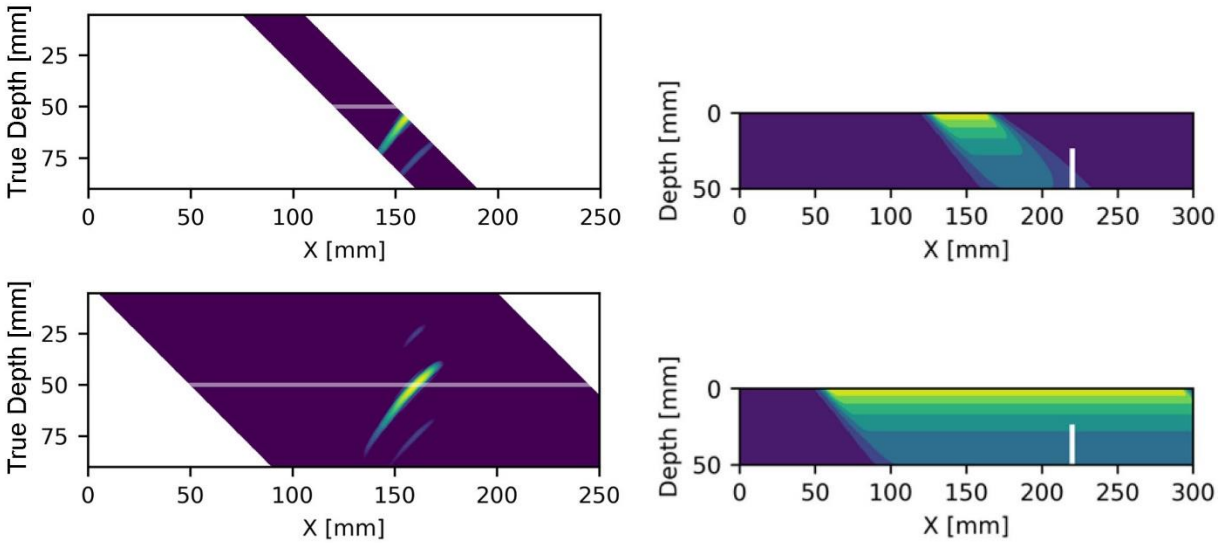

Figure 5.12. Example of partial access simulations as seen by the B-scan (*top left*), and the total beam incident onto flaw (*top right*). The bottom panels show the full access scenario for reference. In the B-scans, the horizontal line indicates the specimen backwall. In the beam plots, the vertical line shows the flaw location and size (through-wall depth).

We use the geometry and probes described and used for the simulations in Section 5.1, to understand the relationship between the normalized beam amplitude, beam ray paths, and the flaw amplitudes. Figure 5.13 shows both the flaw amplitude (shades of red) and beam metric (shades of green) as the distance between flaw and probe changes (see Figure 5.11). A flaw-to-probe distance of 0 mm corresponds to the case when the probe is placed such that it is right on top of the flaw. Negative positions refer to the cases when the probe is in front of the flaw (beam is going away from the flaw). Positive positions refer to the cases when the probe is behind the flaw (beam is moving toward the flaw). The allowed probe scan range is 30 mm (1.2 in.). Three representative cases out of all simulated 23 probes are shown in Figure 5.13. Similar trends were observed for the other probes.

For the flaw amplitude curves, there is a range of flaw-to-probe distances (x-axis in Figure 5.13) where the amplitude is maximal. This corresponds to the flaw location in which the scan range catches the corner echo. The flaw amplitude rapidly decreases when the scan range does not include the corner. In the case of the total beam metric, we see similar trends. There is a range of locations where the flaw is able to be insonified in a manner that maximizes the total beam energy incident on the flaw.

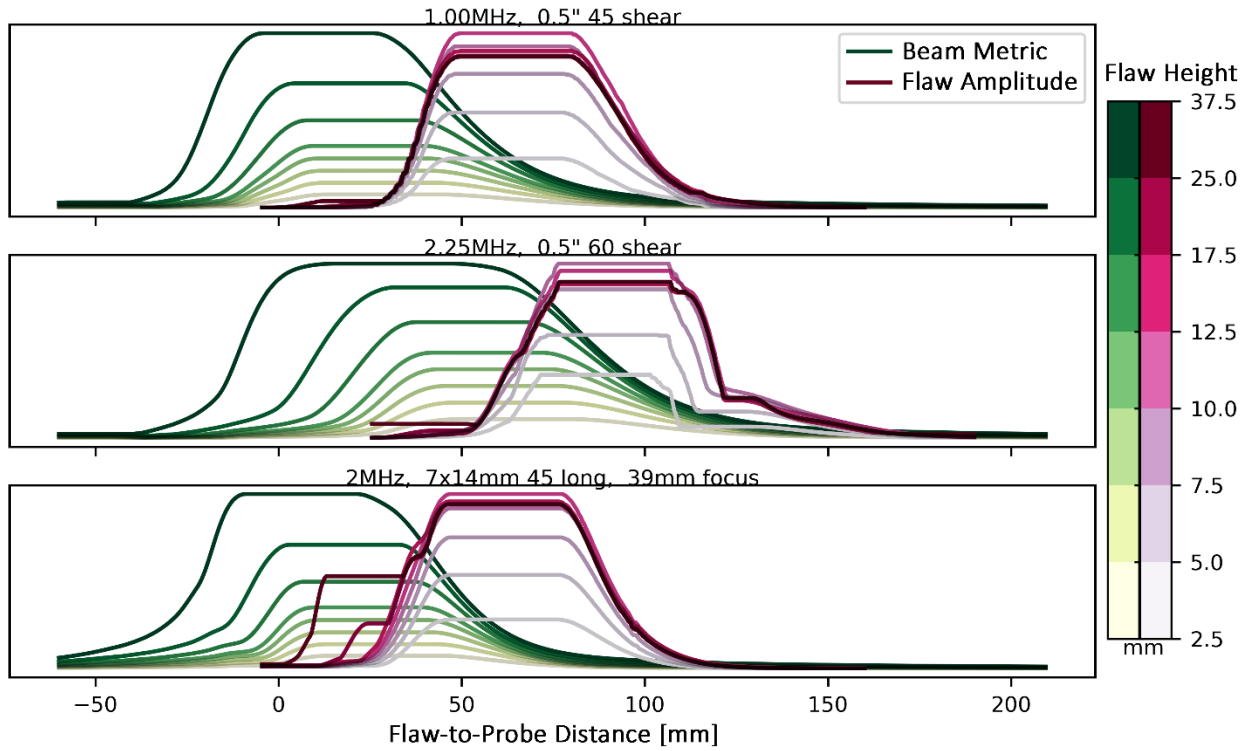

Figure 5.13. The flaw backscatter amplitude vs. flaw-to-probe distance is shown in shades of red. The total beam amplitude incident onto the flaw for different flaw-to-probe distances is shown in shades of green. The different shades refer to different flaw sizes, as indicated by the color bars.

The most important observation from Figure 5.13 is that the probe locations that attain a maximum total beam amplitude are different from those which achieve maximum backscattered energy from the flaw, resulting in maximum flaw amplitudes. The flaw amplitude is maximized when the probe is behind the flaw by approximately the *specimen thickness* $\times$ tan θ, where θ is the beam angle. However, we do not see a maximum in the beam metric until the probe is much closer to the flaw. In addition, the beam metric does not roll off to zero until the probe has passed to the front of the flaw.

This difference is likely due to many factors. In particular, backscattering of energy from the flaw can occur when the beam reflects off the backwall and then the flaw, resulting in a greater flaw amplitude prior to significant beam energy directly incident on the flaw Figure 5.14. However, when the probe is directly above the flaw, there is a larger amount of energy incident onto the flaw with a lower amount of energy backscattered toward the transducer.

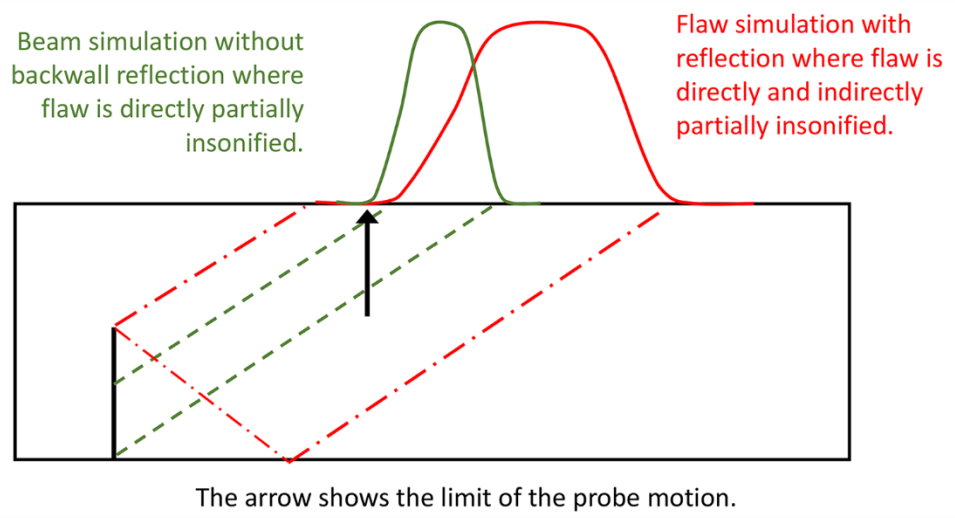

Figure 5.14. Schematic showing the relationship between probe motion, beam paths, and partial insonification of flaw that may partly explain differences observed in Figure 5.13.

To verify this effect (reflection of energy from the backwall, followed by reflection from the flaw), we conducted beam simulations in which the reflection of the beam from the backwall as well as the beam direct path were computed, as shown in Figure 5.15. The figure shows an example of the ultrasound beam from a 1 MHz, 12.7 mm (0.5 in.) diameter, shear wave probe with the incident energy in the part at 45°. Figure 5.15 (top) shows the ultrasound beam computation if no reflection from the backwall is computed, while Figure 5.15 (bottom) shows the beam energy including that reflected from the backwall. The beam metric described earlier was recomputed to include the reflected energy off the backwall. The results for the beam metric and backscatter amplitude for different probe-flaw relative positions are shown in Figure 5.16.

Using these more complete simulations, we see that the beam metric (green curves) is bimodal for shear wave probes. This is due to the additional contribution from the backwall-reflected energy that is incident on the flaw. It appears that accounting for this additional contribution better explains the behavior of the beam metric and flaw amplitude as a function of the probe-to-flaw distance. This result confirms that, in this case, the maximum flaw amplitude occurs when the beam reflects off the backwall first, and is not from the direct beam on the flaw.

It is noteworthy that the bimodal behavior is not observed in the simulated data from dual-element TRL probes (compare the bottom panel of Figure 5.16 to the top two panels). This is likely due to scenarios where the probe cross-over zone that defines the TRL “focusing” effect and depth of field is not always optimal for the dimensions of the mockups used in the evaluation, essentially limiting the likelihood of obtaining a coherent backwall reflected signal.

Collectively, the results show that for a given probe, calculated beam maxima may be spatially offset from the probe locations where the flaw amplitude may be maximum. Regions corresponding to maximum insonification (total beam amplitude) may correspond to small flaw amplitudes, and vice versa. Using models that compute both the direct *and* backwall reflected beam paths appear to improve this correlation for single-element probes. It is not yet clear what additional information would be needed to improve this correlation for dual-element and phased array probes, or whether this finding is true in all cases or only in the specific cases described in this report.

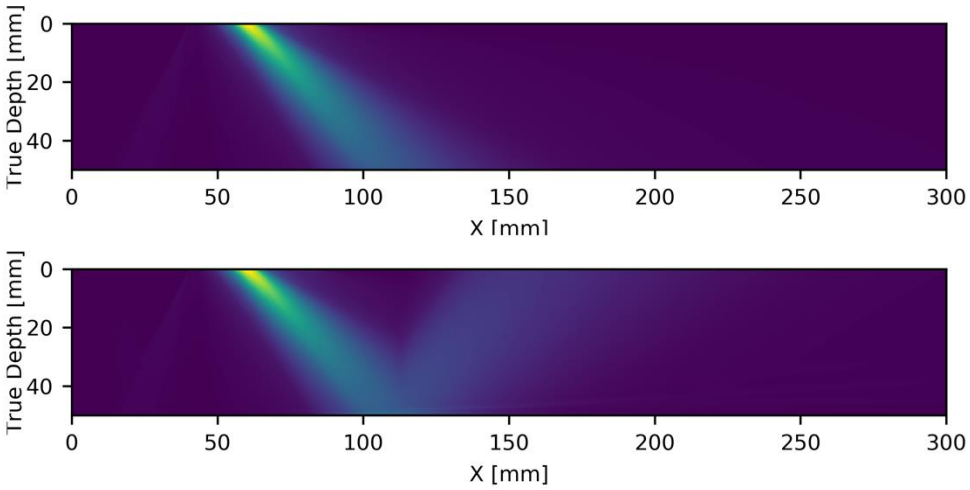

Figure 5.15. Beam for a 1 MHz, 0.5 in. diameter, 45° shear wave probe. Only direct beam (*top*), direct + backwall reflected beam (*bottom*).

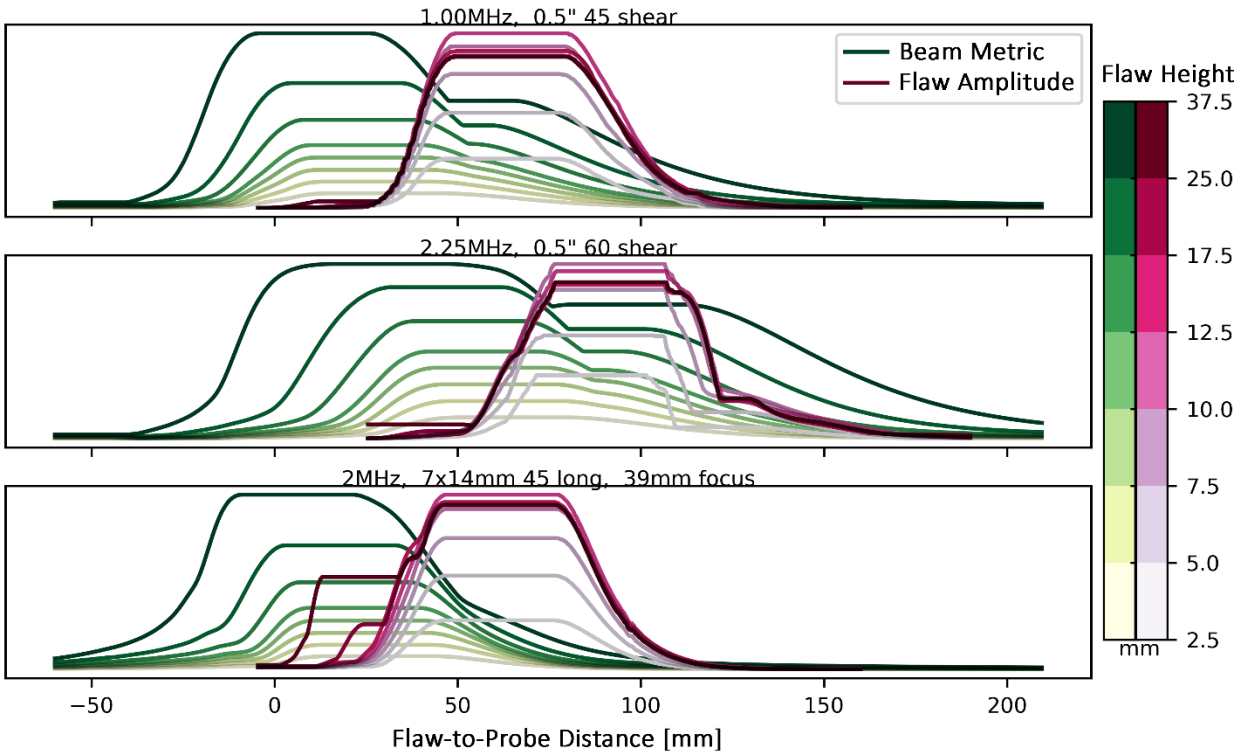

Figure 5.16. The flaw backscatter amplitude vs. flaw-to-probe distance is shown in shades of red. The total beam amplitude (direct + backwall reflected) incident onto the flaw for different flaw-to-probe distances is shown in shades of green. The different shades refer to different flaw sizes, as indicated by the color bars.

5.4 Summary

In this section, we described the results of simulations using beam models and flaw computation models to understand the extent of information that beam models provide relative to flaw detectability. Flaw signal amplitude was used as a proxy for flaw detectability. We found that the relationship between sound energy incident on a flaw and the expected flaw amplitude was a complex function of several factors. Regions corresponding to maximum insonification of the flaw may correspond to very small flaw amplitudes. Normalization appears to not be a significant factor in these conclusions, though the use of normalization changed the interpretation of the relationship between the beam metric and flaw amplitude, as described in Section 5.2.2.

Given these findings, we conclude that the beam amplitude incident on a flaw does not appear to be an informative measure of expected flaw detection reliability. As a corollary, comparing the performance of probes with respect to flaw detection capability will likely require additional information beyond the amount of ultrasound energy incident in a volume. Finally, simulation models will need to effectively accommodate noise and include the effects of beam interaction with the backwall and other geometric factors to accurately compute the total beam energy incident on the flaw, and the interaction of the energy with the flaw itself, to obtain a comprehensive understanding of flaw detection capabilities in both full and limited coverage scenarios.

6.0 Flaw Response Model in Austenitic Welds

As discussed earlier, modeling of sound propagation through welds is complicated by the fact that welds are heterogeneous, anisotropic regions with varying crystallographic orientation throughout the weld volume. This anisotropy and non-homogeneity results in attenuation, redirection, and scatter of sound propagating through the weld.

Section 2.0 discussed multiple techniques for microstructure representation of welds for the purpose of modeling sound propagation at wavelengths generally of interest in UT. Section 4.0 showed that welds cause beam skewing and redirection, with the effects qualitatively captured by models. However, quantitative matches of the beam profiles between simulation and experiment require greater fidelity in the material properties used in the model.

In this section, we investigate the use of flaw response models for predicting B-scan images in specimens that contain flaws close to welds. The purpose of this work is to identify proper procedures for defining general weld models, evaluate required accuracy of model inputs, and validate the accuracy of the model itself for weld simulations.

We use the Ogilvy weld parametrization model combined with the dynamic ray tracing model (Section 2.0) to predict ultrasound B-scan images. The Ogilvy weld parametrization model significantly reduces the number of parameters and the extent of knowledge needed to model a weld structure. This makes using the Ogilvy model more practical than other detailed weld specification methods, which require more complex definitions of the weld dendritic structure. However, the tradeoff for practicality may be simulation accuracy.

To appropriately evaluate weld models, we need to specify the intended use of such models. In this work, we direct our focus to the following two issues:

- Sound scattering due to heterogeneous weld structure results in signal “clutter” as a result of multiple scattering from weld interfaces, weld root, and counterbore. It is important for a model to reproduce such expected clutter accurately, as the presence of clutter may challenge the ability to discriminate signal responses and reliably detect flaws.
- The flaw specular backscatter amplitude. This amplitude essentially controls the SNR and influences detection reliability. Note that we do not simulate the noise in this study; this will be considered in follow-on studies and will be documented in a subsequent report.

We investigate three types of inspections typically used in NPP inspection: shear wave, dual-element TRL, and phased-array TRL.

In this section, we first describe the measurement matrix and experimental procedures used to obtain responses from both thermal fatigue cracks and machined flaws (saw-cut reflectors). Cases where the flaw is located at the weld far side and near side are considered. We then analyze the B-scan (side view) and C-scan (top view) images to identify the important aspects of the measurement that can cause missed calls and false calls. We compare resultant B-scans from experiments and simulations to identify potential shortcomings of models for use in NDE reliability. We also compare computed flaw specular amplitudes from experiments and simulations.

6.1 Specimen, Probes and Experimental Procedures

In this study, we used scans from a WSS 120° pipe section containing an austenitic weld. The section is 36 mm (1.4 in.) thick and has a 610 mm (24 in.) outer diameter, as described in Anderson et al. (2011). The cross-sectional view of the specimen and weld design specifications are shown in Figure 6.1. A saw-cut flaw with length 65.2 mm (2.6 in.) and maximum height of 10.2 mm (0.4 in.) was added to the specimen at a distance of 7.6 mm (0.3 in.) from the weld root center. The specimen was then scanned using three probes:

- Longitudinal-wave, dual-element TRL probe, 34x20 mm (0.8x1.34 in.) rectangular dimensions for each element, 2 MHz, 40 mm (1.58 in.) focal depth, and 45° angle through base material.
- A 2 MHz phased-array, dual-matrix TRL probe (10x5 elements). The phased-array was used to transmit and receive the longitudinal wave mode at a 45° angle and 35 mm (1.38 in.) depth focus.
- Shear-wave, single-element, 12.7 mm (0.5 in.) diameter, 2.25 MHz, and 45° angle through base material.

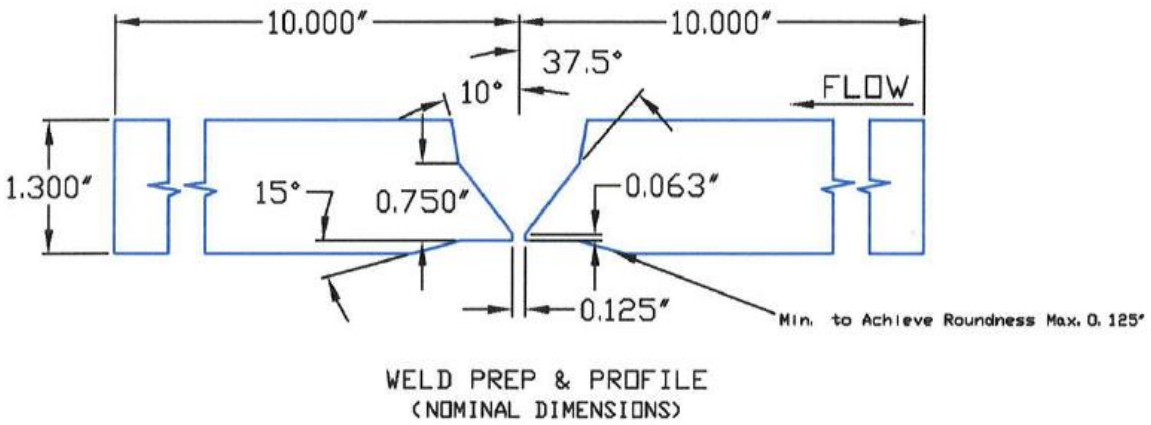

Figure 6.1. Specimen cross-sectional view, including the weld profile. Dimensions are in inches. This view does not show the saw-cut flaw.

In addition to scanning the saw-cut reflector, the specimen end-of-block was also scanned to obtain a reference signal that could be used to calibrate the reflector responses. The calibration allowed direct comparison of amplitudes in both simulations and experiments. The experimental scan setup is shown in Figure 6.2. A DYNARAY scanning system was used, and the reflector was scanned with a resolution of 0.5 mm (0.02 in.) in the scan direction and 1 mm (0.04 in.) in the index direction.

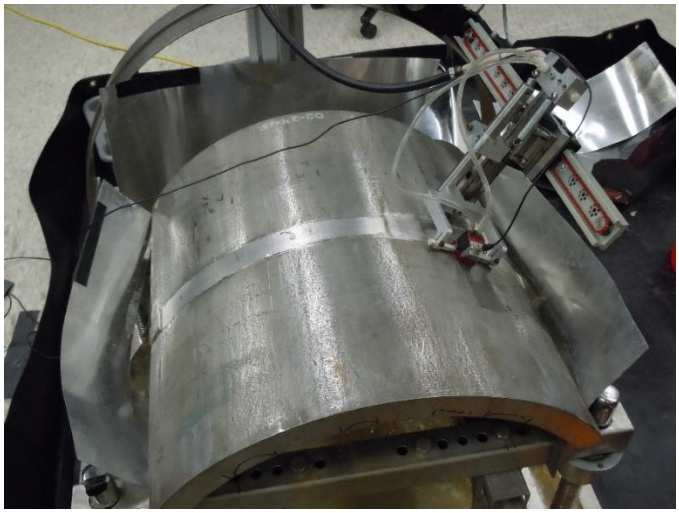

Figure 6.2. Experimental scan setup with the specimen.

6.2 Simulation Specification in CIVA

Multiple simulations were conducted in CIVA, replicating the parameters used for the empirical data measurements. The specimen and weld profile geometries were defined by 2D Computer Aided Design (CAD) drawing. Then, the 2D CAD drawing was revolved into a 3D geometry at a 610 mm (24 in.) diameter and over a 120° circumferential pipe segment. The resulting geometry resembled a segment of a 610 mm (24 in.) diameter pipe, similar to that shown in Figure 6.2. An elliptical surface-breaking flaw with the same dimensions as those of the empirical measurements was defined within the specimen. The specimen base material was specified as isotropic steel with density 7800 kg/m^3, shear wave velocity of 3230 m/s, and longitudinal wave velocity of 5800 m/s. These material properties represent the nominal values for stainless steel. The weld was defined based on the Ogilvy weld parameterization (Section 2.2). The parameters D and α for the weld parametrization were specified to be 1.6 mm (0.06 in.) and 37.5°, respectively, based on the geometry in Figure 6.1. The parameters T and η were both set to 1, in the absence of additional information on the weld morphology.

The material properties for the weld were specified to have cubic symmetry with C_{11} = 245 GPa, C_{12} = 145 GPA, and C_{44} = 110 GPa. The corresponding slowness curves in the X–Z plane are shown in Figure 2.1, and were generated in CIVA based on the specified stiffness matrix.

Probe and wedge dimensions were measured from the empirical setup and used as input to the simulation. The probe center frequencies and bandwidths were estimated from the probes' responses from the specimen end-of-block. The input signal spectral shape was specified as Gaussian, although experimentally we do not obtain a perfect Gaussian spectrum. To minimize the simulation computing time, only axial line scans (probe scanned along the axis at one circumferential position) were considered with a 1 mm (0.04 in.) step size. In addition, a "computational zone" was defined to limit the volume considered for computation at each scan point. The computational zone was large enough to capture any reflections from flaws or material. For the shear wave transducer, only the shear mode was specified for computation. For longitudinal wave transducers (dual-element and phased array), only longitudinal wave modes were computed. Two scan skews were simulated—one where the flaw and probe were on the same side of the weld (near side) and one where the probe and flaw were at opposite sides of the weld (far side).

6.3 Simulation Results and Discussion

In this section, we analyze some of the empirical measurements and characterize the different echoes that can be seen in B-scan images. All B-scan images were corrected by skewing the image at an angle based on the beam propagation direction in base material. The intent of the results described in this section is to demonstrate what one might expect from a simulation of complex scenarios such as a weld inspection. In the following section, we will divide our analysis into three parts—longitudinal waves, phased array longitudinal waves, and shear waves.

6.3.1 Longitudinal Wave Mode with TRL Probes

In this section we describe the results for both near side and far side inspections using a 2 MHz TRL probe at a 45° beam incident angle. Figure 6.3 shows B-scan images for a dual-element longitudinal probe at 2 MHz and a 45° angle for both experiment and simulation. The experiment results (top panel) show a highly cluttered B-scan. The specular response from the flaw can be seen among other echoes from the specimen backwall and reflections from the weld root. The specular echo in the experiment and simulation B-scans have similar dynamics, although there are some differences due to uncertainties in material properties and pulse shape, as described previously. The simulation B-scan does not show such noise or clutter, which is to be expected as there was no specification of structural noise, mode conversions, or computation of specimen echoes in those simulations. To better understand the sources of different echoes in the experimental B-scan, we plot the C-scan view in Figure 6.4. For the near side inspection C-scan (left panel), we can see three distinct echoes representing each of the flaw, weld, and mode-converted signals.

Figure 6.5 shows the results from the same TRL probe for a far side inspection. In the experiment B-scan (top panel), we see that the weld root echo is much stronger than the echo from the flaw. This can be seen clearly from the experiment C-scan in Figure 6.4 (right), where the root echo overshadows the specular response from the flaw. The simulation B-scan (Figure 6.5, bottom) shows a clear specular response; however, the tip response is below −20 dB and cannot be seen in this B-scan view. Also note that the specular response in the simulation is in a different location than in the experiment, likely due to the approximate definition of the weld dendrites.

Finally, we compute the calibrated flaw specular echo amplitudes relative to the responses from the specimen end-of-block. As discussed earlier, calibration normalizes the signal amplitudes and enables a one-for-one comparison between simulation and experiment (Dib et al. 2017). In addition, calibration relative to a known reflector (EPRI 2013) is the standard method for equipment calibration in the field.

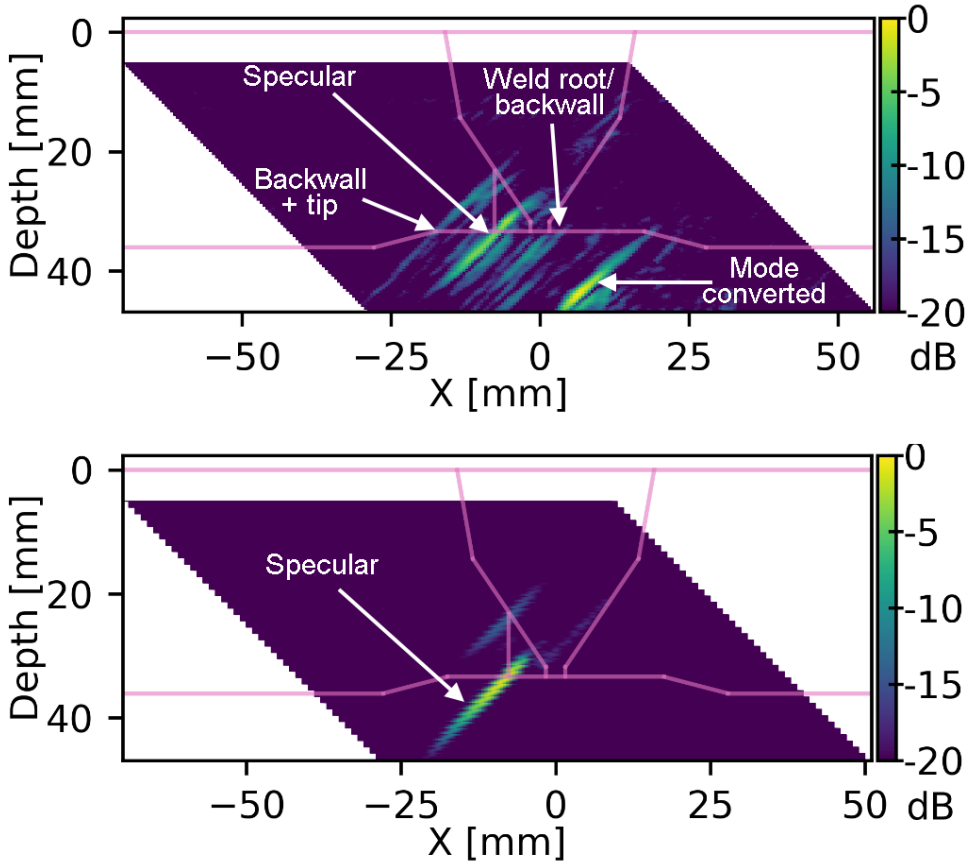

Figure 6.3. **B-scan for near side inspection using a dual-element TRL probe at 2 MHz, 45° longitudinal wave. *Top*: experiment, *bottom*: simulation. The weld profile and location of saw-cut flaw are overlaid on the B-scan. The B-scans are normalized to their own maximum signal amplitude. The color maps span amplitudes down to −15 dB from the maximum.**

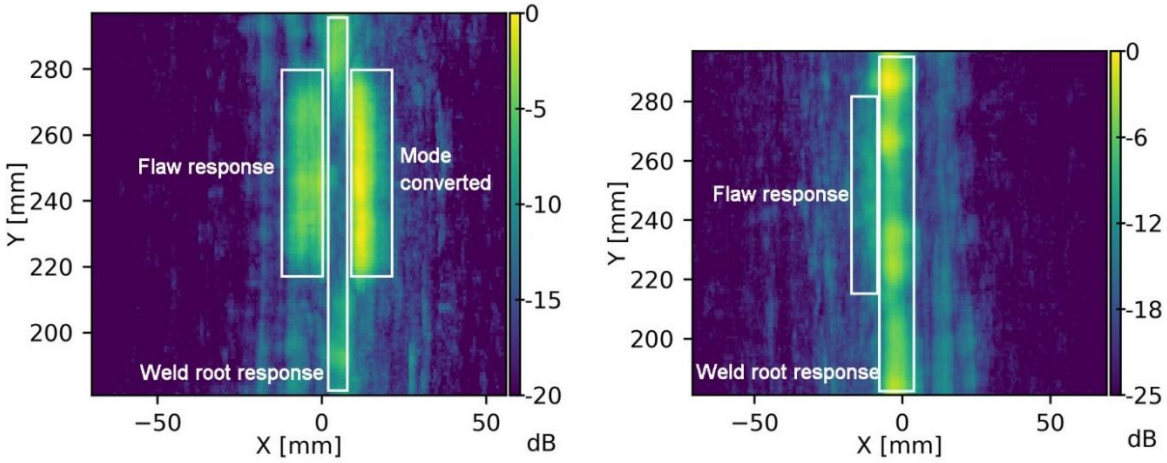

Figure 6.4. **Experimental C-scan using the dual-element TRL probe at 2 MHz, 45° longitudinal wave. *Left*: near side inspection, *right*: far side inspection. The C-scan is normalized to its own maximum amplitude.**

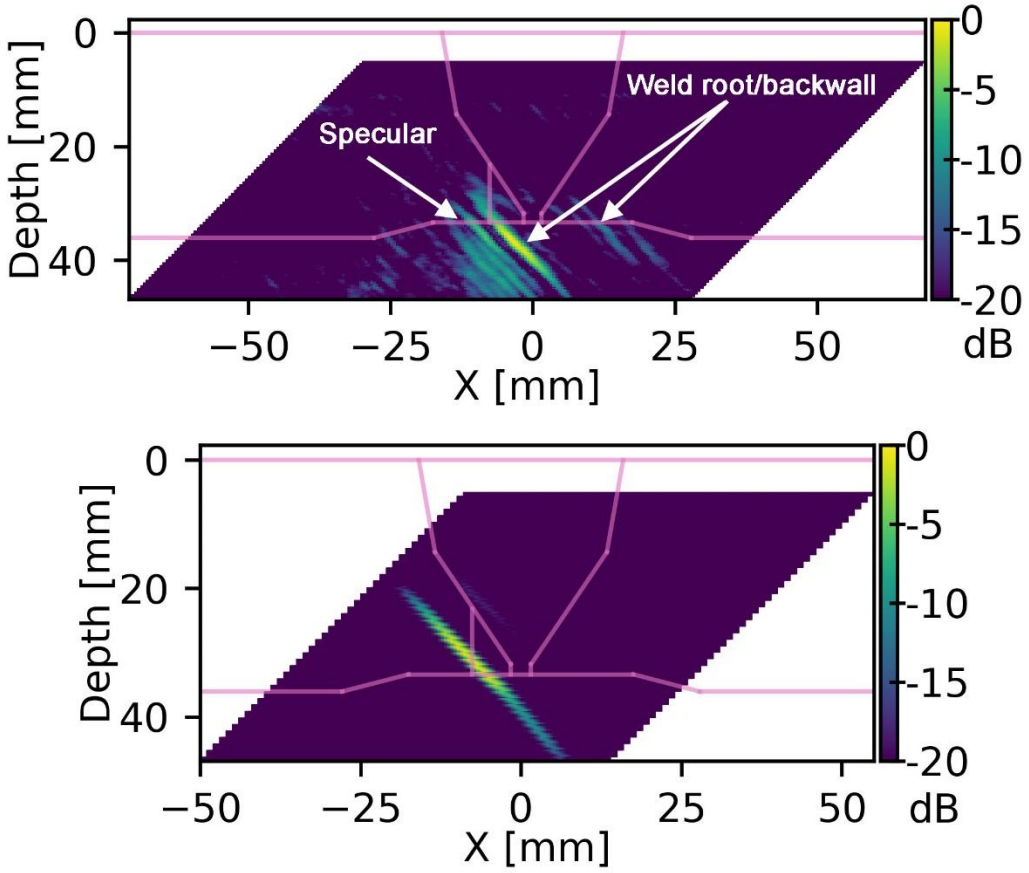

Figure 6.5. B-scan for far side inspection using a dual-element TRL probe at 2 MHz, 45° longitudinal wave. *Top*: experiment, *bottom*: simulation. The weld profile and location of a saw-cut flaw are overlaid on the B-scan. The B-scans are normalized to their own maximum signal amplitude. The color maps span amplitudes down to −20 dB from the maximum.

The specular echo from the specimen end-of-block (reference signal) in the experiment resulted in large variations in amplitude that depended on the scan position. An analysis of the data, along with additional measurements from the specimen end-of-block at different locations, led to the conclusion that the variation was due to roughness of the specimen end-of-block and not due to coupling variations. Given the variability, we decided to report experimental results using a 95% confidence interval computed using all (117) measured amplitudes of the end-of-block reflections. It is important to note that this confidence interval only represents variations in the end-of-block response, and not any other uncertainties that might occur during experimental data collection.

We also computed the maximum amplitude of the clutter from the weld and backwall for the experiment as well as the normalized noise floor. These are reported using the 95% confidence bounds as well. We do not compute clutter amplitude for simulation, because reflections from interfaces and specimen boundaries were disabled in the model.

The calibrated amplitudes for the near-side and far-side inspections are shown in Table 6.1. The confidence interval for the experiment flaw response varies by about −4 dB. The simulation over-estimated the flaw specular response amplitude by 5–10 dB for near side inspection and 2.5–7 dB for far side inspection. We also see that the noise floor was about −24 to −31 dB, which is much lower than the flaw amplitude. Thus, structural noise and thermal noise were not a large factor in these inspections. On the other hand, we see that clutter is significant, especially for far-side inspections where it may have amplitudes as high as −1 dB, masking the flaw response and limiting the ability to reliably detect flaws. It is, therefore, important to have simulations that compute the interactions with geometric features reasonably accurately. The results also illustrate the impact of uncertainties in model specifications (material properties, limited specification of geometric conditions, etc.) that may contribute to the differences between simulation and empirical results. Consequently, there is a need to use stochastic methods to validate models and when applying simulation models for estimating NDE reliability. With stochastic methods, input parameters to the model are treated as probability distributions rather than a point estimate. Multiple simulations are then performed, with input parameter values taken from the probability distributions. The result is a probability distribution for the model output that defines the probability of occurrence of different values (such as flaw response amplitudes) based on the range of input values.

Table 6.1. Calibrated Amplitudes for the Saw-Cut Notch Using a Dual-Element TRL Probe

	Experiment 95% confidence (dB)	Simulation (dB)
Near side – flaw	[−10, −5.6]	0.2
Near side – clutter	[−9.2, −4.8]	
Near side – noise	[−29, −24.5]	
Far side – flaw	[−12.3, −7.9]	−5.2
Far side – clutter	[−5.1, −1.1]	
Far side – noise	[−31.6, −27.2]	

6.3.2 Longitudinal Wave Mode Using Phased Array

Phased-array probes allow focusing and steering of sound beams and provide potentially higher resolution and improved SNR over their single-element probe counterparts. In this section, we describe initial results of using a phased-array probe for flaw detection in the presence of welds. The phased-array probe in this study was focused at a depth of 35 mm (1.38 in.) (just above the specimen backwall) and emitted a beam at a 45° angle from the specimen normal. The B-scans for the saw-cut with a 10×5 matrixed phased-array probe, near-side inspection, are shown in Figure 6.6. Assessing the experimental results (top panel), a major difference can be seen between using this phased-array probe and the TRL probe in Section 6.3.1. For the phased-array probe, the tip signal from the saw-cut appears to be greater relative to the specular echo and the experimental noise levels are lower. The B-scans for the far-side inspection are shown in Figure 6.7. In this case, the experimental data appear to be more cluttered and noisy than its near-side counterpart. As with the TRL probe, the signal from the weld root is much more prominent than that of the flaw. However, we have sufficient resolution to distinguish the flaw in this case. In addition, the flaw tip on the far side has higher intensity. The simulation, however, only contains the specular echo from the flaw, as expected, due to the way the model was defined. The tip echo can still be seen, but it appears to have lower intensity than in the near-side scan.

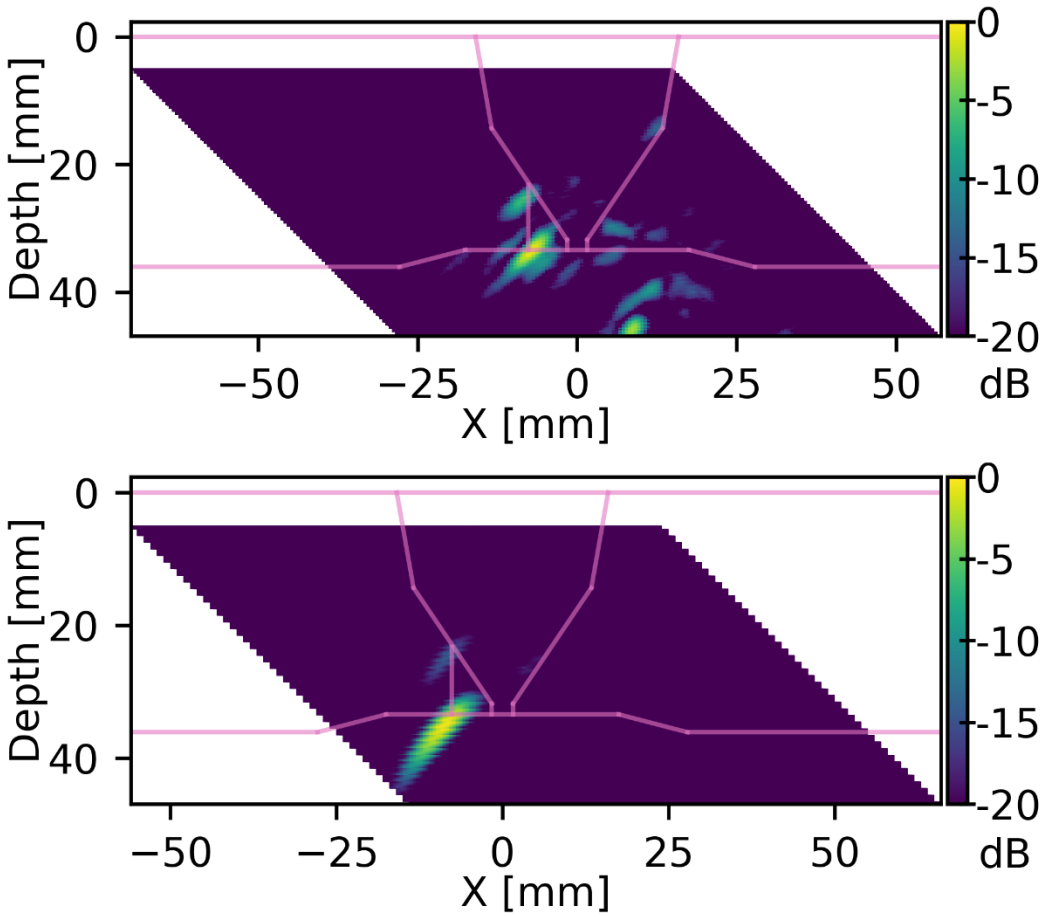

Figure 6.6. **B-scan for near-side inspection using a 10x5 phased array longitudinal probe at 2 MHz, 45° longitudinal wave, and 35 mm (1.38 in.) depth focus. *Top*: experiment, *bottom*: simulation. The weld profile and location of the saw-cut flaw are overlaid on the B-scan. The B-scans are normalized to their own maximum signal amplitude. The color maps span amplitudes down to −20 dB from the maximum.**

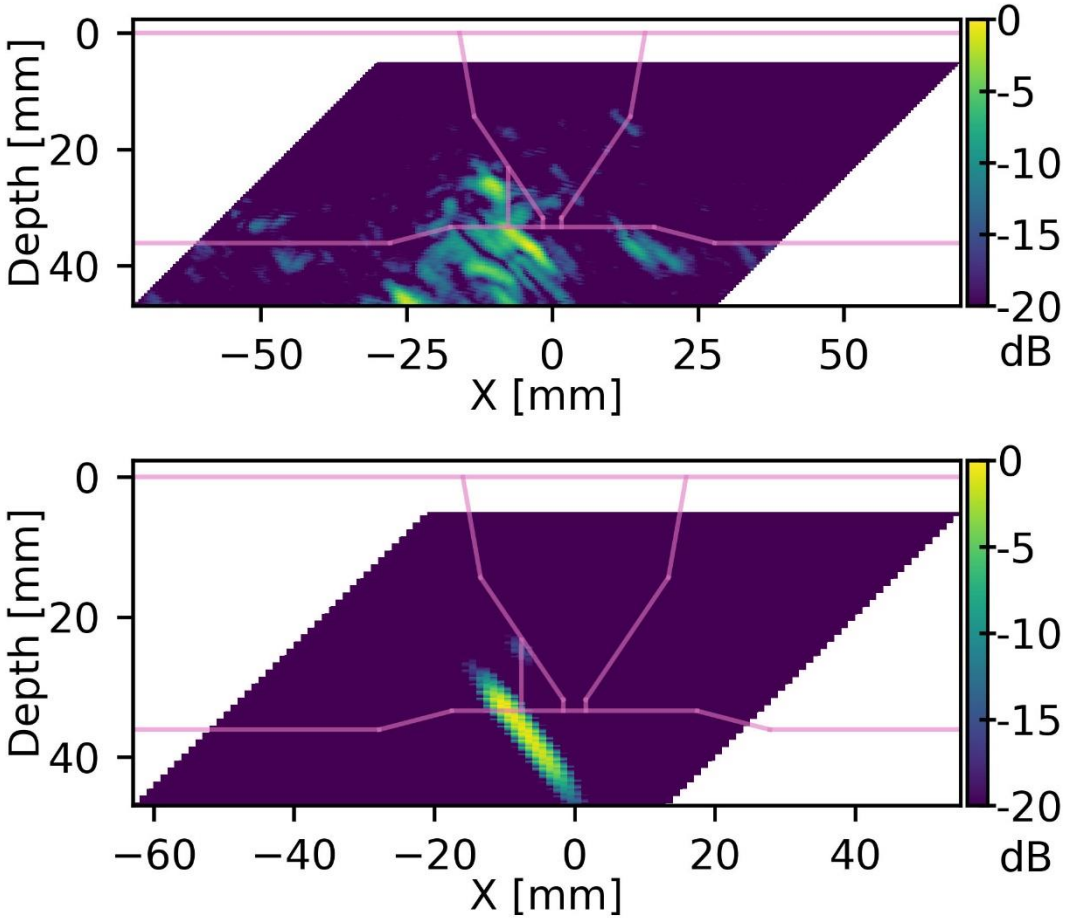

Figure 6.7. B-scan for far-side inspection using a 10x5 phased array longitudinal probe at 2 MHz, 45° longitudinal wave, and 35 mm (1.38 in.) depth focus. *Top*: experiment, *bottom*: simulation. The weld profile and location of the saw-cut flaw are overlaid on the B-scan. The B-scans are normalized to their own maximum signal amplitude. The color maps span amplitudes down to −20 dB from the maximum.

The calibrated amplitudes (see Section 6.3.1) for the near-side and far-side inspections using the phased-array probe are shown in Table 6.2. The simulation lies within the 95% confidence range of the experiment for the near side inspection. Yet, the simulation significantly over-estimates the flaw specular amplitude for the far side inspection. Again, there are a number of uncertainties in model specifications that may contribute to this difference. The experimental noise floor is about −27 to −34 dB, again much lower than the flaw amplitude. However, we see that clutter is significant, especially for the far side inspection where it could have an amplitude as high as −1 dB, masking the flaw response. Again, this reflects the importance of accurate simulations that incorporate signals from geometries when evaluating the flaw detection capability.

Table 6.2. Calibrated Amplitudes for the Saw-Cut Notch Using a Phased Array Probe

	Experiment 95% confidence (dB)	Simulation (dB)
Near side – flaw	[−5.7, 0.1]	0
Near side – clutter	[−9, −3.2]	
Near side – noise	[−33.4, −27.6]	
Far side – flaw	[−18, −14.6]	−1.69
Far side – clutter	[−5.2, −1.7]	
Far side – noise	[−34.4, −30.9]	

6.3.3 Shear Wave Modes

Shear waves, though used for weld inspection, are subjected to greater beam deviations and scattering when propagating through austenitic welds (Adler et al. 1978; Kupperman and Reimann 1981). Simulations of this phenomenon may be performed using rays traced through a typical heterogeneous weld with cubic symmetry (Figure 6.8). The longitudinal waves (left) show little disturbance and ray splitting as they propagate through the weld and scatter from the flaw. On the other hand, shear waves (right) show extreme beam redirection and splitting, resulting in longer propagation paths and changes of direction within the weld. This is because waves in heterogeneous anisotropic media tend to follow the direction with the highest phase velocity. Based on a cubic symmetry definition, the phase velocity for shear waves changes much more rapidly than it does for longitudinal waves (see Section 2.2).

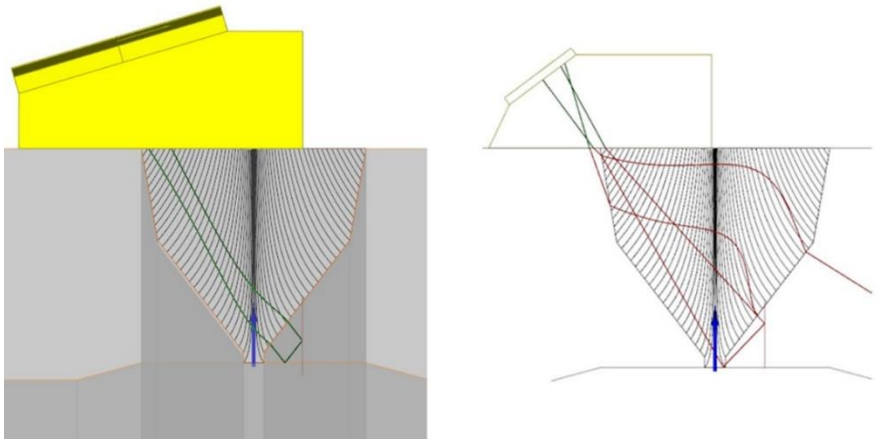

Figure 6.8. Ray tracing of the longitudinal wave mode (*left*), and the shear wave mode (*right*) in a weld with cubic symmetry, and heterogeneity defined using the Ogilvy geometric model.

The weld is defined using the Ogilvy geometrical model with the parameters defined as described in Section 6.2. No attenuation was defined for the weld or base material, and as in other instances discussed previously, the computed flaw amplitudes are likely to be lower when the effects of attenuation are factored into the simulation.

Shear waves are commonly used for near-side inspections in the nuclear industry, given their higher resolution (relative to longitudinal wave transducers). Figure 6.9 shows the B-scan from a 10 mm (0.4 in.) deep saw-cut notch using a single-element shear wave transducer at 2 MHz nominal frequency and 45° beam angle. The probe scan direction relative to the weld is such

that the flaw is on the near side. Thus, the ultrasound beam does not propagate through the weld to detect the flaw. Experimental data for the near-side inspection case show that, with a shear-wave transducer, only the specular echo from the flaw is received. We see similar results in the simulation B-scans. The differences in the specular echo shape are likely due to uncertainties in the material and probe definitions used to define the simulation model. The most significant parameter affecting this difference is the definition of the transmitted signal (signal generated by the transducer), which is an idealization of the experimental signal. In both the experiments and simulations, we do not see a tip-diffracted signal within the −20 dB threshold. This is likely because the tip of this specific flaw intersects with the weld interface, reducing the tip signal amplitude.

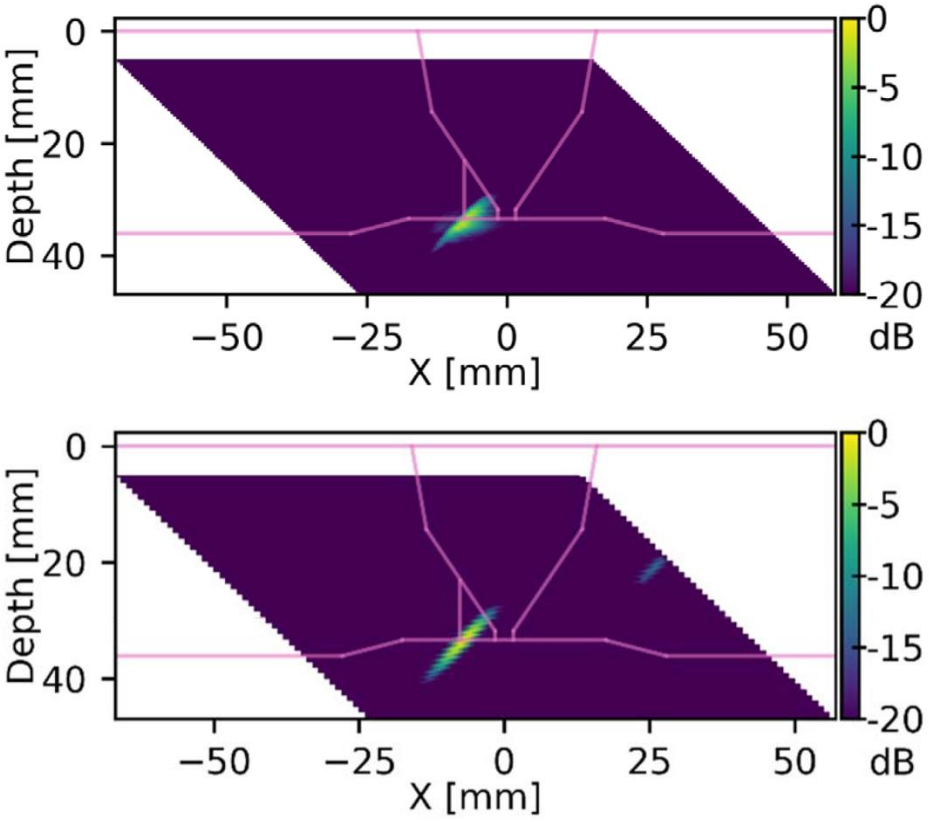

Figure 6.9. B-scan for near side inspection using a 0.5 in. diameter, 2 MHz, 45° shear wave transducer. *Top*: experiment, *bottom*: simulation. The weld profile and location of the saw-cut flaw are overlaid on the B-scan. The B-scans are normalized to their own maximum signal amplitude. The color maps span amplitudes down to −20 dB from the maximum.

A major difference between the experiment and simulation is the presence of an extra echo at approximately X = 25 mm (0.98 in.) in the simulation results. The source of this echo is illustrated in Figure 6.10. When the probe is positioned on the weld, the simulation indicates that there are two ray paths through the weld. One is a direct ray path, which propagates as expected at a 45° angle through the specimen. No echo will be received back due to this ray path as there is no corner reflector in its path. However, the simulation also uses a second ray path through the weld straight down to the backwall that results in the additional indication in the simulation results. This ray path is theoretically valid when using the Ogilvy geometrical definition of the weld. Note that it appears that the reflection is originating from the weld root

since the B-scan was corrected based on the assumption of base metal material properties. However, in practice, the weld is highly attenuative, and such an echo, even if it exists, is unlikely to be detectable. In this particular case, the extra echo in the simulation is sufficiently far from the flaw of interest, and can be safely ignored when analyzing the simulation results. In more complex scenarios, care must be taken to quantify the sources of various signals in the simulation and to possibly define appropriate attenuation parameters for the weld material so such signals are suppressed.

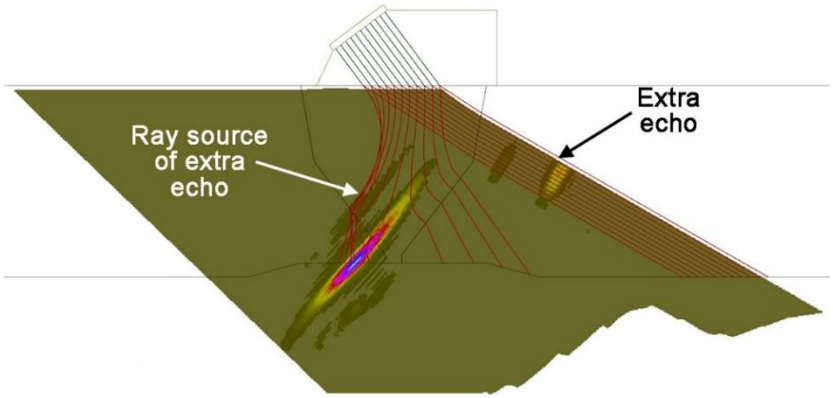

Figure 6.10. Ray path indication showing the source of an extra indication due to beam splitting through the weld.

However, shear-waves are used for inspection through welds (far-side inspections) due to the higher beam deviations and scattering experienced when propagating through welds (Adler et al. 1978; Kupperman and Reimann 1981). However, in the interest of assessing the impact of welds on shear waves, we conducted simulations and experiments using the far-side inspection configuration. Figure 6.11 shows the B-scans (experimental and simulation) for a far-side inspection. In the experimental B-scan (top panel), the specular echo at the flaw-backwall corner can be seen; however, it has a low SNR due to expected higher attenuation of shear waves as they propagate through the weld. In addition, there appears to be an extra echo with an apparent origin close to the weld root region. The simulation B-scan (bottom panel) shows a small specular response from the flaw. The simulation also shows an extra echo at X = −20 mm (−0.8 in.) due to normal beam reflection when the probe is on top of the weld (see Figure 6.10). However, the different probe positions producing the extra echoes in experiment and simulation indicate different sources of origin.

The fact that the simulation B-scan results show the specular echo at a location approximately 10 mm (0.4 in.) away from the expected corner reflection, compared with the experiment results that shows the specular echo at its expected location relative to the flaw, suggest that the anisotropy of the weld in the experiment is not as significant as defined for this simulation. A second observation is the lack of weld root echoes in the simulations. The lack of a significant weld root in the simulation geometry is likely one reason for this. In addition, we defined the simulation to only compute signals from ultrasound interacting with the flaw to limit computational complexity. Further, the lack of a noise model results in SNRs that are significantly different between the simulation and experimental B-scans, as would be expected.

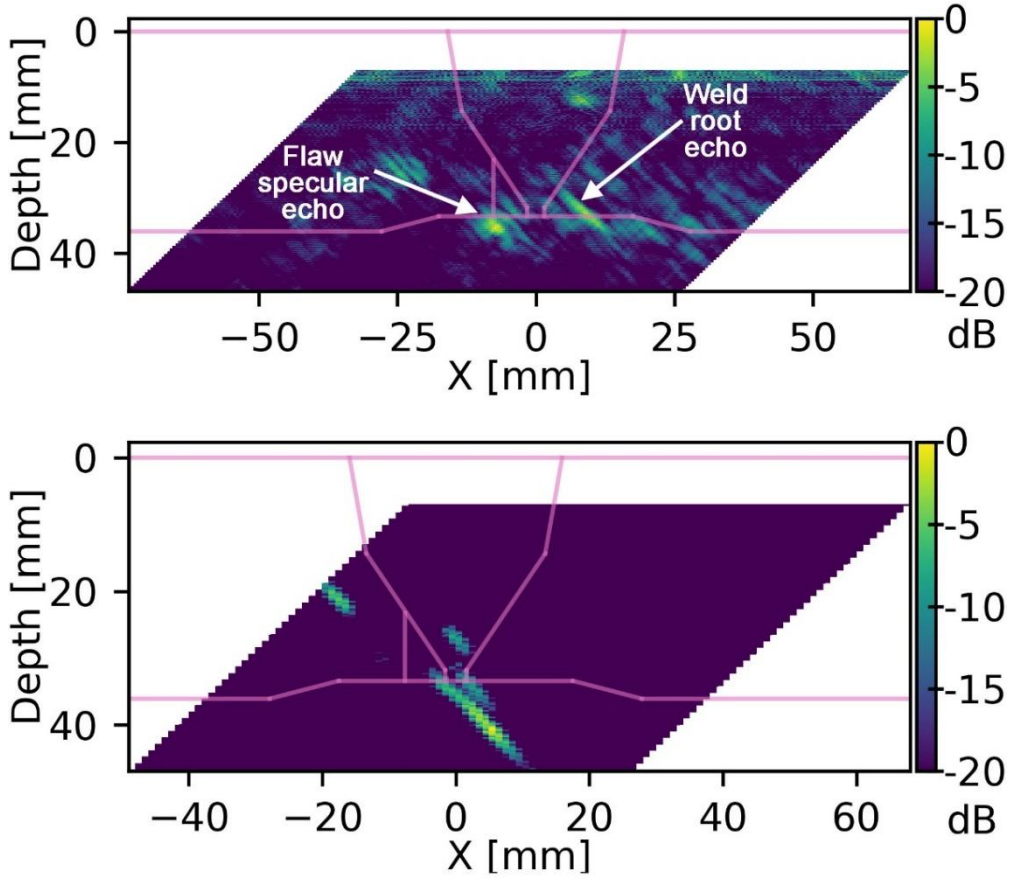

Figure 6.11. B-scan for far side inspection using a 0.5 in. diameter, 2 MHz, 45° shear wave transducer. *Top*: experiment, *bottom*: simulation. The weld profile, and location of the saw-cut flaw are overlaid on the B-scan. The B-scans are normalized to their own maximum signal amplitude. The color maps span amplitudes down to −20 dB from the maximum.

Finally, we compute the calibrated flaw specular response amplitude. Table 6.3 summarizes the results for the experiments and simulations.

Table 6.3. Calibrated Amplitudes for the Saw-Cut Notch Using a Single-Element Shear Wave Probe

	Experiment 95% confidence (dB)	Simulation (dB)
Near side flaw amplitude	[1.3, 7.5]	−15
Near side clutter amplitude	[−17.3, −11.1]	
Near side noise floor	[−31.5, −25.3]	
Far side flaw amplitude	[−19.9, −13.7]	−35.3
Far side clutter amplitude	[−16.1, −9.9]	
Far side noise floor	[−32.9, −26.7]	

Table 6.3 shows that the flaw amplitude response was under-estimated by the simulation for the near-side inspection (flaw response amplitude of −15 dB from a 10 mm [0.4 in.] flaw height at 2 MHz). The reason for this uncharacteristically low signal, given that the beam does not propagate through the weld, is unclear. The flaw response amplitude in the far-side inspection is also much lower in the simulation results; however, this may be due to a greater than necessary weld anisotropy in the simulation parameters. The experimental clutter and noise floor are about 20 dB below the flaw specular response. Thus, in this particular case, simulating these responses would not add significant information to the assessment of model validity and flaw detection capability.

6.4 Summary

The initial analysis of flaw detection within the vicinity of welds, using multiple probes from near- and far-side inspections, indicate that far-side inspections can present significant levels of clutter, depending on the geometric conditions in and near the weld. Experimentally obtained material noise levels were low; however, it is not clear if this was a function of the welds inspected or if the results are generalizable to other specimens.

The flaw specular amplitudes differ significantly between experiments and simulations when using the shear-wave probe and differ (~13 dB) for longitudinal-wave probes (TRL and phased-array). Based on prior experience in validating ray tracing models, these differences are likely not due to a lack of validity of ray theory; instead, they may be due to the way in which simulation software handles complex geometries and/or uncertainties in the material properties. We are currently further investigating the sources of these discrepancies.

Although these results show a large discrepancy between simulation and experiments, we expect that reducing the uncertainty in weld material properties will improve the simulation of flaw specular responses in the vicinity of welds. This will require accurate measurements of dendritic and elastic properties of the weld, in addition to flaw properties such as crack morphology and crack shape (depth profile). As indicated earlier, the use of stochastic methods for validating these complex models is also essential, along with a sensitivity analysis using the validated model also being an essential element of identifying the important parameters for accurate weld simulations.

In addition to flaw response, clutter (noise from ultrasound interaction with geometry) is an important factor in the ability to reliably detect flaws using UT. In the simulations described above, we disabled the calculation of clutter to reduce the computational complexity and run times of the models. The ability of ray models to accurately reproduce clutter in complex geometries with a large number of interfaces in a reasonable amount of time may be a limiting factor in their use in assessing flaw detection capability and reliability. This is especially true if multiple simulation runs are needed for a statistical evaluation of inspection reliability.

7.0 Transducer Variability Analysis in Ultrasound Testing

Ultrasonic simulation results are dependent on the input parameter values used, as shown in the parametric study of input parameters detailed in Dib et al. (2017). Quantifying the variability in input parameters is necessary for quantifying the uncertainty in the simulation results. As a first step toward better bounding of the expected variability of modeling and simulation input parameters, we performed a characterization study on a set of single-element contact transducers. The objective was to assess the performance variability of transducers typical of those used for ISI in the nuclear industry.

All the contact transducers used in this characterization study were nominally 12.7 mm (0.5 in.) diameter with a center frequency of 5 MHz. Given the nominally identical specifications, we expect that the actual center frequency will be close to (typically within 5–10%, based on previous laboratory characterizations of newly procured transducers with identical specifications), if not exactly equal to, the nominal specification. Given the nominal frequency and element size, one would expect a natural focus (near-field to far-field transition) at approximately 136 mm (5.31 in.) in water and near 35 mm (1.38 in.) in stainless steel in the absence of a wedge delay.

Table 7.1 lists the manufacturer, model, and serial numbers of the transducers, and a photo of the transducer set is provided in Figure 7.1. These transducers were acquired by PNNL for a number of projects and applications over the last 25 years, and during this time they have experienced varying use conditions. Their use history is not well documented, similar to probes used in the field where a detailed use history may not be known to the end user. Because the 11 transducers selected were all found to be functional through a basic operational test, they were deemed adequate for use in this preliminary variability study.

Table 7.1 Summary of Transducers Used for Characterization Study

Manufacturer	Model Number	Serial Number
Panametrics	V109	274560
Nortec	ZT-Z-1/2-5	931786
Harisonic	CM0508-R	00B014
Harisonic	CM0508-R	00B015
Harisonic	CM0508-R	00B016
Harisonic	CM0508-R	00B021
Harisonic	CM0508-R	00B023
Sonic	CBA 5-2	09078T
Sigma	SCMB	1127-94001
Sigma	SCMB	1127-94002
Sigma	SWTM-1/2-5	4910-01002

Figure 7.1. Transducers used in characterization study.

The transducer characterization focused on assessing performance in two main areas. The first was on determining the frequency response of the transducers using a contact measurement. This performance characteristic was selected because it is a simple measurement that can be easily replicated by field personnel and provides a quantitative metric for this analysis. The second focus area assessed the effective radius of the transducers using an immersion sound field measurement on the central axis of the transducer. This was selected because of its impact on performance (and simulation results). The active area of the piezoelectric element or effective diameter has considerable effect on the near field length of the sound field. A summary of both characterization activities is provided in the following subsections and a more complete description and discussion of these activities is provided in Appendix A.

Assessing the performance characteristics of a transducer can be performed using a variety of methods. Most modern ultrasonic data acquisition systems feature fast Fourier transform (FFT) processing tools allowing the analyst to compute the frequency response of a transducer with actual inspection data. Although this approach gives some indication of the frequency response of a transducer, it is not the accepted approach for measuring the frequency response because the acquired signal consists of a convolution of characteristics from the probe, cabling, pulser/receiver, and the test part. More advanced methods allow for the convolution of these signals to be separated for determining the true impulse response of the transducer. The *Standard Guide for Evaluating Characteristics of Ultrasonic Search Units* (ASTM E1065-14 2014) provides a rigorous approach for assessing the frequency response of a transducer and is the approach used to characterize the 11 transducers in this study. Other, more rigorous and academic approaches for accurately characterizing a transducer are available and widely accepted. For example, the method presented in Schmerr Jr. and Song (2007) is one of the leading approaches applied in NDE research. This method allows for the characterization of the sub-components of the measurement system (cabling, inspection material, transducer, etc.) and describes models for removing the transfer function of these sub-components so that the actual characteristics of the transducer can be more effectively isolated and quantified.

7.1 Frequency Response

The frequency response measurements of the 11 transducers in this study were performed in adherence to the ASTM E1065-14 standard (ASTM E1065-14 2014). The time-domain response of each transducer was acquired as shown in Figures 7.2 and 7.3. This setup employed a pulse-echo mode for measuring the response through an aluminum block that was 86 mm (3.4 in.) thick. The aluminum block was submerged in water such that the wear face of the transducer was slightly submerged for consistent coupling. A 2.0 kg (4.5 lb.) weight was placed on the transducer to provide consistent coupling pressure. For the two transducers with the micro-dot connector on the top of the housing, a load cell was used instead of the weight and 2.0 kg (4.5 lb.) of coupling force was applied manually. The time-domain response (A-scan) was recorded using an oscilloscope, and post-processing was performed in MATLAB. Further information on the setup configuration, data acquisition and analysis specifics, and transducer results are provided in Appendix A.

Examples of representative and atypical results are shown in Figures 7.4 and 7.5, respectively. The atypical results were generally significantly outside the nominal specifications.

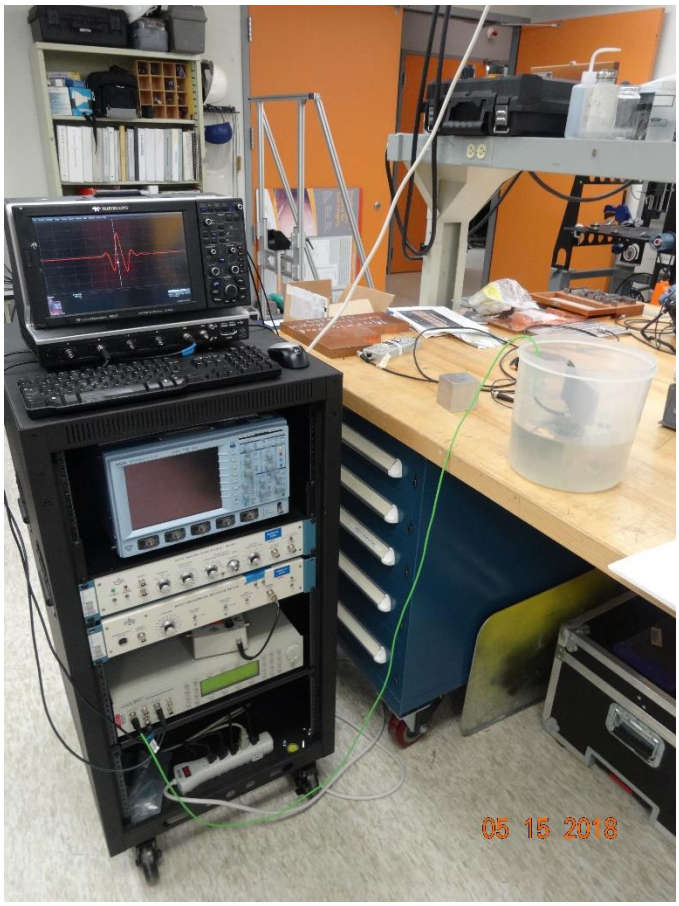

Figure 7.2. Setup for frequency response evaluation of contact transducers.

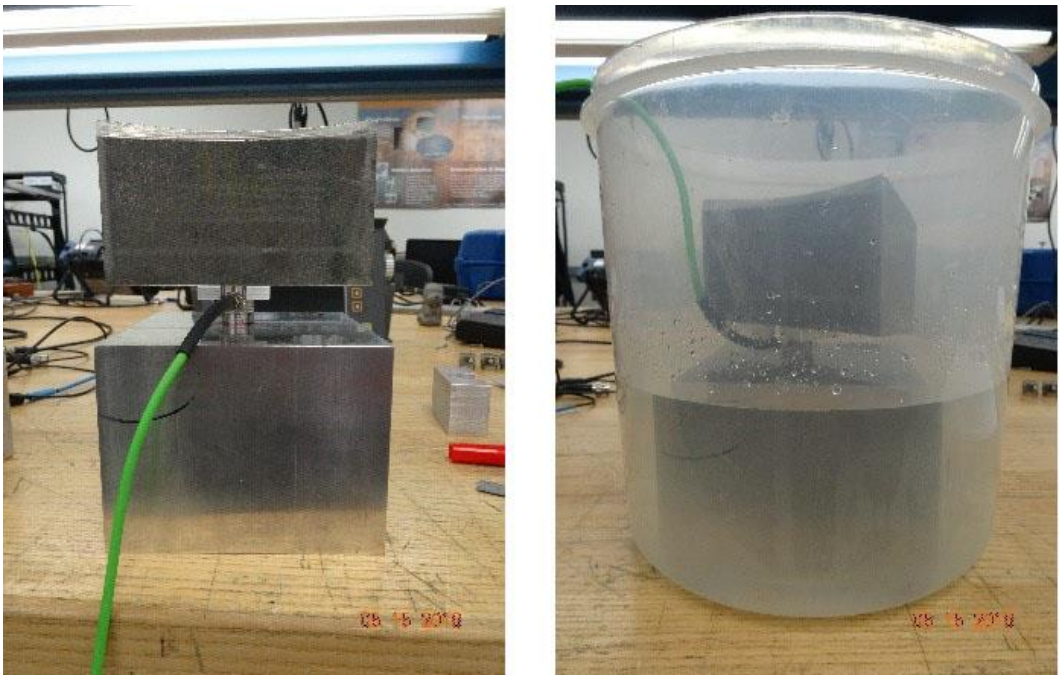

Figure 7.3. Contact configuration using 4.5 lb. weight for consistent coupling.

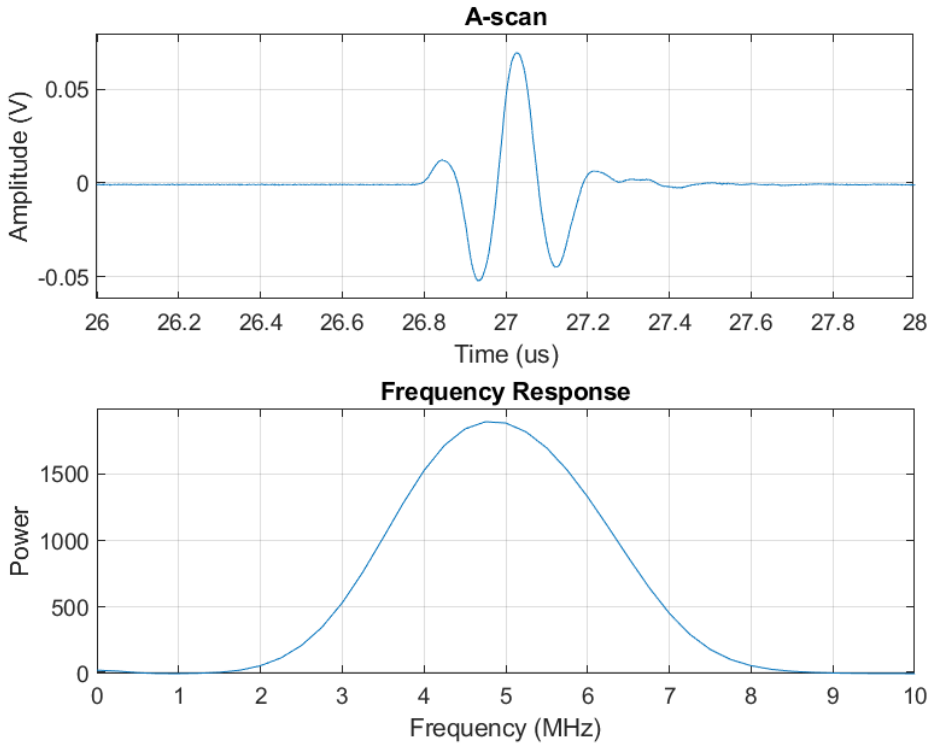

Figure 7.4. Representative transducer time-domain (*top*) and frequency-domain (*bottom*) results.

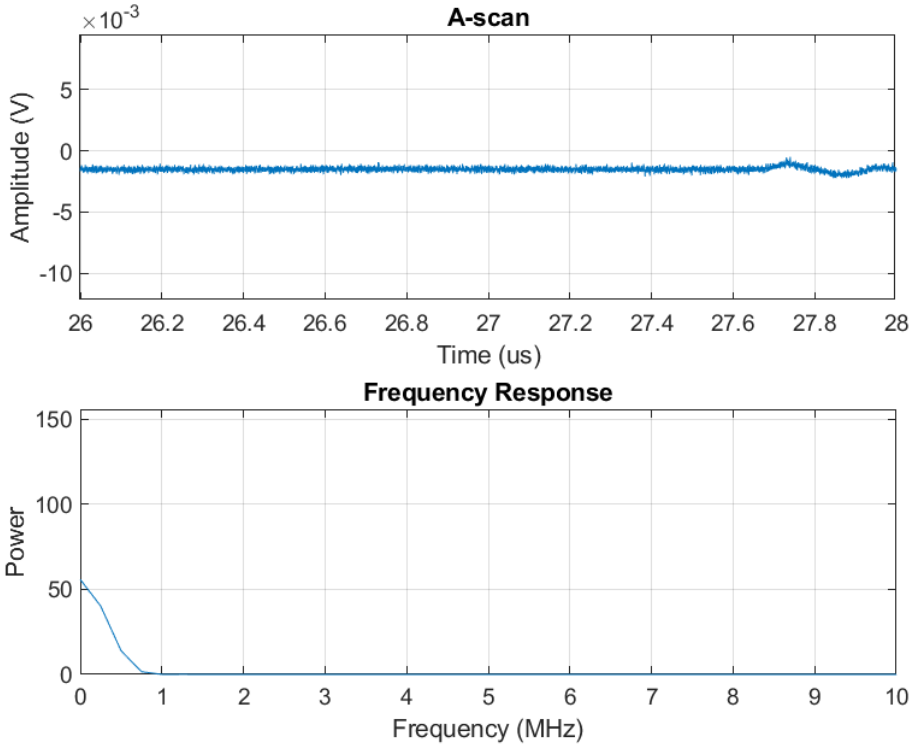

Figure 7.5. Example of atypical transducer results in time-domain (*top*) and frequency-domain (*bottom*).

A summary of the results from the frequency response characterization is provided in Table 7.2. Note that transducers were randomized and given an alias. The results from Transducer #1 are clearly outside the bounds of expected performance, indicating that this transducer was not functioning properly. As a result, this transducer was not included as part of the set used for the remaining analysis. Statistics from the remaining set of ten transducers are provided in Table 7.2 and consist of average, minimum, and maximum values for the peak operating frequencies, center frequencies, 6 dB low- and 6 dB high-frequency points, and the 6 dB bandwidth [BW]) of the probes). The standard deviation is also given for each of these parameters.

Table 7.2. Summary of Frequency Response Results

Transducer Alias	F-peak, MHz	F-center, MHz	F-Low, MHz	F-High, MHz	BW, MHz	−6 dB Δ Frequency, MHz	−6 dB BW, %
1	0.75	0.76	0.75	0.78	0.03	0.03	3.7
2	6.75	6.71	5.86	7.56	1.70	1.70	25
3	3.50	3.49	2.58	4.39	1.81	1.81	52
4	4.75	4.63	3.43	5.82	2.39	2.39	52
5	4.75	4.71	3.45	5.97	2.51	2.51	53
6	5.00	4.94	3.67	6.20	2.52	2.52	51
7	5.00	5.05	3.68	6.41	2.73	2.73	54
8	5.25	5.21	3.78	6.64	2.86	2.86	55
9	5.00	4.77	3.31	6.22	2.92	2.92	61
10	4.75	4.92	3.44	6.41	2.98	2.98	60
11	4.50	4.35	2.77	5.92	3.15	3.15	72

	F-peak	F-Center	F-Low	F-High	Δ Frequency, MHz	6 dB BW, %
Minimum	3.50	3.49	2.58	4.39	1.70	25
Average	4.92	4.88	3.60	6.15	2.56	54
Maximum	6.75	6.71	5.86	7.56	3.15	72
Standard Deviation	0.759	0.762	0.839	0.752	0.457	11.3

7.2 Beam Profile Mapping

Central-axis beam profile mapping was performed on each transducer to determine the near-field/far-field transition distance and the effective active area of each piezoelectric crystal. Each of the transducers has a nominal 12.7 mm (0.5 in.) diameter, which was used to compute the theoretical distance *N* to the transitional zone between the near field and the far field. A basic estimation of *N* is given in (Krautkramer and Krautkramer 1990) as

$$N = \frac{D^2 F}{4C}$$

where *D* is the element diameter, *F* is the center frequency of the transducer, and *C* is the sound velocity in the medium. Assuming the entire element area is active and the transducer operates close to the nominal center frequency, 5 MHz, *N* is expected to end 136 mm (5.31 in.) from the wear face along the central axis of the transducer. This is expected to be an over-estimate because the entire diameter of the element is likely not active. The edges of the element are constrained by the housing of the transducer, reducing the active area of the element and consequently shortening the near field to some degree. Additionally, damage to the element or probe face can contribute toward non-linearity in the near field, leading to unpredictable sound field conditions for conventional, single-element probes.

To measure *N*, single-axis sound field mapping (beam profile mapping) was performed. This was done using two different methods. First, the pulse-echo response from a spherical reflector (stainless steel ball bearing) in water was measured at multiple distances from the transducer along the central axis of the probe. The second approach used a pinducer as a receiver to directly measure the sound field. The resulting amplitude variation was used to identify the near-field distance for each transducer.

Because the results from the spherical reflector showed significant variation of probe characteristics from the ideal case, CIVA was used to simulate the sound field in water for the ideal case and the effects of probe misalignment (axis along which the sound field is measured is not perfectly orthogonal to the transducer face) on the near-field transition measurement. The simulations indicated that even small misalignments (on the order of 0.2^{o} or so from normal) could result in large variations in the measured near-field distance.

Based on the CIVA results, the pinducer-based measurements were used to directly detect the sound field. The pinducer-based measurements were performed by a different project team member to independently verify the results of the spherical reflector method. Details of the methods for these assessments are described in ASTM E1065, and in Appendix A. The theoretical bases for similar methods of transducer characterization are also included in Schmerr Jr. and Song (2007).

7.2.1 Spherical Reflector Measurements

For the reflector method, a 3-axis translation stage was used to scan the spherical reflector along the axis of transducer from 155 mm to 2 mm (6.1 in. to 0.08 in.) from the face. A-scans were acquired every 1 mm (0.04 in.) along the scan path using an oscilloscope. Figure 7.6 shows the overall system used to perform this evaluation, including the motion controller, pulser/receiver equipment, and the 3-axis translation stage. Figure 7.7 shows the instrumentation for pulsing and receiving, a bandpass filter, and an oscilloscope for saving the RF waveforms. Figure 7.8 shows a view inside the immersion tank used for this activity. The spherical reflector was attached to the translation stage, for scanning in the Z-direction. According to the ASTM standard, the ball target should have a diameter at least 10 times the wavelength. The wavelength of sound at 5 MHz in water is about 0.3 mm, and the ball was 5 mm in diameter, so this condition was easily satisfied. The top surface of the spherical reflector was positioned 24 mm (0.94 in.) from the top surface of the plate. This separation was critical to identifying the spherical reflector response from the plate response. Appendix A describes the measurement procedure in detail.

A waveform was stored at each scan position. Each waveform was post-processed using MATLAB, and the peak response of the spherical reflector was recorded. The peak response at each position was then plotted as a function of distance from the transducer as shown in Figure 7.9.

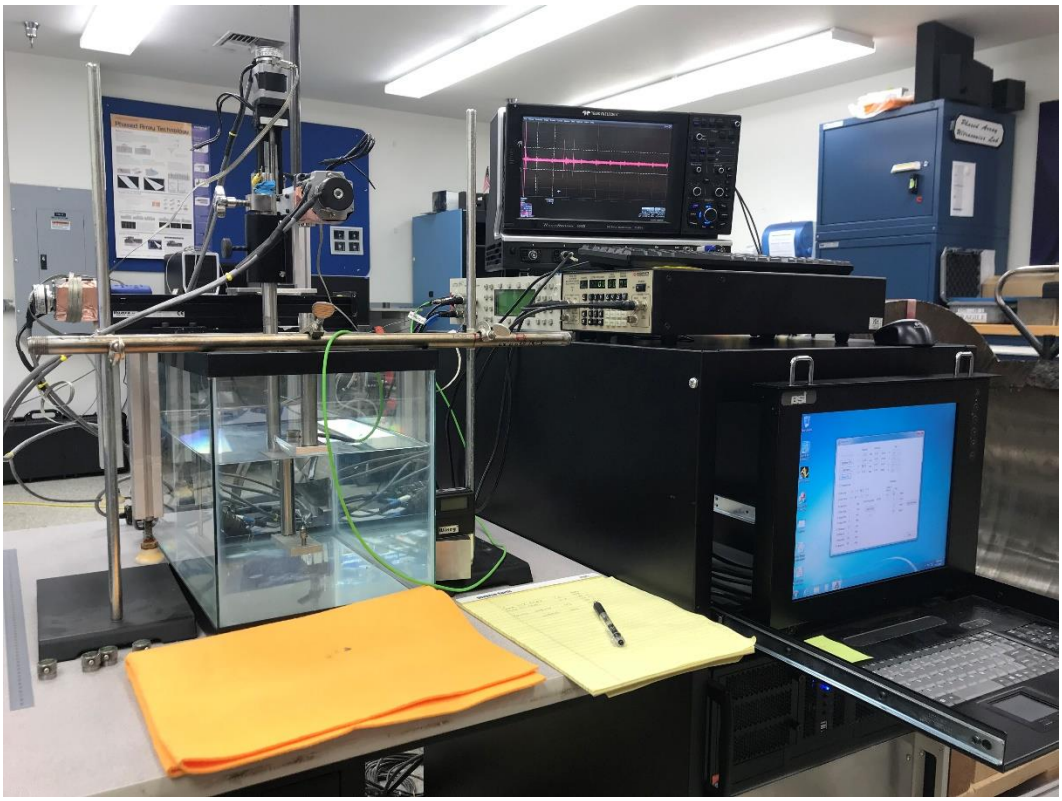

Figure 7.6. Setup for measuring beam profile along transducer axis.

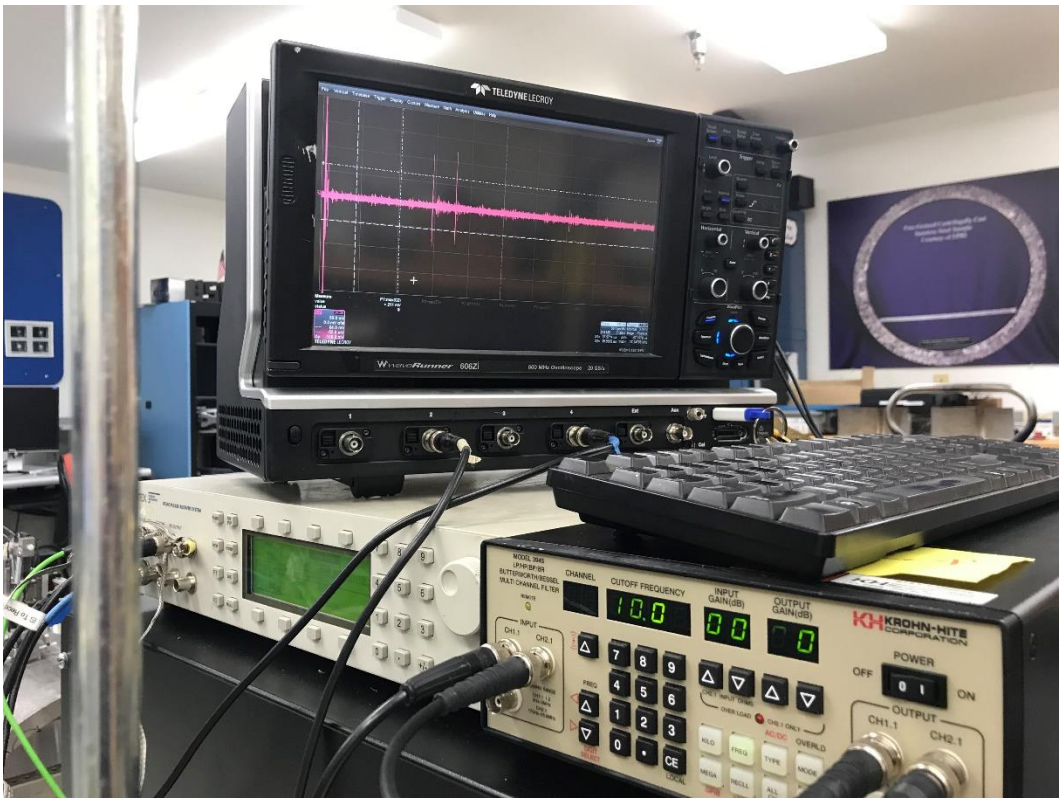

Figure 7.7. Instrumentation for beam profile measurements.

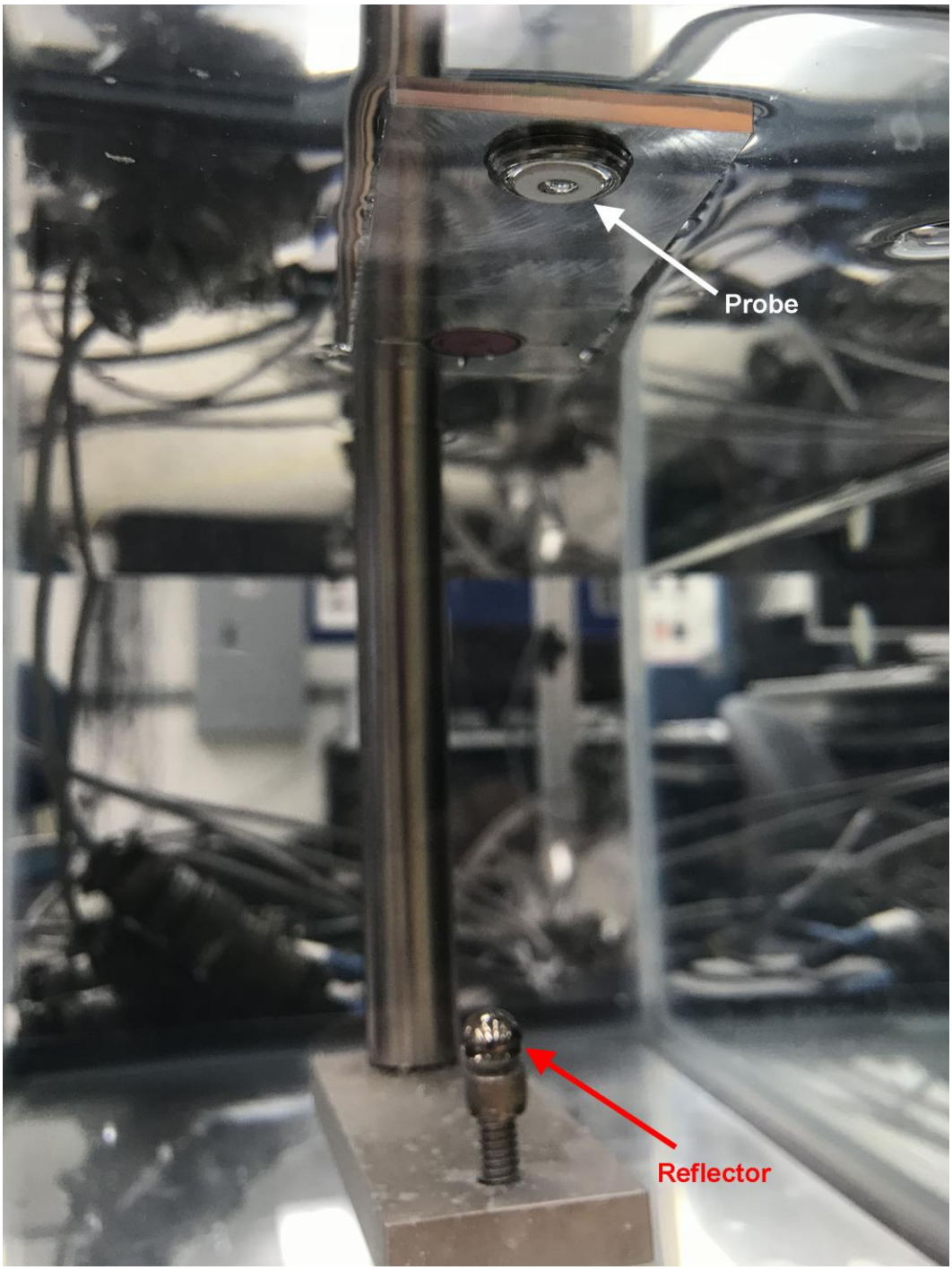

Figure 7.8. Immersion tank configuration and spherical reflector for beam profile measurements.

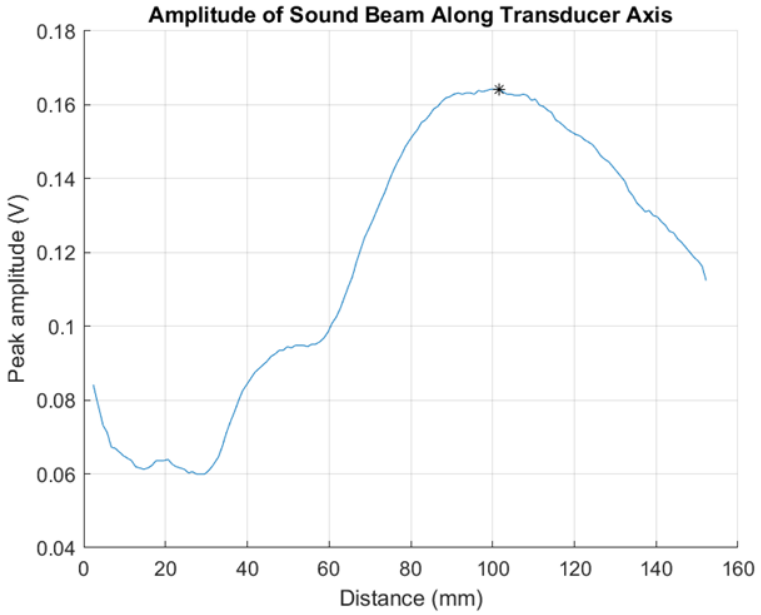

Figure 7.9. Example of the resulting sound beam profile as a function of distance from the transducer.

7.2.2 Pinducer Measurements

7.2.2.1 Beam Profile

For the pinducer method, a similar setup to that described above with the ball reflector was used to translate the pinducer. Figure 7.10 shows the scanning apparatus with a mounted transducer and pinducer and Figure 7.11 shows a close-up view of the submerged pinducer directed toward the face of the transducer. UltraVision and a DYNARAY PA-UT system were used to collect and store the encoded data generated by the motor controller and pinducer. An Agilent 33220A function generator was used to drive the transducer using a three-cycle tone-burst at the previously measured center frequency of the transducer. Figure 7.12 shows an example of the raw data collected in UltraVision on Transducer #7. The red cursors were placed at approximately the transition position, or *N*. Data were exported to MATLAB for further analysis. The data acquisition and analysis procedure is described in detail in Appendix A.

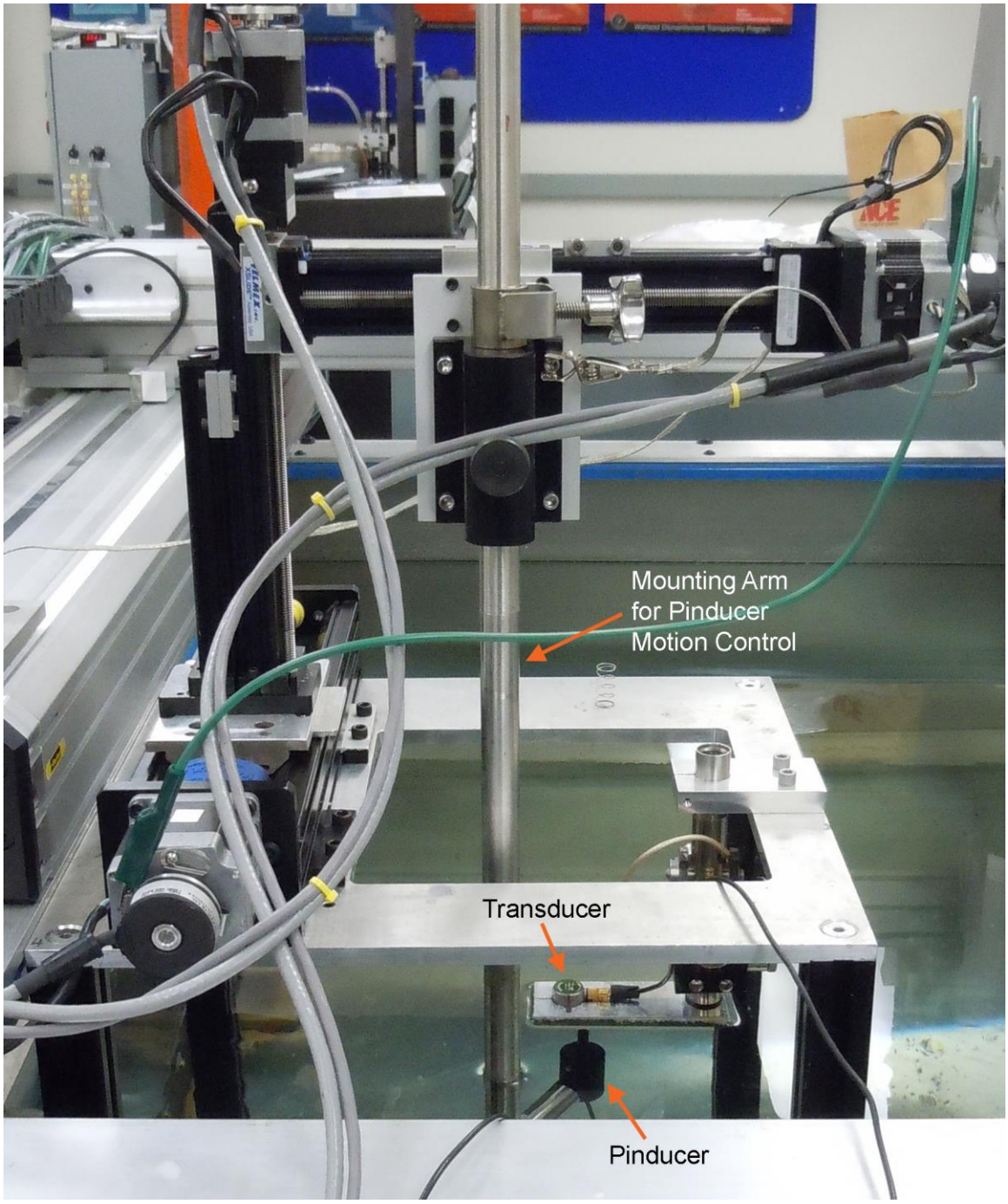

Figure 7.10 The scanning apparatus with a mounted transducer and pinducer.

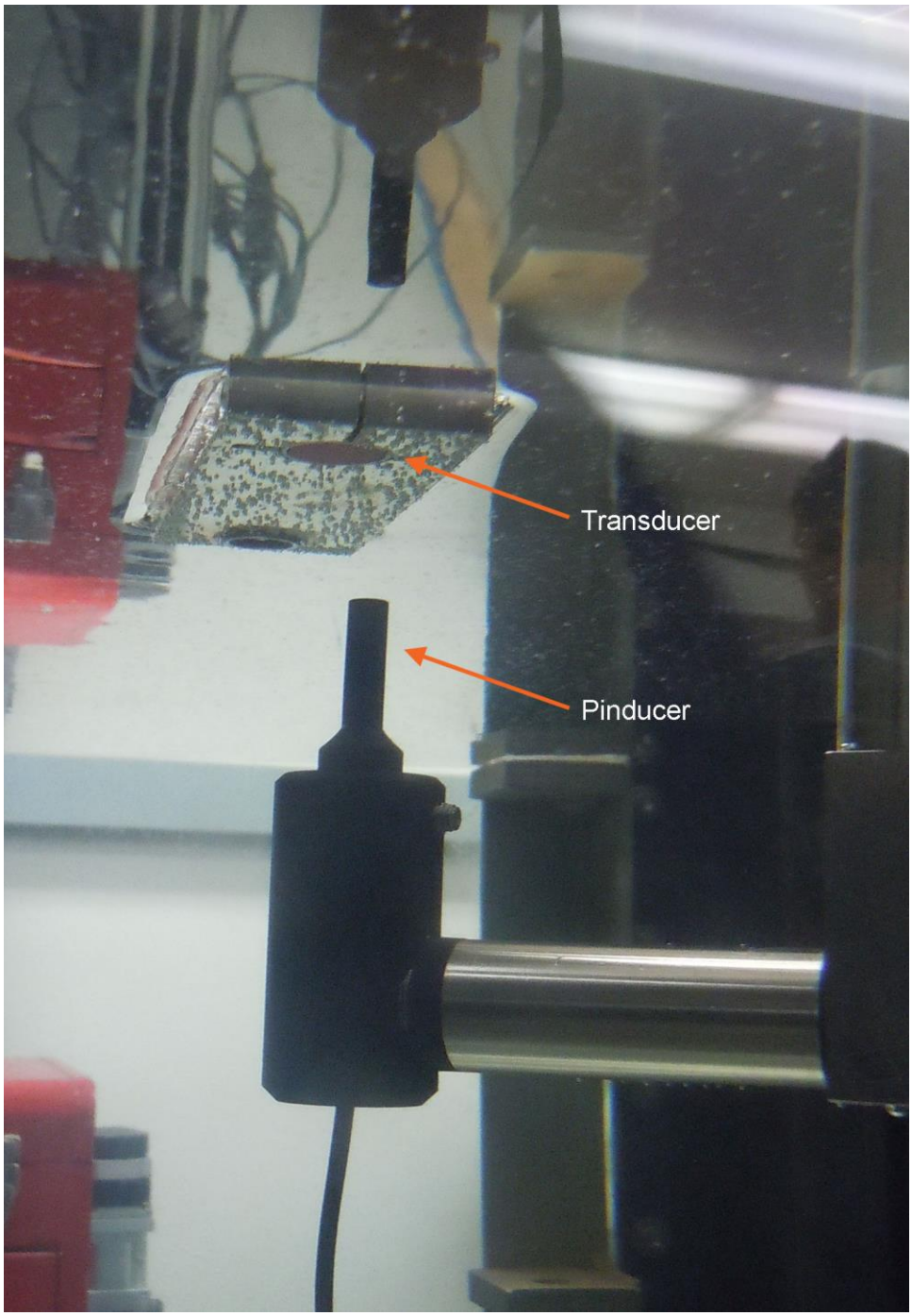

Figure 7.11 A view of the submerged pinducer and transducer.

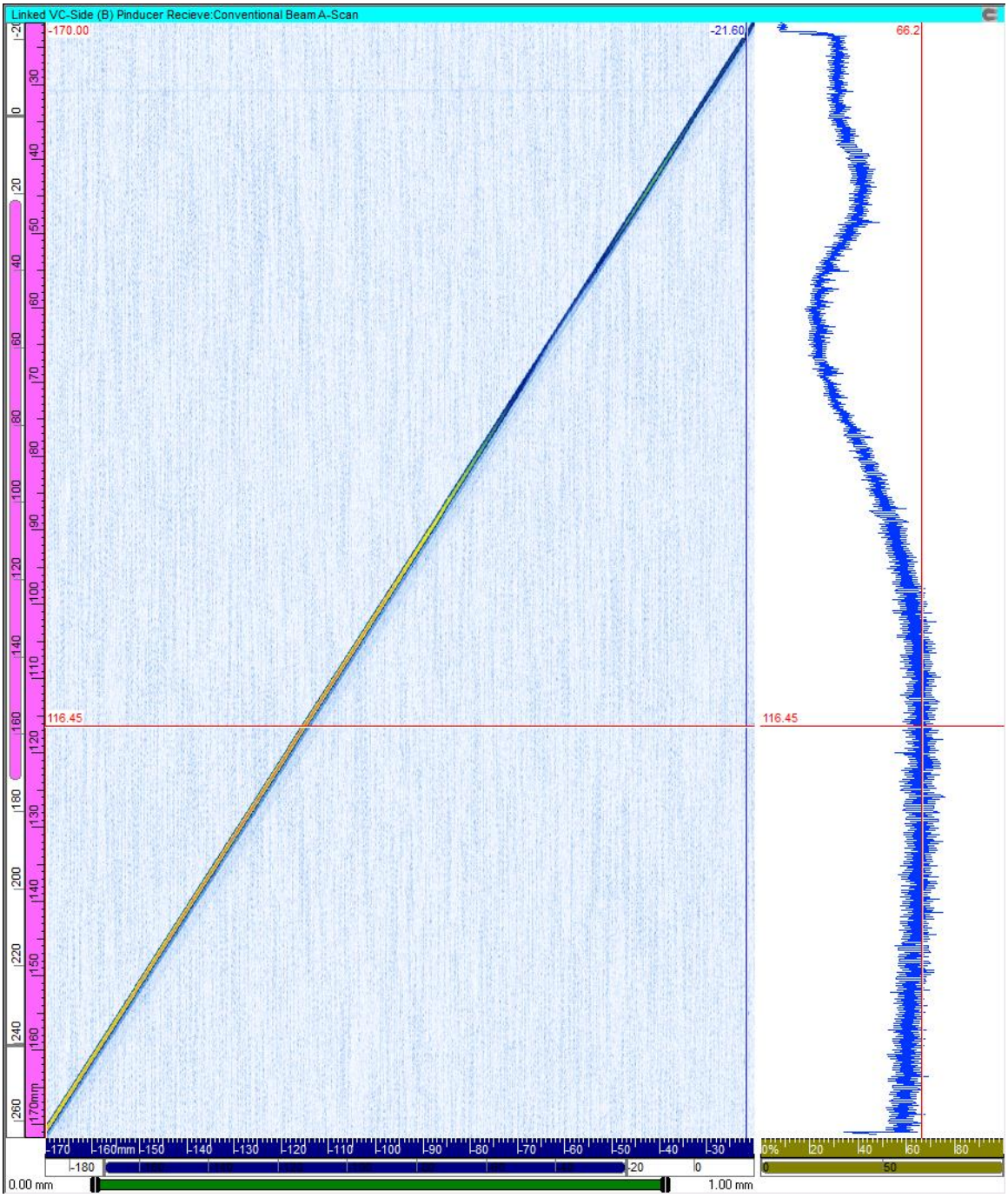

Figure 7.12 UltraVision line profile data from Transducer #7 showing the raw line scan data (*left*) and the data profile (*right*). The horizontal red line indicates the approximate position of the signal maximum.

7.2.2.2 Transducer Face Maps

The probe face was scanned on seven of the probes: those that showed the largest variation between values of *N* obtained from the spherical reflector data and the pinducer line scan data. This included Probes 2, 4, 5, 7, 8, and 11. For Probe 3, the calculated effective diameter obtained from both measurement sets was nearly as large as the nominal diameter, potentially suggesting a nearly ideal emitting surface. Therefore, the face of this probe was scanned as well. Face scans were done by placing the pinducer approximately 1–2 mm (0.04–0.08 in.) away from the probe face and collecting a 2D scan in the XY plane. Figure 7.13 shows an example of the probe face scan of Transducer #3. The scan shows a circular and relatively uniform beam intensity at the face of the transducer. This type of behavior was not typical of the transducers; for example, the scan of Transducer #5 (see Figure 7.14) resulted in significant sound field heterogeneity close to the face of the probe. Upon close visual examination of the probe face, this heterogeneity appeared to be related to slight damage to the surface of the transducer face. Figure 7.15is a photograph of the probe face showing the area of damage. Other transducers did not show any visual damage but also had inhomogeneous sound patterns. Appendix A shows all of the transducer face maps that were collected.

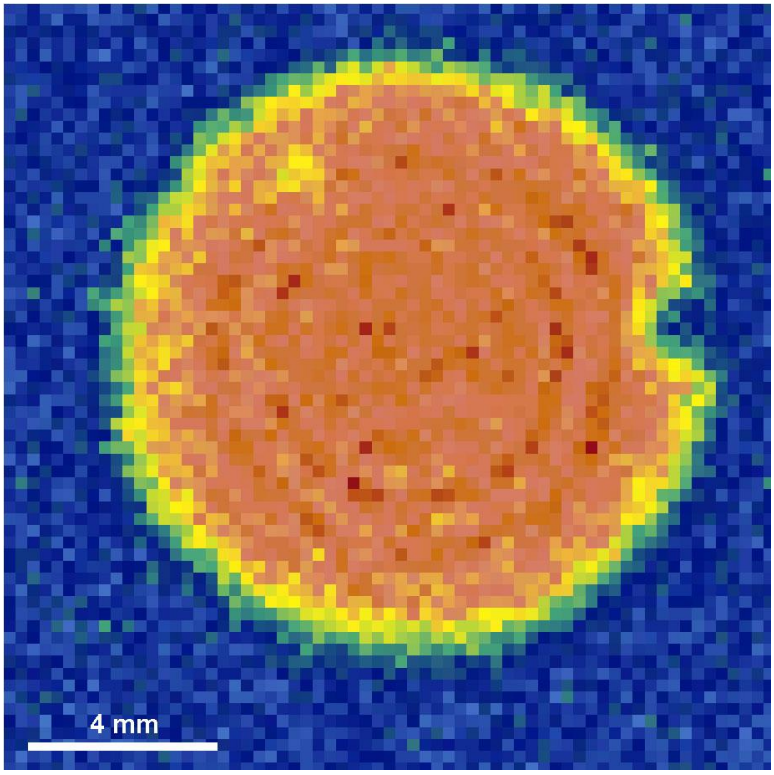

Figure 7.13 Probe face scan of Transducer #3. The soft gain was adjusted so that the peak signal was 100% of full-screen-height.

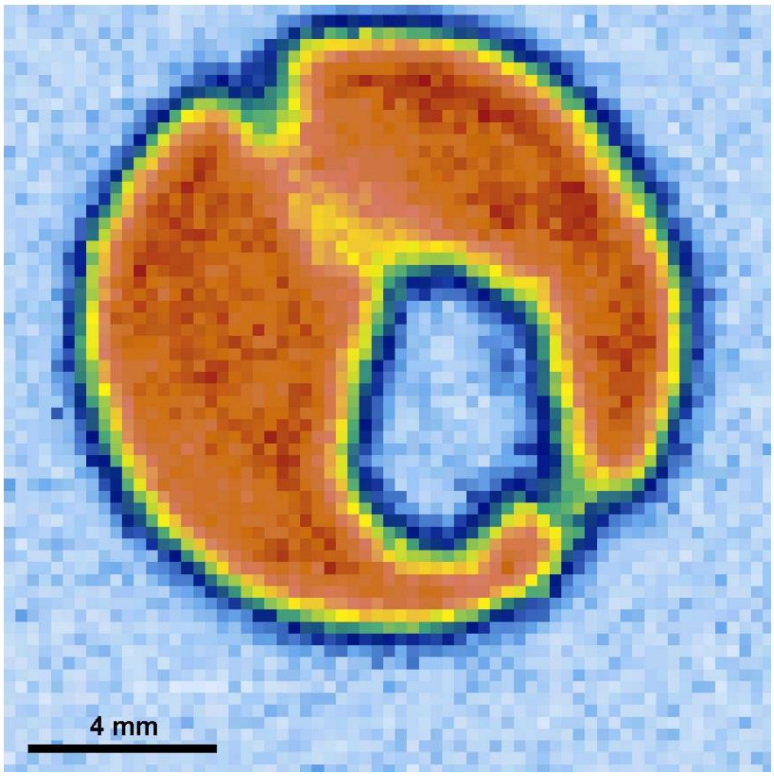

Figure 7.14 Probe face scan of Transducer #5. The soft gain was adjusted so that the peak signal was 100% of full-screen-height.

Figure 7.15 Photograph of the face of Transducer #10

7.2.2.3 CIVA Beam Simulations

Simple 2D beam simulations were generated in CIVA using a circular probe and water as the medium. A 50 mm × 300 mm (2.0 in. × 11.8 in.) sensitivity zone was defined in the XZ plane with 0.5 mm (0.02 in.) isotropic resolution. For the nominal transducer, the diameter was set to 12.7 mm (0.5 in.), the frequency to 5 MHz, and the −6 dB bandwidth to 55%. Figure 7.16 (left) shows the XZ profile for the nominal case; the horizontal line indicates the position of the maximum signal *N*. For specific probe models, the measured center frequencies and bandwidths were used. A variety of different probe diameters were simulated, including the nominal diameter and those obtained from the spherical reflector data, the pinducer data, and the probe face scans. The results provided here use the diameter from the probe face scan as model inputs because this was the only direct measurement of the transducer diameter; that is, this measurement did not depend on a calculation based on the line-scan data. Appendix A.5 shows the beam profile results from each of the simulations. Included on each plot is the nominal case for comparison.

In addition to the nominal probe simulation, a 3D simulation was performed with the probe at a 0.2° tilt. This was done to estimate the effects of slight transducer misalignment on laboratory measurements of *N*. Figure 7.16 (right) shows the results of the simulation in the central XZ plane. The maximum signal position, shown by the horizontal line, is considerably closer to the probe than in the normal incidence case.

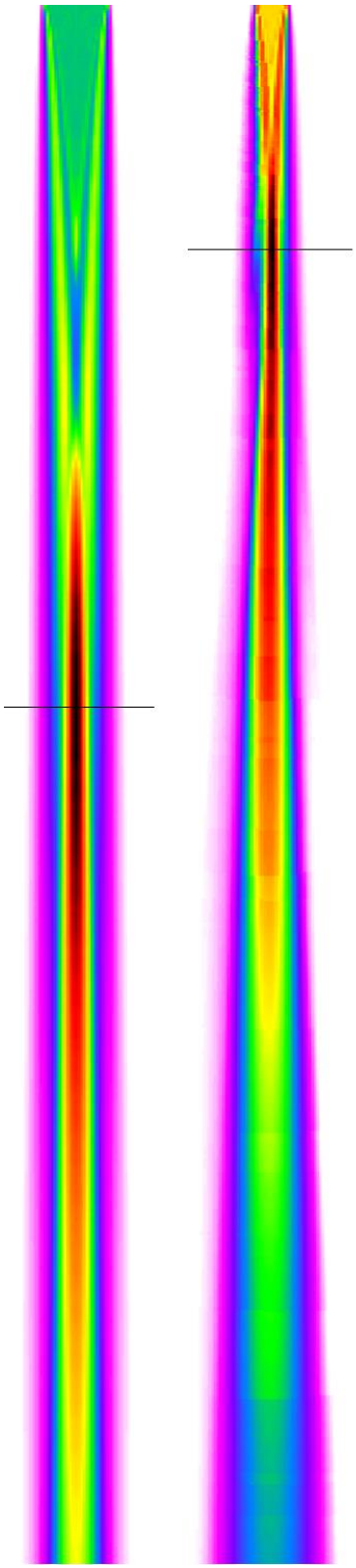

Figure 7.16. XZ Profiles of a simulated nominal transducer. *Left*: normal incidence. *Right*: 0.2° transducer tilt.

To further examine how alignment issues may affect experimental results, the maximum beam position was measured in the simulated nominal case (with 0° incidence) at 0.5 mm (0.02 in.) increments from the beam center. This would imitate off-central-axis measurements. Figure 7.17 shows the results of five measurements from the beam center to 2.0 mm (0.08 in.) off of center. The circles indicate the maximum signal positions, and the line connecting them shows the trend. Results show that as misalignment with the probe center increases, the maximum position also increases while the signal intensity decreases. For comparison to the normal incidence beam, Figure 7.17 also shows the case with the 0.2° tilt. Results suggest that combined subtle misalignment of the transducer angle and pinducer (or spherical reflector) position can result in significant changes in the measured *N* with a continuum of possible results.

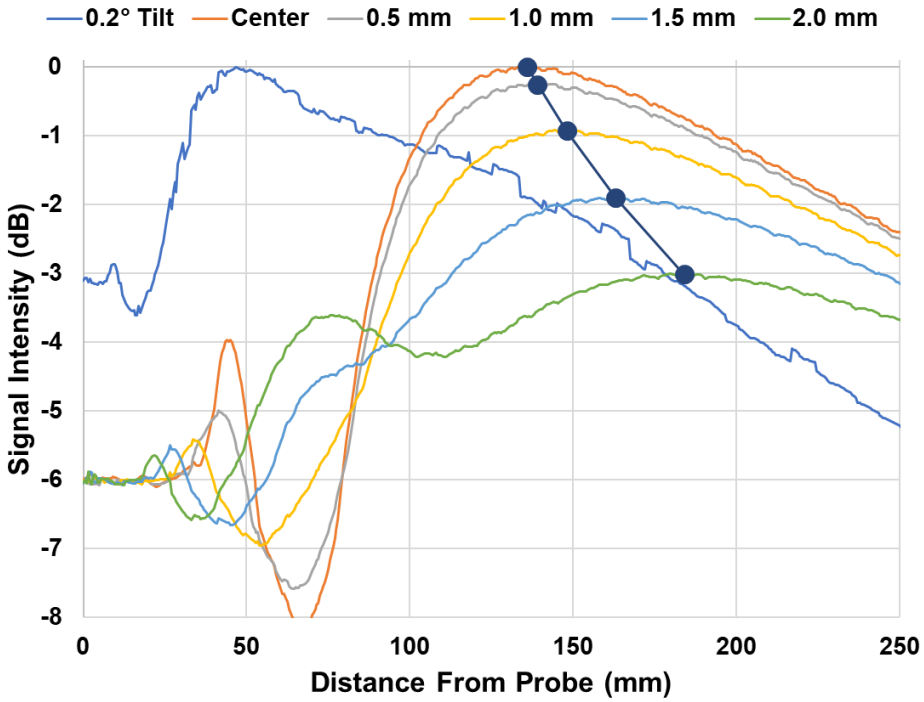

Figure 7.17. Beam profiles of a simulated nominal transducer at different distances from the beam centerline and at a 0.2° tilt.

Results

A summary of the results across all transducers is provided in Table 7.3 and Table 7.4, which show the calculated and measured values of the effective transducer diameters and near-field transition lengths *N*, respectively. Figures 7.18 and 7.19 show box-and-whisker plots[1] of the data, illustrating the range of values obtained from the different methods. Both plots show that the range of results from the spherical reflector is much greater than the range obtained from the pinducer. This is most likely due to the added scrutiny and attention paid to the alignment process with the pinducer. Further, note that the measured values of *N* made with the ball-target are considerably lower than those made with the pinducer. This is likely due to transducer

[1] A box-and-whisker plot, or box plot, summarizes the set of data by displaying the median (the line within the box), the first and third quartiles (the lower and upper extents of the box), and the minimum and maximum values (the extent of the lines, or “whiskers”). Any outliers are shown as individual data points. In the plots shown here, the mean is indicated by an ‘x’.

alignment issues. As discussed above, the CIVA simulations suggest that slight angular misalignment of the transducer may significantly reduce the measured value of *N*. Additionally, the CIVA results for *N*, which used the beam map diameters as an input, closely match those calculated from the beam maps, as expected. Recall that Transducer #1 was excluded from these results due to its poor performance in the frequency response evaluation. Plots showing the beam profiles from each transducer are provided in Appendix A.

Table 7.3. Transducer Effective Diameters

Transducer Alias	Calculated Effective Diameter, Ball Reflector, mm (in.)	Calculated Effective Diameter, Pinducer, mm (in.)	Measured Effective Diameter, Face Beam Map, mm (in.)
2	7.8 (0.31)	10.3 (0.41)	10.5 (0.41)
3	12.6 (0.49)	12.4 (0.49)	11.0 (0.43)
4	9.1 (0.36)	11.9 (0.47)	10.5 (0.41)
5	4.6 (0.18)	12.2 (0.48)	11.4 (0.45)
6	10.2 (0.40)	11.6 (0.45)	NM
7	6.2 (0.25)	11.7 (0.46)	11.4 (0.45)
8	7.9 (0.31)	11.1 (0.44)	11.4 (0.45)
9	11.2 (0.44)	12.2 (0.48)	NM
10	10.3 (0.41)	11.7 (0.46)	NM
11	7.4 (0.29)	13.1 (0.52)	9.6 (0.38)

Note: Transducer #1 excluded due to poor performance in frequency response evaluations.
NM: Not measured

Table 7.4. Transducer Transition Lengths

Transducer Alias	Measured Transition, Ball Reflector, mm (in.)	Measured Transition, Pinducer, mm (in.)	Calculated Transition, Beam Map, mm (in.)	Transition, CIVA, mm (in.)
2	68.2 (2.69)	119.8 (4.72)	124.7 (4.91)	120 (4.7)
3	87.4 (3.44)	85.6 (3.37)	71.2 (2.80)	73 (2.9)
4	64.1 (2.52)	110.2 (4.34)	86.1 (3.39)	86 (3.4)
5	16.7 (0.66)	118.7 (4.67)	103.2 (4.06)	104 (4.1)
6	86.2 (3.39)	111.2 (4.38)	N/A	N/A
7	33.0 (1.30)	116.4 (4.58)	110.6 (4.36)	111 (4.4)
8	54.5 (2.14)	107.5 (4.23)	114.1 (4.49)	114 (4.5)
9	101.5 (4.00)	118.9 (4.68)	N/A	N/A
10	88.4 (3.48)	114.3 (4.50)	N/A	N/A
11	40.3 (1.59)	126.8 (4.99)	67.6 (2.66)	67 (2.6)

Note: Transducer #1 excluded due to poor performance in frequency response evaluations.
N/A: Not applicable. The specific measurement was either not performed in the laboratory or simulated using CIVA.

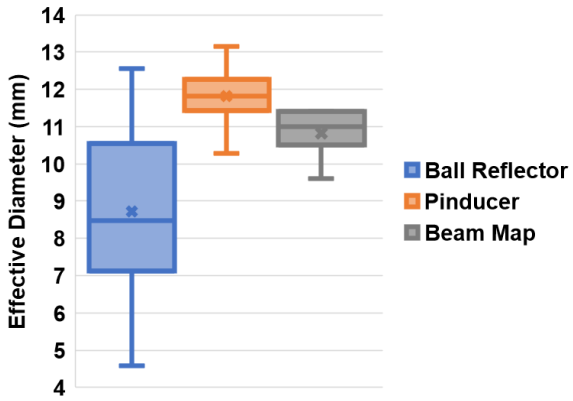

Figure 7.18. Box plot showing the range of measured and calculated probe diameters.

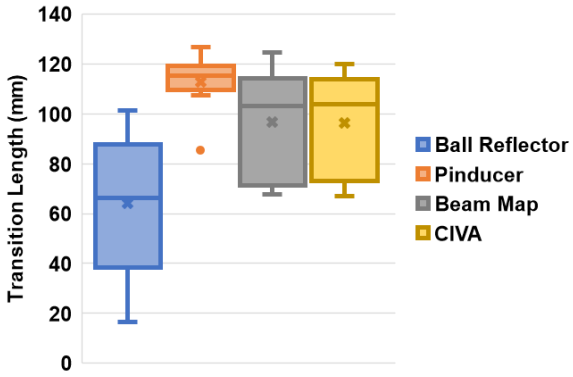

Figure 7.19. Box plot showing the range of measured and calculated near-field transition lengths *N*.

7.3 Discussion

The 11 transducers used in this limited study exhibited variation and some deviation from the nominal specifications. Transducer #1 exhibited atypical responses in the time-domain during the frequency response evaluation and consequently was removed from the study. The remaining ten transducers had an average (± standard deviation) peak frequency of 4.92±0.80 MHz and a center frequency of 4.88±0.80 MHz, slightly lower than the expected 5 MHz center frequency. The average −6 dB bandwidth of the set was 54±12%. A limited comparison between probes with the same model number showed that for one manufacturer the peak and center frequencies were within 500 kHz and bandwidths of the probes were within 10%. Another manufacturer's probes had peak and center frequencies varying by more than 1 MHz and bandwidths within 10% of each other. It should be noted that manufacturing tolerances may contribute to this variation as well as effects from prior use (over excitation, physical damage from dropping, etc.).

The beam profile mapping activity was used to measure the peak position, or near-field length *N*, of the sound field along the central axis of the transducer, and then the effective active diameter of the transducer was calculated. The theoretical *N* of a 5 MHz, ½-inch diameter probe in water is 136 mm (5.35 in.) The average *N* of the transducer evaluated with the ball reflector was 64±28 mm (2.5±1.1 in.), resulting in an average effective diameter of 8.7±2.4 mm (0.34±0.09 in.). However, with stricter attention to alignment, the average *N* measured with the pinducer was 113±11 mm (4.4±0.4 in.), resulting in an average effective diameter of 11.8±0.8 mm (0.46±0.03 in.). Based on the scans of the probe faces, the average effective diameter was measured to be 10.8±0.7 mm (0.43±0.03 in.). This is slightly smaller than, but not significantly different from, the average diameter calculated from the near-field distance measurement using the pinducer. Because both techniques of determining the effective diameter rely on approximations, it is impossible to say which result is "correct." Even so, it was expected that the near-field-to-far-field transition and effective diameter would be shorter than the theoretical values due to the physical constraints on boundaries of the piezoelectric element.

CIVA simulations of the beam profile used the probe-specific measured values of the spot size from the beam mapping along with the measured probe frequency and bandwidth. The resulting near-field transition lengths *N* are shown in Table 7.4 and agree strongly with the calculated lengths based on the beam map data, as expected. Overall, the CIVA results agree well with the transition lengths measured with the pinducer, except for Transducer #11. The beam map of this transducer reveals what appears to be an oblong active area with regions around the edges that are emitting sound but not as strongly as the center region. Such heterogeneities would cause the calculation of the transducer diameter to be too low when the 3 dB drop method is used as per the ASTM standard. When a −6 dB threshold is used, the measured effective diameter increases from 9.6 mm to 12.1 mm (0.38 in. to 0.48 in.), which causes the calculated near-field transition to change from 68 mm to 107 mm (2.7 in. to 4.2 in.). This agrees more closely with the transition length measured with the pinducer of 127 mm (5.0 in.). Therefore, in some cases the −3 dB threshold is likely too conservative for measuring the transducer effective diameters. Indeed, carefully mapping the near-field transition length is a better indicator of true probe performance than mapping the beam at the probe face, because the former gives a direct measure of the actual transition length without relying on approximations or calculations. However, in the absence of time or ability to meticulously align the probe and pinducer, collecting a beam face map is a good alternative.

This work is an example of the importance of incorporating modeling and simulation for understanding and informing experimental results. In this case, the initial results from the spherical reflector method showed significant variation from the transducers' expected performance. Modeling was then used to explore scenarios that could explain the variance. In particular, alignment issues were explored in CIVA much more efficiently than could have been done in the laboratory. Once the hypothesis that probe alignment was a critical parameter was reached, additional empirical work was performed to confirm whether the hypothesis was correct. In this case, the work entailed extremely careful attention to transducer and pinducer alignment, with the adoption of a rigorous, iterative process. After the additional data were collected, experimental results were once again compared to simulations to verify that theoretical expectations were met. Without the benefit of the simulations, the initial spherical reflector results may have been assumed to be correct and no further verification would have been performed. Therefore, this work illustrates nearly ideal synergy between experiment and simulation, with each being informed by, and then in turn informing, the other to obtain results that can be trusted and verified.

In evaluating this set of ultrasonic transducers, some discrepancy in near-field lengths was shown. There are many factors that could potentially contribute to this variability, including the type of piezoelectric element used (i.e., piezocomposite, ceramic, etc.), variability in backing materials and the bonding to the active element, differences in potting and grounding techniques, variations in wear plate type and quality of adhesion to the active elements, and others. However, the objective of this work was to assess the performance specification variability in a small sampling of single-element transducers, not to delve into the sources of variability. This topic has been described elsewhere in the scientific literature (Silk 1984; Krautkramer and Krautkramer 1990).

We expect that the differences in center frequency, bandwidth, and the near-field-to-far-field transition zone will have some impact on the ability to detect flaws. Previous studies (Dib et al. 2017) showed variations in computed beam amplitudes and flaw response amplitudes due to variations in any one of these transducer parameters. From the perspective of simulation studies, using the nominal specifications (either noted on the probe or from a vendor-provided specification sheet) as input to a simulation tool could result in simulation results that do not accurately reflect probe performance. However, the cumulative impact of these variations on flaw detection reliability will depend on the flaw size and location relative to the probe and will need to be quantified using simulation or empirical means. Furthermore, measured variability of transducer specifications can be used to set bounds for particular parameters for modeling. However, these bounds may need to be refined by determining if a particular parameter variation causes performance deviations exceeding the essential variable tolerance as described in Section XI of the ASME BPVC.

Future work will investigate performance variations of this set further by comparing beam profiles and beam divergence. It would also be valuable to expand the set of transducers to include new ones where use history is known to determine how much variability can be expected from new probes.

8.0 Conclusions and Future Work

The primary objective of the work described in this report was to evaluate the effectiveness of beam models with respect to quantifying volumetric coverage and flaw detection capability. Included in the evaluation was the identification of key variables in typical simulation models that influence coverage extent and flaw detection capability.

A comparison of two different commercially used software simulation tools was first conducted to obtain a baseline indication of the variability across different modeling software packages. This comparison showed some differences between the two tools; however, these differences were likely the result of different underlying beam models (one based on ray theory and the other on angular spectrum). The results observed in this comparison suggest several factors that may influence the computed beam profiles, of which only the parameters representing the transducer are controllable by the user. These capabilities and limitations should be better understood prior to their use in estimating flaw detection capability, especially if such estimates are based on beam models. Consequently, users attempting to employ any simulation software (whether the two evaluated here, or others) should have an understanding of the models implemented and the resulting capabilities and limitations of these models prior to drawing conclusions.

While beam models in isotropic materials are reasonably accurate (regardless of the software tool used), their use in anisotropic or complex microstructures is more challenging. Results on a limited set of austenitic weldments indicated that the computed beam profiles through the welds were qualitatively in agreement with experiments; however, the accuracy of the simulation appeared to depend on the accuracy with which the weld material properties can be established.

A key question that arises from these findings is the ability to assess flaw detection capability based on simulated beam models. To assist in this assessment, we defined two metrics—a total beam amplitude metric that acted as a simple surrogate for the total ultrasound energy insonifying the flaw, and the specularly reflected signal from a flaw (flaw backscatter amplitude). Other metrics for the beam model were also computed, including the beam amplitude at the backwall. Results discussed in this report pointed to the difficulties inherent in using beam models as surrogates for flaw detection, regardless of the specific metrics used. In general, beam amplitudes (relative or absolute) appear to contain limited information about the ability to obtain a high flaw response amplitude. This is also true when examining limited coverage conditions, where the probe has limited scan range. In this case, the probe position that optimizes flaw response for detection may not correlate with the probe position for maximal beam insonification of the flaw. This lack of consistent correlation between beam energy and range with the received energy from flaw backscatter has implications for the use of beam models for quantitatively comparing probe performance on flaw detection and estimating volumetric coverage. The primary conclusion that may be drawn, therefore, is that interpretation of beam simulation results in terms of flaw detection capability is challenging. The way to assess UT reliability with models is to use flaw response models. However, additional challenges are inherent for assessing UT reliability, even with flaw response models, as adequate care must be taken to address unknowns in model implementation and normalization procedures, uncertainties in material property specification, and uncertainties in transducer parameters.

Given these findings, we conclude that the beam amplitude incident on a flaw does not appear to be an informative measure of expected flaw detection reliability. As a corollary, comparing the performance of probes with respect to flaw detection capability will likely require additional information, beyond the amount of ultrasound energy incident in a volume. Finally, simulation models will need to include the effects of beam interaction with the backwall and other geometric factors to compute the total beam energy incident on the flaw, and the interaction of the energy with the flaw itself, to obtain a comprehensive understanding of flaw detection capabilities in both full and limited coverage scenarios.

Initial results also show that the accuracy of simulations for flaw detection estimates, when the flaws are in the vicinity of welds, can be limited. This is not surprising, given the need for accurate material property information. However, there are also limitations with respect to the ability to accurately model the interaction of ultrasound with geometric indications (weld root and counterbore, for instance) in a computationally rapid manner. As a result, models may be applied to qualitatively assess and compare inspection capabilities. Quantitative results are likely to require additional steps in the modeling approach, including better quantification of variability in model input parameters and improved computational techniques for faster solutions.

A first step toward assessing model uncertainties was to quantify the variability in ultrasonic probe parameters. An experimental analysis indicated that the variability in the center frequency, bandwidth, and probe effective element size could be large (several percent). While previous sensitivity studies have shown limited impact of this level of variability on simulation results in isotropic materials, it is possible that the variability becomes significant when simulating complex materials. Additional studies in this area are planned to quantify the variability and sensitivity associated with these and other parameters.

Ongoing and future research will need to address several open questions, including:

- Parametric uncertainty. Uncertainty in input parameters continues to present challenges with respect to capturing their effects on simulation results and the conclusions that can be drawn from these results. Empirical measurements are expected to be necessary for insights into the level of variability on input parameters (transducers, specimen material properties and microstructure, and flaw morphologies). In addition, several other sources of experimental uncertainty exist, such as equipment and cabling, and a representative subset will need to be characterized to quantify their impact on the results. Parametric studies and sensitivity analyses can then be applied to quantify the effects of limited parametric knowledge on UT effectiveness and reliability, and to identify model inputs where limited knowledge of the input value has the greatest impact on the result.
- Material noise. Computational models that account for material noise and clutter from geometric conditions are expensive in computing time and resources. Techniques are therefore needed to simplify the computation of these effects, in a manner that is representative of experiment.
- Data analysis methods. Stochastic methods are needed to characterize model uncertainty and bias while accounting for noise. Inherent in the development of these methods are appropriate metrics. While the present study used simplified metrics as surrogates for beam energy and flaw detection, alternate metrics that capture the echo-dynamics of the flaw response may be appropriate for a comprehensive assessment of modeling accuracy and flaw detection capability from model results.

9.0 References

Adler L, KV Cook and DW Fitting. 1978. "Ultrasonic Characterization of Austenitic Welds." In *Proceedings of the First International Symposium on Ultrasonic Materials Characterization*, pp. 533-540. June 7-9, 1978, Gaithersburg, MD. Available at https://www.osti.gov/servlets/purl/6672819.

Anderson MT, AA Diaz, AD Cinson, SL Crawford, SE Cumblidge, SR Doctor, KM Denslow and S Ahmed. 2011. *An Assessment of Ultrasonic Techniques for Far-Side Examinations of Austenitic Stainless Steel Piping Welds*. NUREG/CR-7113, PNNL-19353. Washington, D.C.: U.S. Nuclear Regulatory Commission. ADAMS Accession No. ML12011A130.

Apfel A, J Moysan, G Corneloup, T Fouquet and B Chassignole. 2005. "Coupling an Ultrasonic Propagation Code with a Model of the Heterogeneity of Multipass Welds to Simulate Ultrasonic Testing." *Ultrasonics* 43(6):447-456. DOI: 10.1016/j.ultras.2004.09.004.

ASTM E1065-14. 2014. *Standard Guide for Evaluating Characteristics of Ultrasonic Search Units*, West Conshohocken, Pennsylvania, www.astm.org: ASTM International.

Bathe K-J. 2014. *Finite Element Procedures, Second Edition*, Watertown, Massachusetts: KJ Bathe. ISBN 978-0-9790049-5-7.

Brokešová J. 2006. *Asymptotic Ray Method in Seismology – A Tutorial*. Publication No. 168. Matfyzpress. Available at http://geo.mff.cuni.cz/studium/Brokesova-AsymptoticRayMethod.pdf.

Calmon P, S Mahaut, S Chatillon and R Raillon. 2006. "CIVA: An Expertise Platform for Simulation and Processing NDT Data." *Ultrasonics* 44:e975-e979. DOI: 10.1016/j.ultras.2006.05.218.

Červený V. 2001. *Seismic Ray Theory*, Cambridge, New York: Cambridge University Press.

Chassignole B, D Villard and M Dubuget. 2000. "Characterization of Austenitic Stainless Steel Welds for Ultrasonic NDT." In *Review of Progress in Quantitative Nondestructive Evaluation, Vol. 19*, pp. 1325-1332. July 25-30, 1999, Montreal, Canada. DOI 10.1063/1.1307835. American Institute of Physics, Melville, New York.

Chassignole B, O Dupond, L Doudet, V Duwig and N Etchegaray. 2008. "Ultrasonic Examination of an Austenitic Weld: Illustration of the Disturbances of the Ultrasonic Beam." In *Review of Quantitative Nondestructive Evaluation, Vol. 28*, pp. 1886-1893. July 20-25, 2008, Chicago. American Institute of Physics, Melville, New York.

Chassignole B, O Dupond and L Doudet. 2009. "Ultrasonic and Metallurgical Examination of an Alloy 182 Welding Mold." In *Proceedings of the Seventh International Conference on NDE in Relation to Structural Integrity for Nuclear and Pessurised Components*, pp. 12-15. May 12-14, 2009, Yokohama, Japan.

CIG. 2015. "SPECFEM3D_GLOBE." University of California, Davis, California: Computational Infrastructure for Geodynamics. Accessed June 18, 2018. Available at https://geodynamics.org/cig/software/specfem3d_globe/.

Crawford SL, MS Prowant, AD Cinson, MR Larche, AA Diaz and MT Anderson. 2014. *Phased Array Ultrasonic Sound Field Mapping in Cast Austenitic Stainless Steel*. PNNL-23393. Richland, Washington: Pacific Northwest National Laboratory. ADAMS Accession No. ML14155A165.

Darmon M, R Raillon, V Dorval, S Chatillon and L Fradkin. 2013. "Generic GTD-Kirchhoff Scattering Model for the Ultrasonic Response of Planar Defects." In *10th International Conference on NDE in Relation to Structural Integrity for Nuclear and Pressurized Components*, pp. 675-683. October 1-3, 2013, Cannes, France. Joint Research Centre. Available at https://www.ndt.net/article/jrc-nde2013/papers/675.pdf.

Dib G, SL Crawford, RE Jacob, MS Prowant and AA Diaz. 2017. *Validation of Ultrasonic Nondestructive Examination (NDE) Computational Models - Phase 1*. PNNL-26336. Richland, Washington: Pacific Northwest National Laboratory. ADAMS Accession No. ML17082A190.

EPRI. 2013. *PDI-UT-2 Generic EPRI Procedure for the Ultrasonic Examination of Austenitic Pipe Welds Rev F*. PDI-UT-2, Revision F. Palo Alto, California: Electric Power Research Institute.

Gardahaut A, K Jezzine and D Cassereau. 2012. "Modelling Tools for Ultrasonic Inspection of Bimetallic Welds." In *Acoustics 2012*. 2012-04-23, Nantes, France. Available at https://hal.archives-ouvertes.fr/hal-00811043.

Gardahaut A, K Jezzine and D Cassereau. 2014a. "Paraxial Ray-Tracing Approach for the Simulation of Ultrasonic Inspection of Welds." *AIP Conference Proceedings* 1581(1):529-536. DOI: 10.1063/1.4864865.

Gardahaut A, H Lourme, F Jensen, S Lin and M Nagai. 2014b. "Ultrasonic Wave Propagation in Dissimilar Metal Welds - Application of a Ray-Based Model and Comparison with Experimental Results." In *11th European Conference on Non-Destructive Testing (ECNDT 2014)*, pp. 302-311. October 6-10, 2014, Prague, Czech Republic. European Federation for Non-Destructive Testing.

Huthwaite P. 2014. "Pogo." London: Imperial College. Accessed June 18, 2018. Available at http://www.pogo-fea.com/about.html.

ISU. 2018. "UTSIM." Ames, Iowa: Iowa State University, Center for Nondestructive Evaluation. Available at https://www.cnde.iastate.edu/research/ultrasonic/utsim/.

Jenson F, T Fortuna and L Doudet. 2009. "Modeling of Ultrasonic Propagation in a Coarse Grain Structure." In *Proceedings of the 35th Annual Review of Progress in Quantitative Nondestructive Evaluation*, pp. 1201-1208. July 20-25, 2008, Chicago, Illinois. DOI 10.1063/1.3114091. American Institute of Physics, Melville, New York.

Jeonga H and LW Schmerr. 2007. "Ultrasonic Beam Propagation in Highly Anisotropic Materials Simulated by Multi-Gaussian Beams." *Journal of Mechanical Science and Technology* 21(8):1184-1190. DOI: 10.1007/bf03179034.

Jezzine K, A Gardahaut, N Leymarie and S Chatillon. 2013. "Evaluation of Ray-Based Methods for the Simulation of UT Welds Inspection." *AIP Conference Proceedings* 1511(1):1073-1080. DOI: 10.1063/1.4789162.

Keller JB. 1962. "Geometrical Theory of Diffraction." *Journal of the Optical Society of America* 52(2):116-130. DOI: 10.1364/JOSA.52.000116.

Krautkramer J and H Krautkramer. 1990. *Ultrasonic Testing of Materials, 4th Edition*, Berlin: Springer-Verlag.

Kupperman DS and KJ Reimann. 1980. "Ultrasonic Wave Propagation and Anisotropy in Austenitic Stainless Steel Weld Metal." *IEEE Transactions on Sonics and Ultrasonics* 27(1):7-14. DOI: 10.1109/T-SU.1980.31137.

Kupperman DS and KJ Reimann. 1981. "Deviation of Longitudinal and Shear Waves in Austenitic Stainless Steel Weld Metal." In *Proc. 3rd International Conference on Nondestructive Evaluation in the Nuclear Industry*. February 11-13, 1980, Salt Lake City, UT. American Society for Metals, Metals Park, OH. Available at https://inis.iaea.org/collection/NCLCollectionStore/_Public/11/548/11548418.pdf.

Mahaut S, S Lonne, L de Roumilly and G Cattiaux. 2006. "Validation of CIVA Simulation Tools for Ultrasonic Inspection in Realistic Configuration." In *9th European Conference on NDT*. September 25-29, 2006, Berlin, Germany. Session We.1.4.4.

Marple Jr. SL. 1987. *Digital Spectral Analysis: With Applications*, Prentice Hall Signal Processing SeriesPrentice Hall. ISBN 978-0132141499.

Moysan J, A Apfel, G Corneloup and B Chassignole. 2003. "Modeling the Grain Orientation of Austenitic Stainless Steel Multipass Welds to Improve Ultrasonic Assessment of Structural Integrity." *International Journal of Pressure Vessels and Piping* 80:77-85. DOI: 10.1016/S0308-0161(03)00024-3.

Moysan J, G Corneloup, B Chassignole, C Gueudré and MA Ploix. 2012. "Modelling Welded Material for Ultrasonic Testing Using MINA: Theory and Applications." *AIP Conference Proceedings* 1430(1):1219-1226. DOI: 10.1063/1.4716358.

Ogilvy JA. 1985. "Computerized Ultrasonic Ray Tracing in Austenitic Steel." *NDT International* 18(2):67-77. DOI: 10.1016/0308-9126(85)90100-2.

Ogilvy JA. 1986. "An Estimate of the Accuracy of the Kirchhoff Approximation in Acoustic Wave Scattering from Rough Surfaces." *Journal of Physics D: Applied Physics* 19(11):2085. DOI: 10.1088/0022-3727/19/11/008.

Rokhlin SI, TK Bolland and L Adler. 1986. "Reflection and Refraction of Elastic Waves on a Plane Interface Between Two Generally Anisotropic Media." *The Journal of the Acoustical Society of America* 79(4):906-918. DOI: 10.1121/1.393764.

Rose JL. 2004. *Ultrasonic Waves in Solid Media*, Cambridge, United Kingdom: Cambridge University Press.

Sakamoto K, T Furukawa, I Komura, Y Kamiyama and T Mihara. 2012. "Study on the Ultrasound Propagation in Cast Austenitic Stainless Steel." *E-Journal of Advanced Maintenance* 4(1). Available at http://www.jsm.or.jp/ejam/Vol.4No.1/AA/AA37/EJAM_CASS_Paper_sakamoto_Final_0419_.pdf.

Schmerr Jr. LW and S-J Song. 2007. *Ultrasonic Nondestructive Evaluation Systems – Models and Measurements*, New York: Springer.

Shi F, W Choi, MJS Lowe, EA Skelton and RV Craster. 2015. "The Validity of Kirchhoff Theory for Scattering of Elastic Waves from Rough Surfaces." *Proceedings of the Royal Society A: Mathematical, Physical & Engineering Science* 471(2178). DOI: 10.1098/rspa.2014.0977.

Silk MG. 1984. *Ultrasonic Transducers for Nondestructive Testing*, Bristol: Adam Hilger, Ltd. ISBN 0-85274-436-6.

Szávai S, Z Bézi, J Dudra and I Méhész. 2016. "Modelling of Phased Array Ultrasonic Inspection of a Steam Generator Dissimilar Metal Weld." *Procedia Structural Integrity* 2:1015-1022. DOI: 10.1016/j.prostr.2016.06.130.

Thompson RB and FJ Margetan. 2002. "Use of Elastodynamic Theories in the Stochastic Description of the Effects of Microstructure on Ultrasonic Flaw and Noise Signals." *Wave Motion* 36(4):347-365. DOI: 10.1016/S0165-2125(02)00029-X.

Thorsos EI. 1988. "The Validity of the Kirchhoff Approximation for Rough Surface Scattering Using a Gaussian Roughness Spectrum." *The Journal of the Acoustical Society of America* 83(1):78-92. DOI: 10.1121/1.396188.

Appendix A – Evaluation Procedures and Results

A.1 Frequency Response Evaluation

As described earlier, the frequency response measurements of the transducers in this study were performed in adherence to the ASTM E1065-14 standard (ASTM E1065-14 2014). The time-domain response of each transducer from an aluminum block was acquired as shown in Figure 7.2 and Figure 7.3. This setup used a pulse-echo mode for measuring the response from an aluminum block that was 85.83 mm (3.38 in.) thick. The aluminum block was submerged in water such that the wear face of the transducer was slightly submerged for consistent coupling. A 4.5 lb. weight was placed on the probe to provide consistent coupling pressure. For the two transducers with the micro-dot connector on the top of the housing, a load cell was used instead of the weight and 4.5 lbs. of coupling force was applied manually. The time-domain response (A-scan) was averaged across 50 traces and then recorded using an oscilloscope. The functional configuration of the setup used is shown in Figure A.1. The procedure used for acquiring the data is given below, and is followed by additional information on the analysis approach.

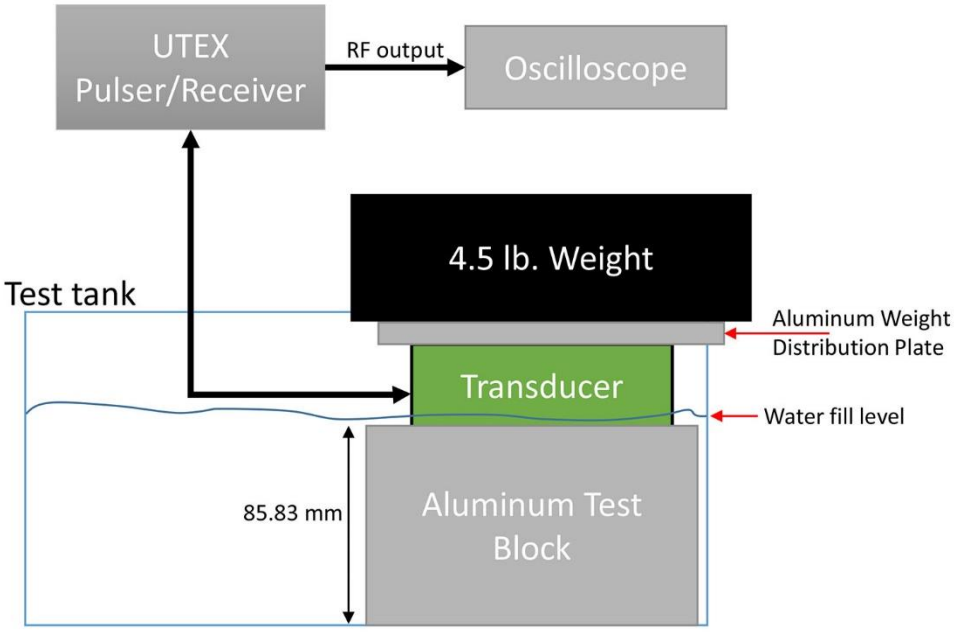

Figure A.1. Functional measurement configuration used for acquiring data for determining frequency response.

A.1.1 Measurement Procedure

1. Power on all equipment, and verify the pulser/receiver is not actively pulsing. Fill the test tank with water such that the top of the aluminum test block is slightly submerged. Allow the water to degas.
2. Place transducer on aluminum block test piece. The contact location shall be consistent for all probes being evaluated. Then place the machined plate on the transducer to provide a large contact surface for the weight. Carefully place a weight on the contact surface such that a consistent coupling is made between the aluminum test block and the transducer (see Figure 7.3).

3. Start Utex pulser/receiver. Allow the oscilloscope to acquire enough waveforms to satisfy the averaging. Modify the trace title to include the serial number of the transducer in the filename.
4. Record waveform to a binary file on oscilloscope (this format is preferred since the oscilloscope settings are saved with the data file).
5. Stop the Utex pulser/receiver. Remove the weight, machined plate, and transducer from the test part. Disconnect the cable.
6. Repeat this process for subsequent transducers.

   General acquisition notes:

   - To improve consistency of the results across all the transducers being evaluated, ensure that the same settings and equipment are used for each. The pulser/receiver settings as well as the oscilloscope settings did not vary among probes in this evaluation. The same cabling was used for all frequency response testing.
   - No filtering on the receiver or the oscilloscope was used to better isolate the impulse response of the transducers.

After the waveforms were acquired the data was post-processed using MATLAB. The FFT of the time-domain data was computed and the analysis approach described in ASTM E1065 was applied. Windowing was not applied to the waveform so as to not influence the bandwidth response of the spectral response. Zero-padding (appending zeros to the time domain signal) was used when applying the transform to more effectively enhance the spectral peaks in the frequency domain. Further information on the application and effects of windowing and zero-padding is provided in Marple Jr. (1987).

After zero-padding operations are conducted, the discrete FFT of the time-domain signal is computed. The built-in FFT function in MATLAB was used for this process. The resulting time-domain and frequency-domain response for each transducer featured in this study is provided in Figures A.2 through A.12.

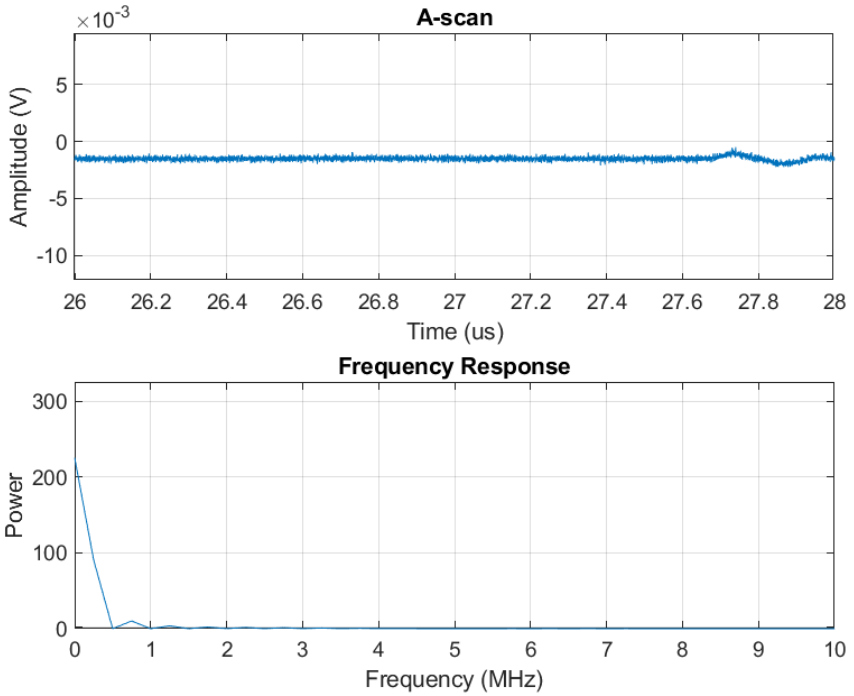

Figure A.2. Time and frequency response for Transducer #1.

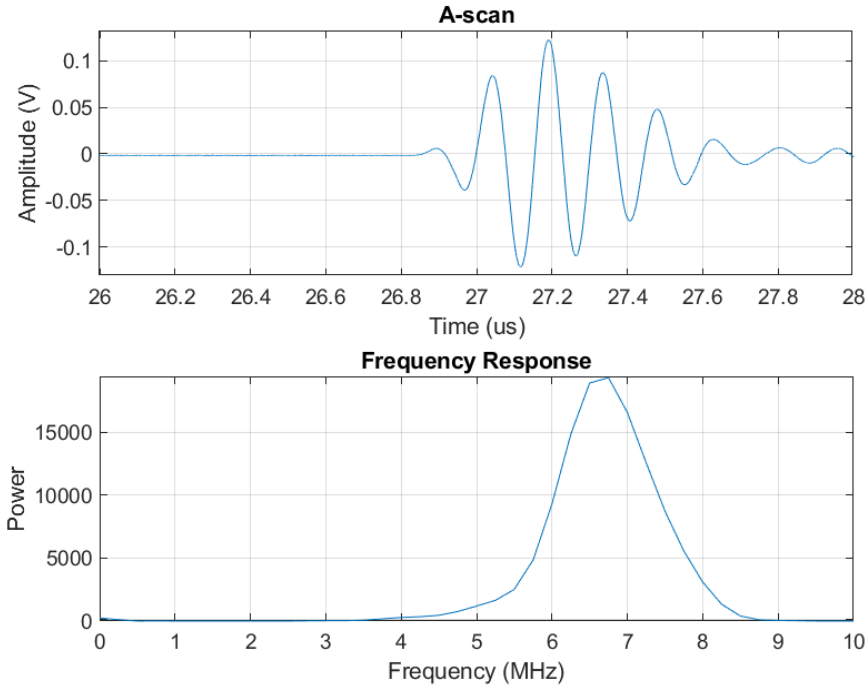

Figure A.3. Time and frequency response for Transducer #2.

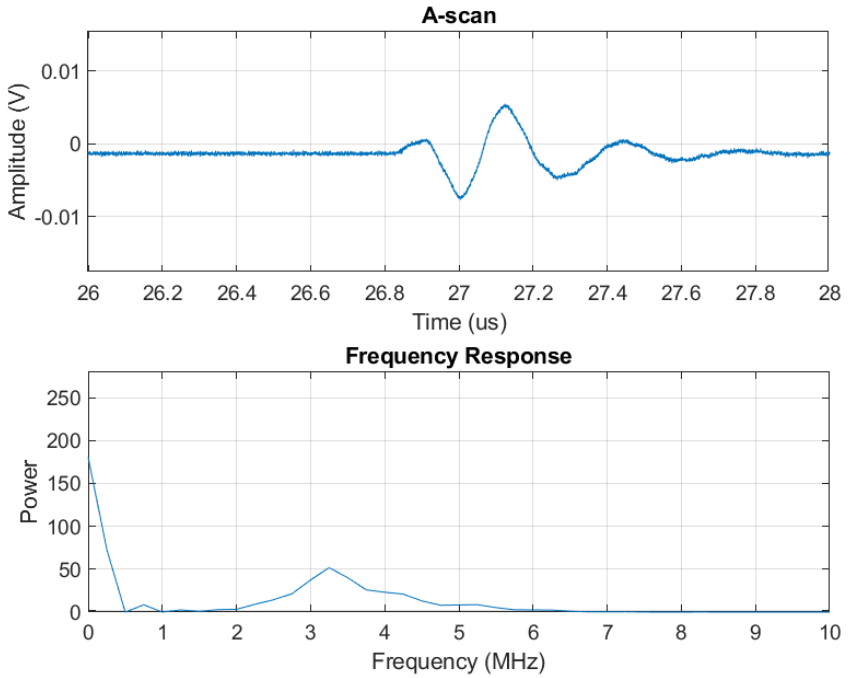

Figure A.4. Time and frequency response for Transducer #3.

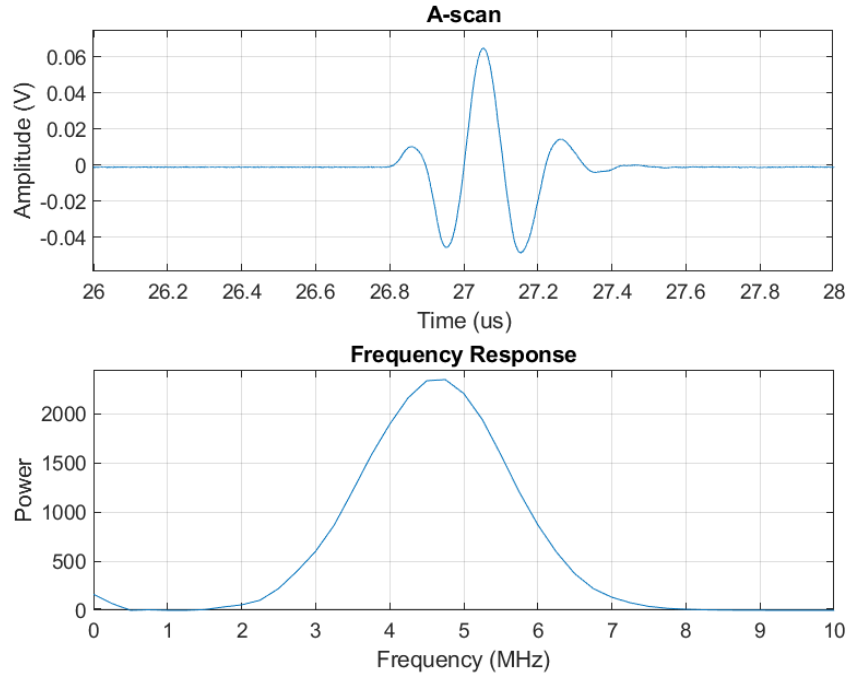

Figure A.5. Time and frequency response for Transducer #4.

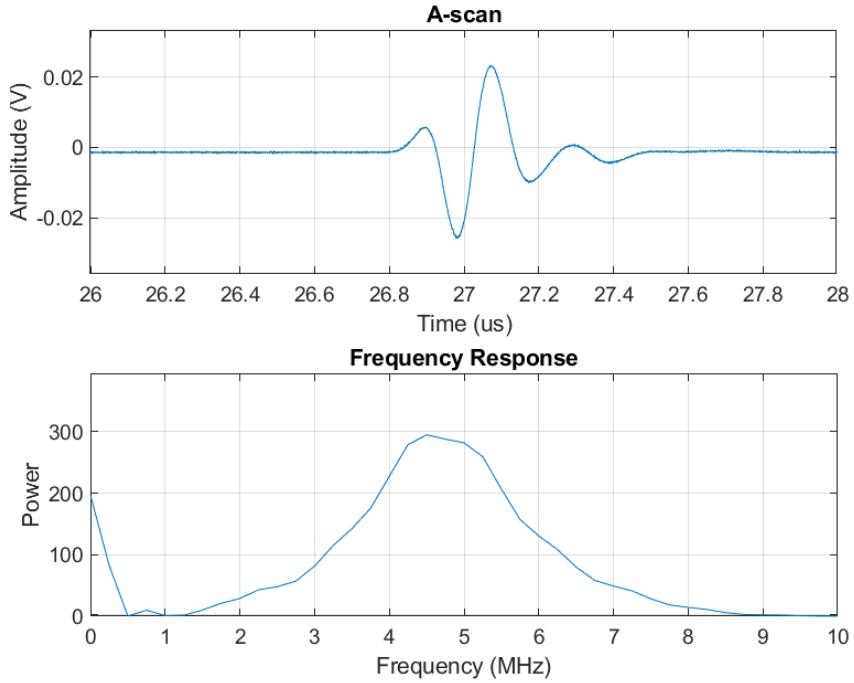

Figure A.6. Time and frequency response for Transducer #5.

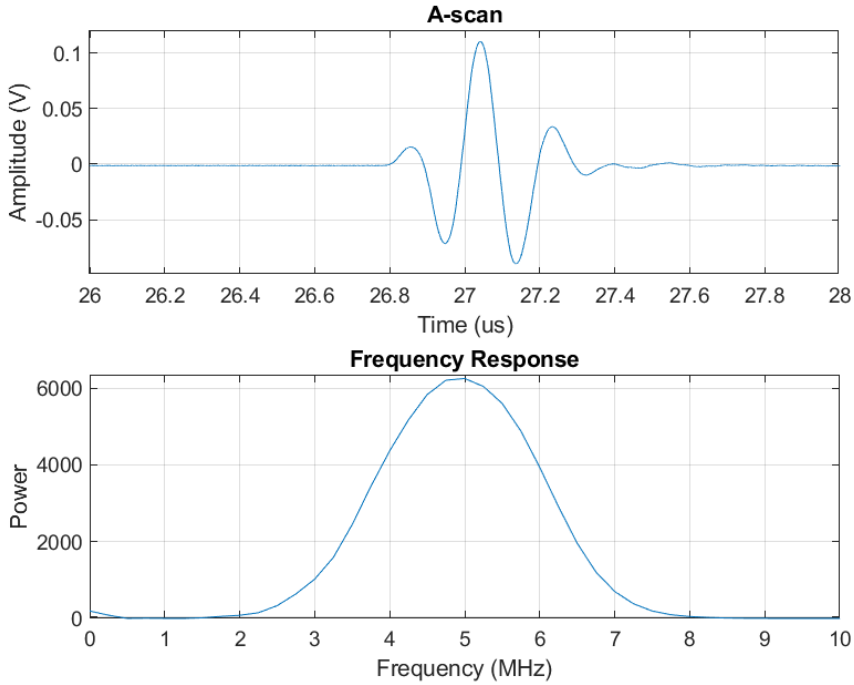

Figure A.7. Time and frequency response for Transducer #6.

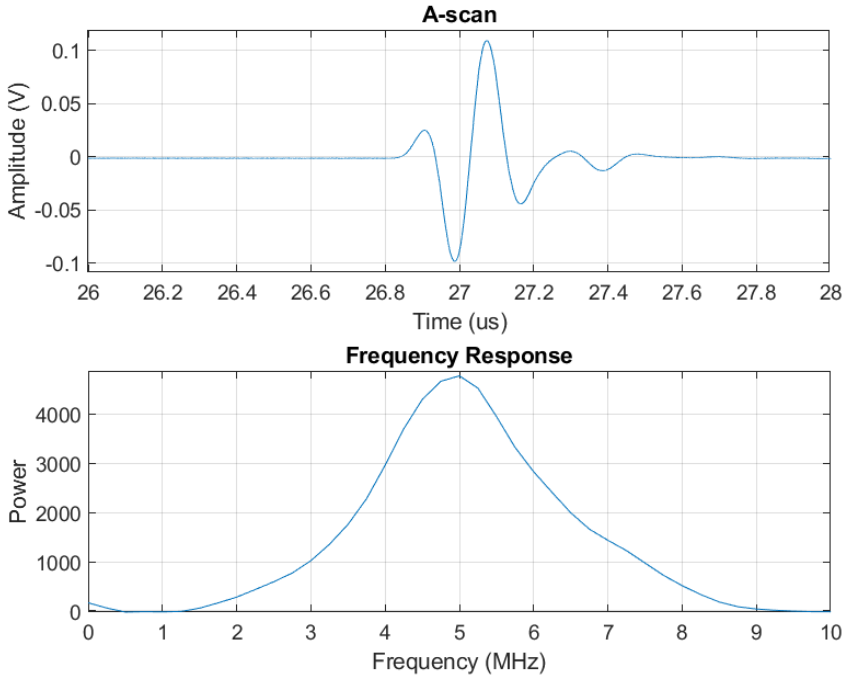

Figure A.8. Time and frequency response for Transducer #7.

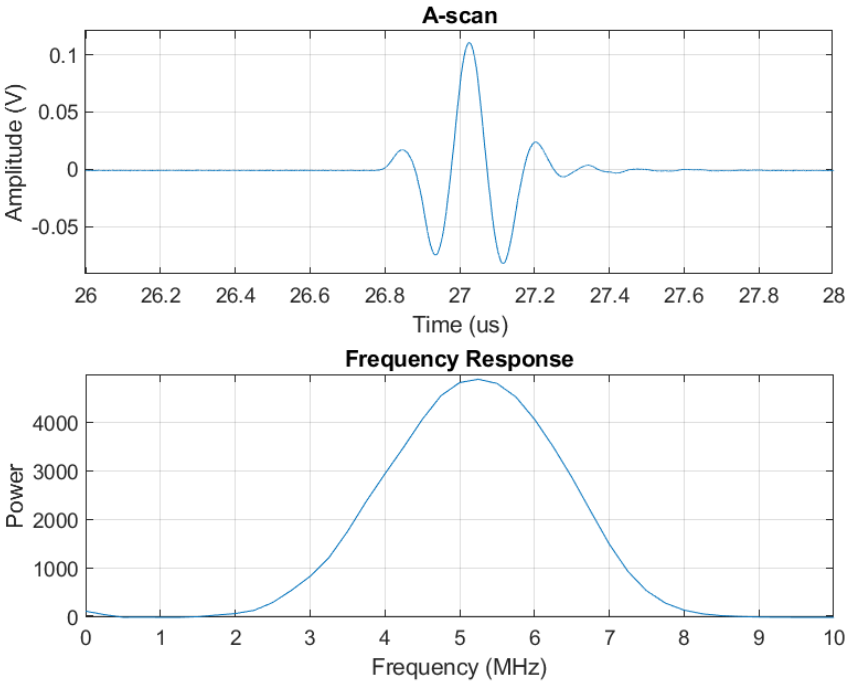

Figure A.9. Time and frequency response for Transducer #8.

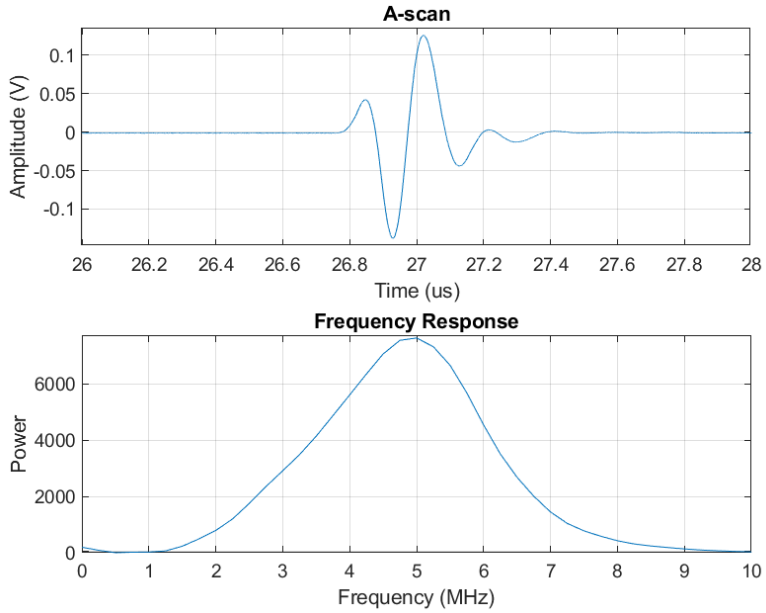

Figure A.10. Time and frequency response for Transducer #9.

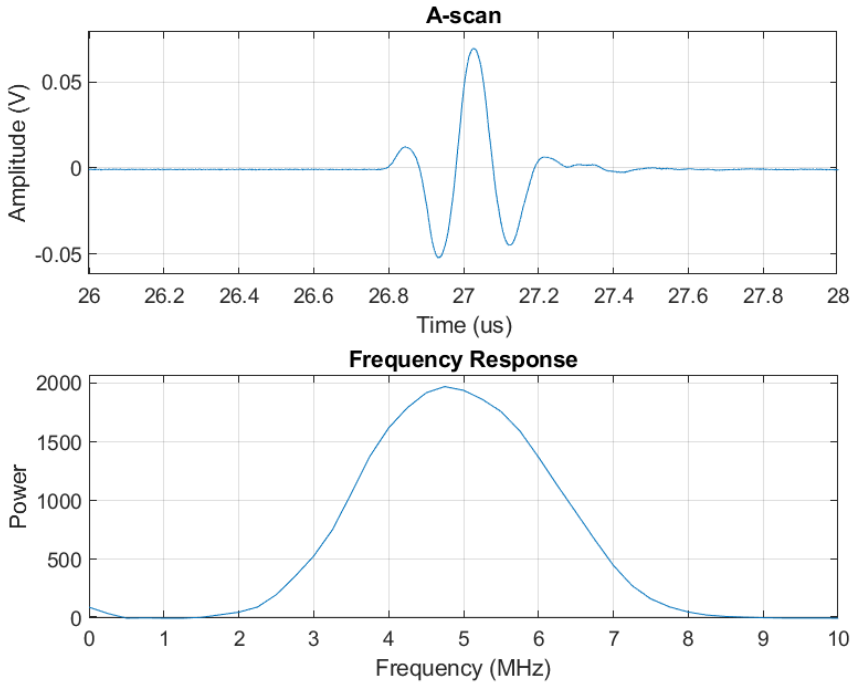

Figure A.11. Time and frequency response for Transducer #10.

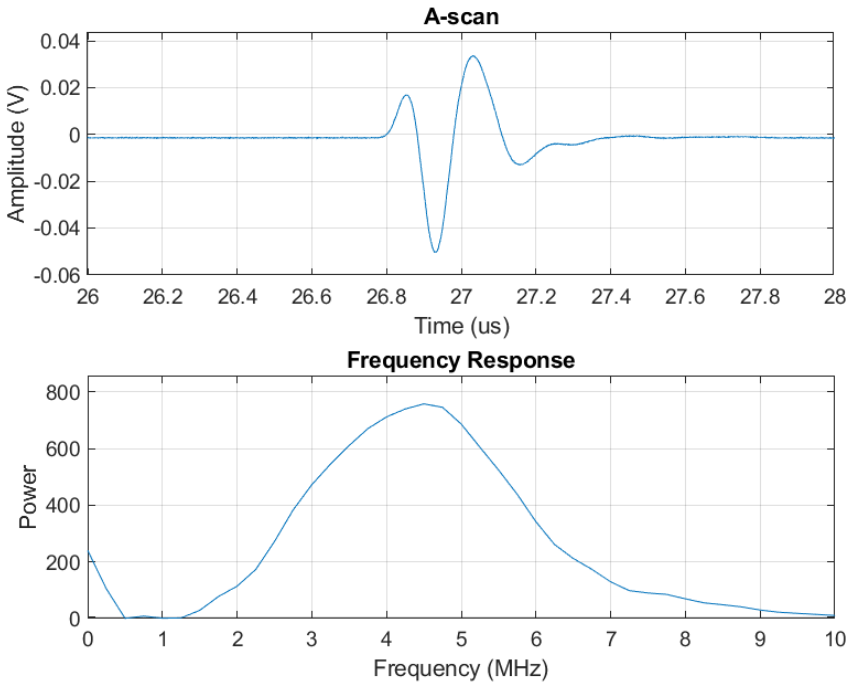

Figure A.12. Time and frequency response for Transducer #11.

A.2 Beam Profile Mapping Evaluation – Spherical Reflector

The functional diagram of the setup for this beam mapping study is provided in Figure A.13. In this setup a DYNARAY PA-UT data acquisition system is used to read the Z-axis encoder and provide a sync pulse to the pulser and oscilloscope at each step interval. The Stanford Research device is used to condition the DYNARAY trigger to a positive square wave trigger than is recognizable by the Utex and the oscilloscope.

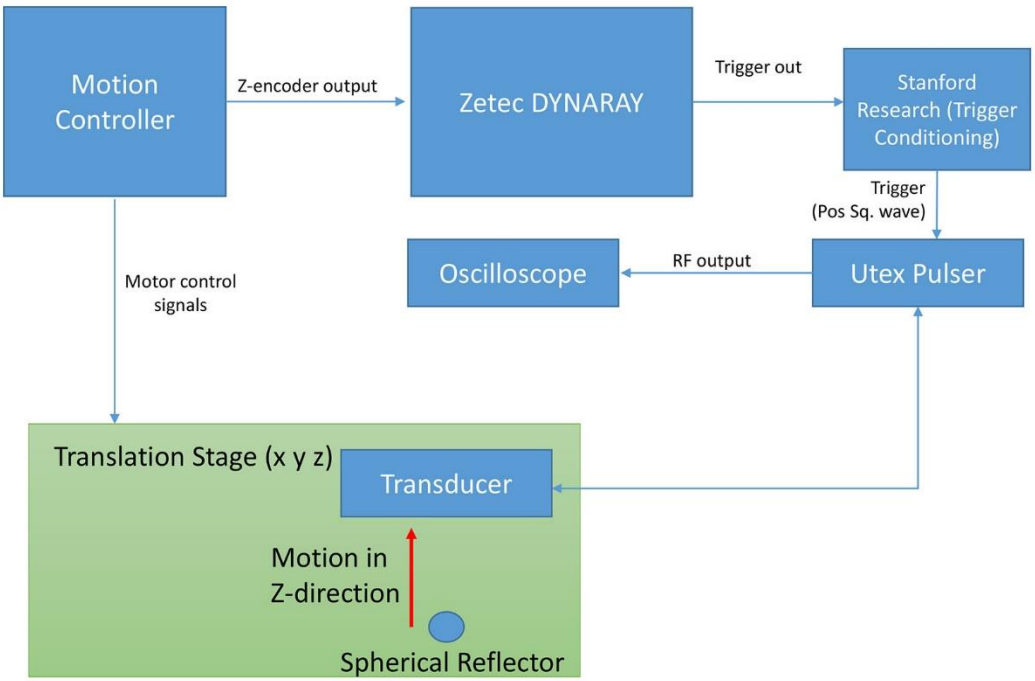

Figure A.13. Functional diagram of equipment configuration for beam profile mapping measurements.

A.2.1 Measurement Procedure

1. Power on all equipment and verify the pulser/receiver is not actively pulsing. Fill the test tank with water such that the spherical reflector can scan upward at least 150 mm (5.91 in.) toward the transducer. The reflector must scan from the far field, through the transition region, and into the near field. Allow the water to degas.
2. Mount the transducer on the aluminum holding fixture. Ensure the transducer is level and aligned with the translation stage. This alignment is critical for keeping the spherical reflector on the central axis of the transducer as it is being scanned along the Z-direction. Verify the micro-dot connector gasket on the probe is in good condition and replace if necessary. The wear face of the transducer must be slightly submerged in the immersion tank, but the connector should remain out of the water.
3. Start the Utex pulser/receiver using the internal trigger option. Peak the spherical reflector response on the oscilloscope display by moving the translation stage in the X- and Y-direction. Once the spherical reflector has been peaked, ensure the spherical reflector has room to travel the entire scan length and set the spherical reflector to the starting position.

4. Set the Utex to external trigger mode. Set the DYNARAY to a single line scan with the same resolution setting as the motion controller. Start the DYNARAY inspection. Set the oscilloscope to record waveforms to binary files when externally triggered.
5. Start the scan on the motion controller. Ensure that the oscilloscope is recording waveforms at the specific interval. Note that if the scan speed is too great, the oscilloscope will miss waveforms. This can be verified by counting the number of saved waveforms at the end of acquisition.
6. Once the acquisition is complete, stop the oscilloscope from automatically saving when triggered. Turn off the Utex pulser/receiver output.
7. Remove the transducer from the immersion tank and repeat this process for subsequent transducers.
8. Repeat the scan process to acquire replicate data sets.

   General acquisition notes:

   - To improve consistency of the results across all the transducers being evaluated, ensure that the same settings and equipment are used for each. The pulser/receiver settings as well as the oscilloscope settings did not vary among probes in this evaluation. The same cabling was used for all frequency response testing.
   - Scanner and motor noise was reduced through the use of bandpass filtering and grounding straps. The effect of noise was greater in this study because of the translation stage motors and due to the lack of averaging. The pulse-on-position configuration of the setup does not allow for taking a large number of waveforms and averaging them together to reduce transient signals.

Once the waveforms were acquired, a peak finding function was used to identify the spherical reflector response and plate response for the waveforms at each scan position. An example of the reflector peak detection for Transducer #3 is shown in Figure A.14. The black asterisk in the figure indicates the peak response from the spherical reflector. Shortly after this reflection is the response from the mounting plate. The spherical reflector response amplitude and time of flight were recorded from each waveform and used to plot the amplitude of the reflector response as a function of distance away from the transducer wear face. From these data, the near-field/far-field transition points along the transducer's primary axis were identified (also marked with a black asterisk) as shown in Figures A.15 through A.24. For Transducer #7 the profile response is shorter than the other transducers because some waveforms were removed from the scan where the spherical reflector response was buried in the noise.

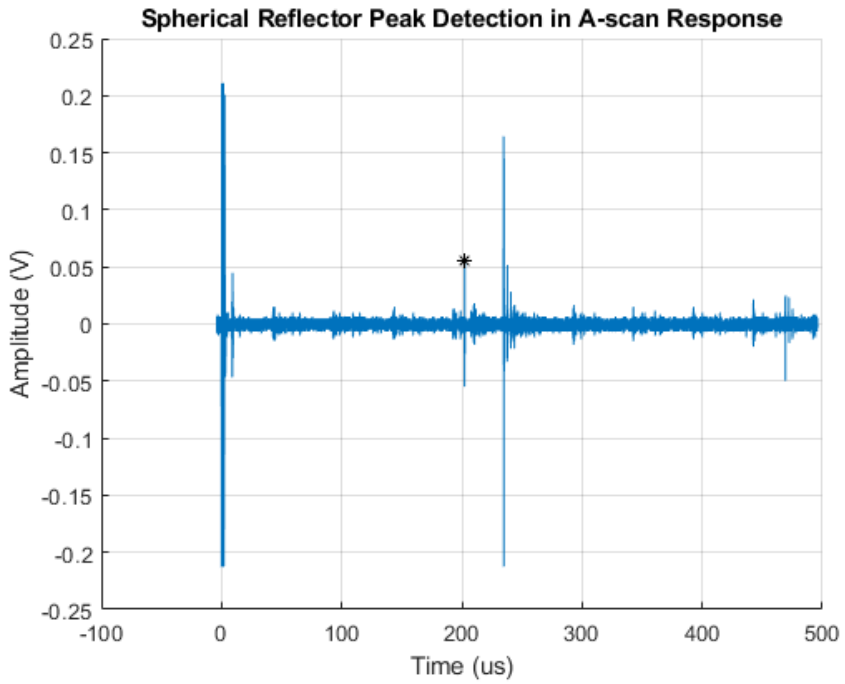

Figure A.14. Example A-scan from Transducer #10 showing peak detection of spherical reflector response.

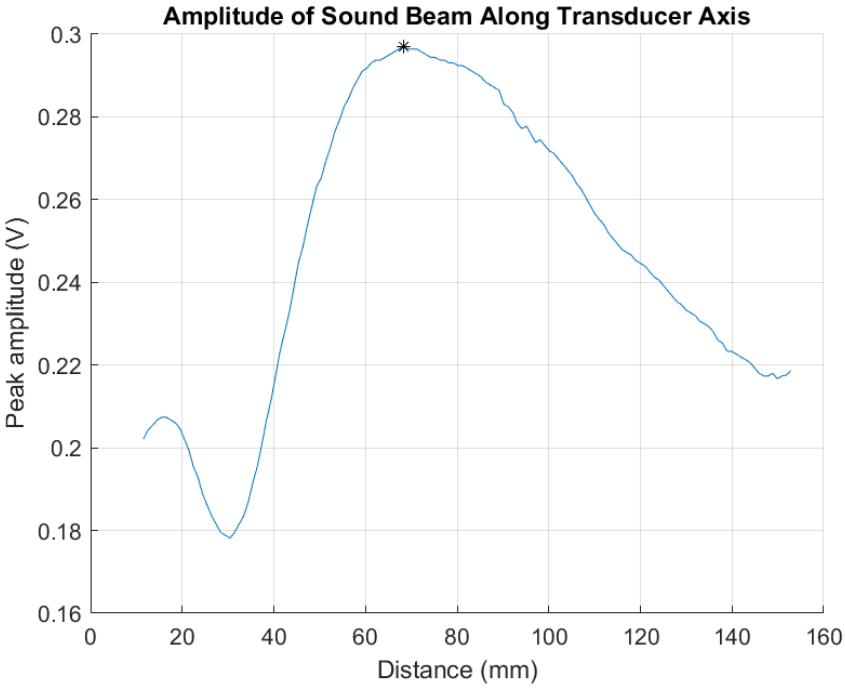

Figure A.15. Sound beam profile for Transducer #2.

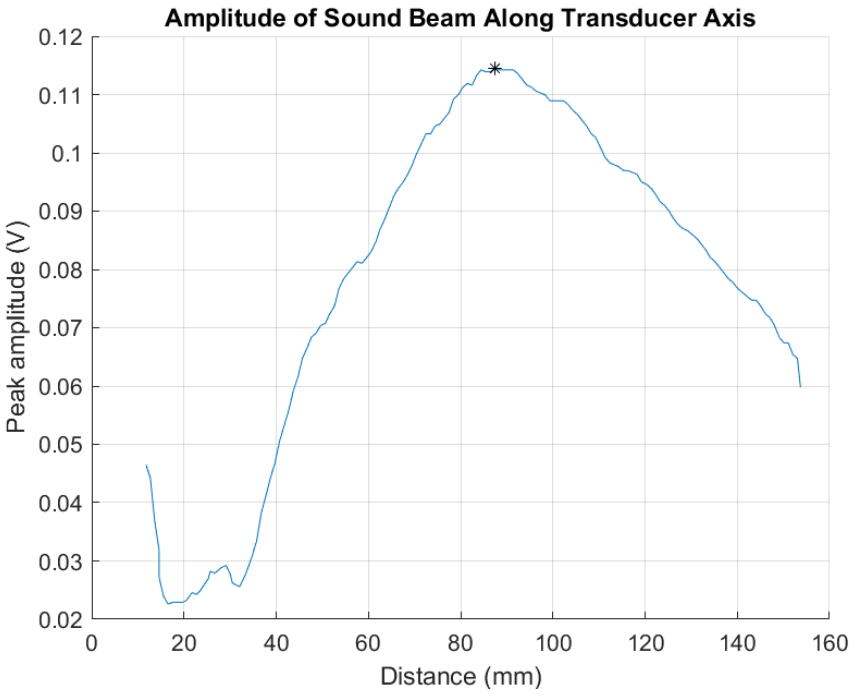

Figure A.16. Sound beam profile for Transducer #3.

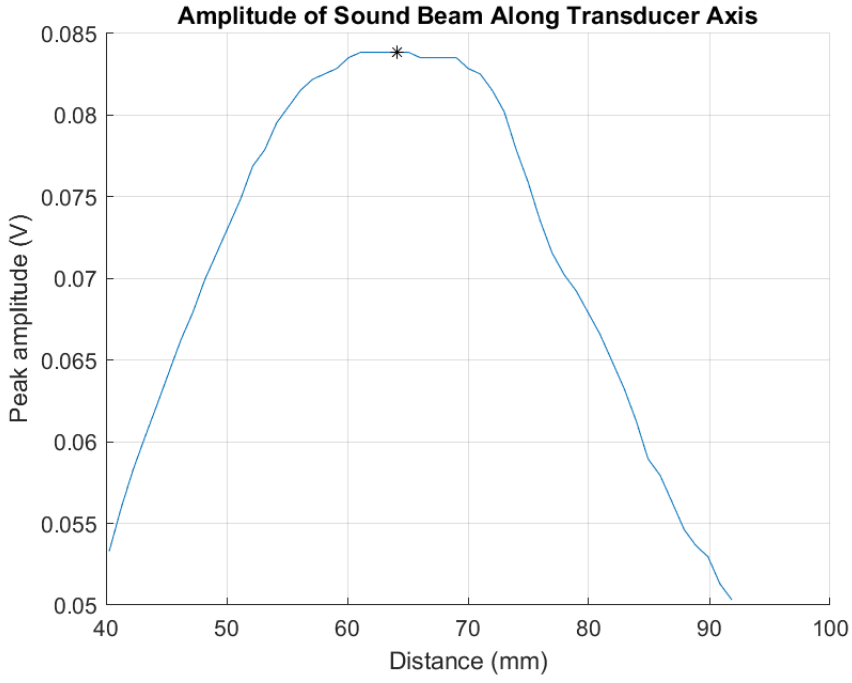

Figure A.17. Sound beam profile for Transducer #4.

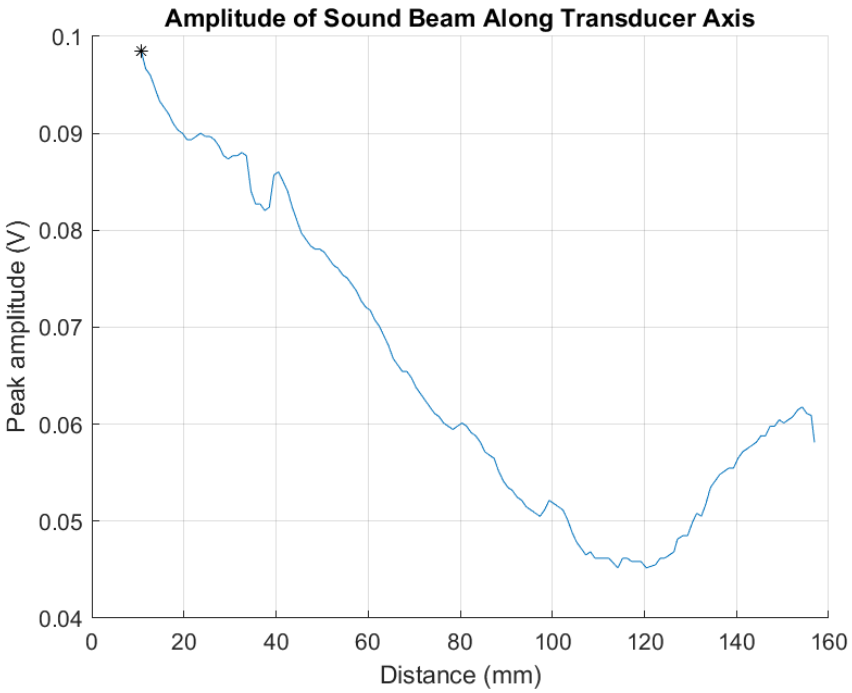

Figure A.18. Sound beam profile for Transducer #5.

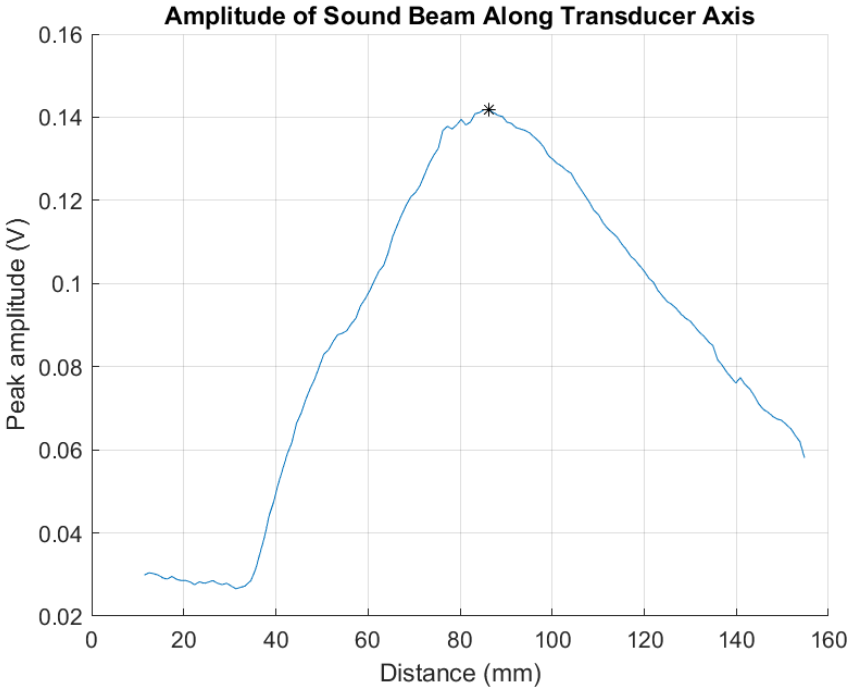

Figure A.19. Sound beam profile for Transducer #6.

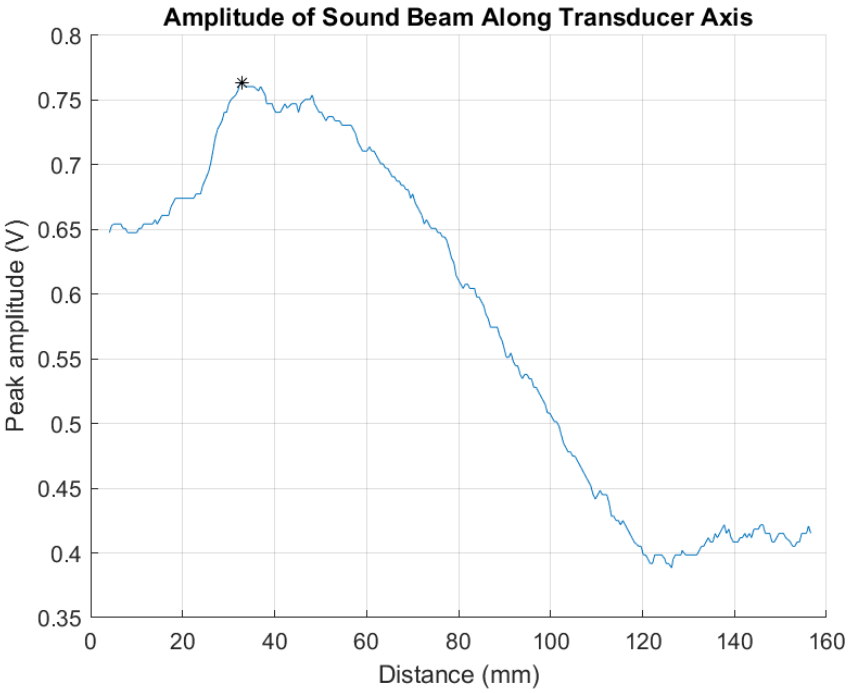

Figure A.20. Sound beam profile for Transducer #7.

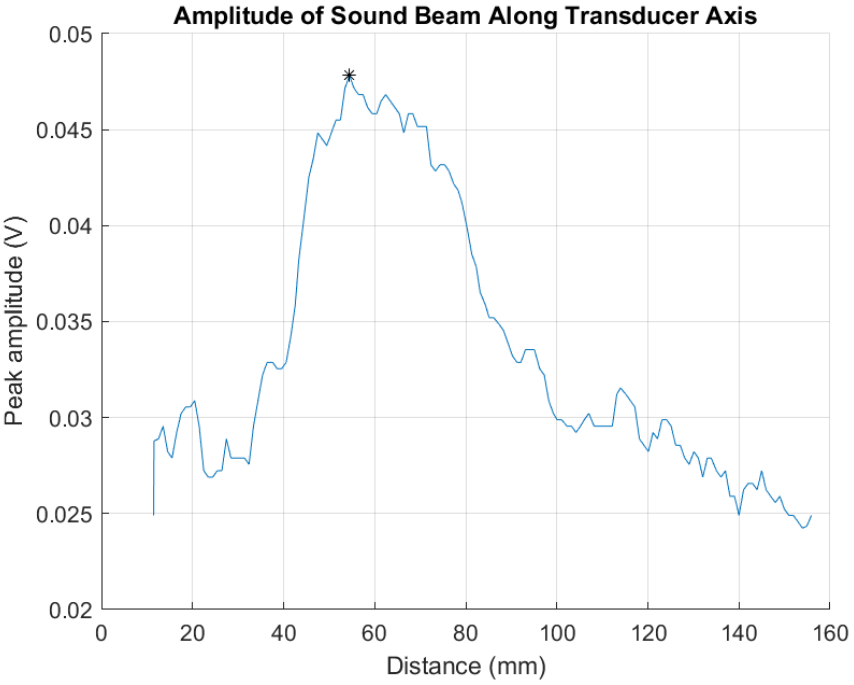

Figure A.21. Sound beam profile for Transducer #8.

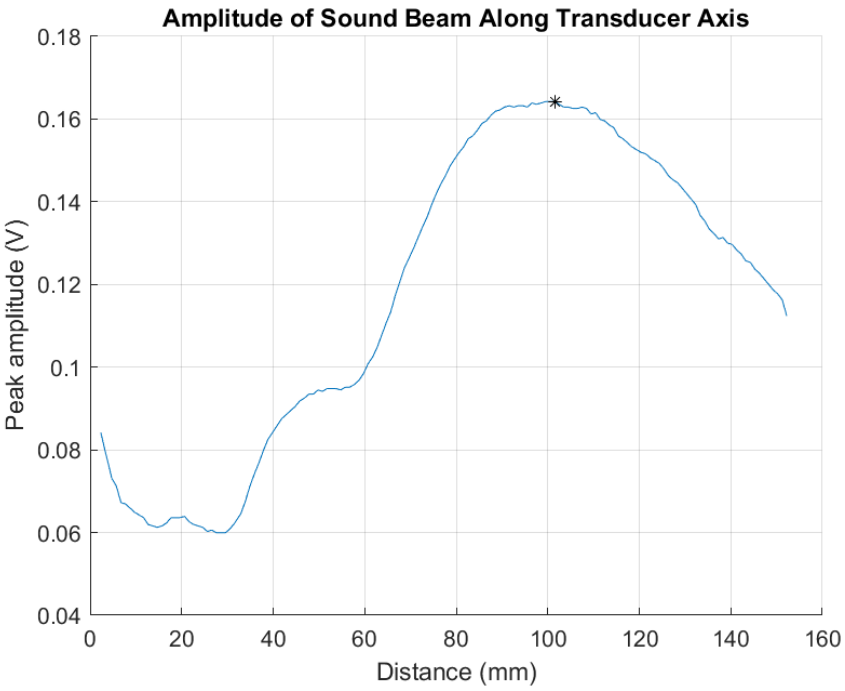

Figure A.22. Sound beam profile for Transducer #9.

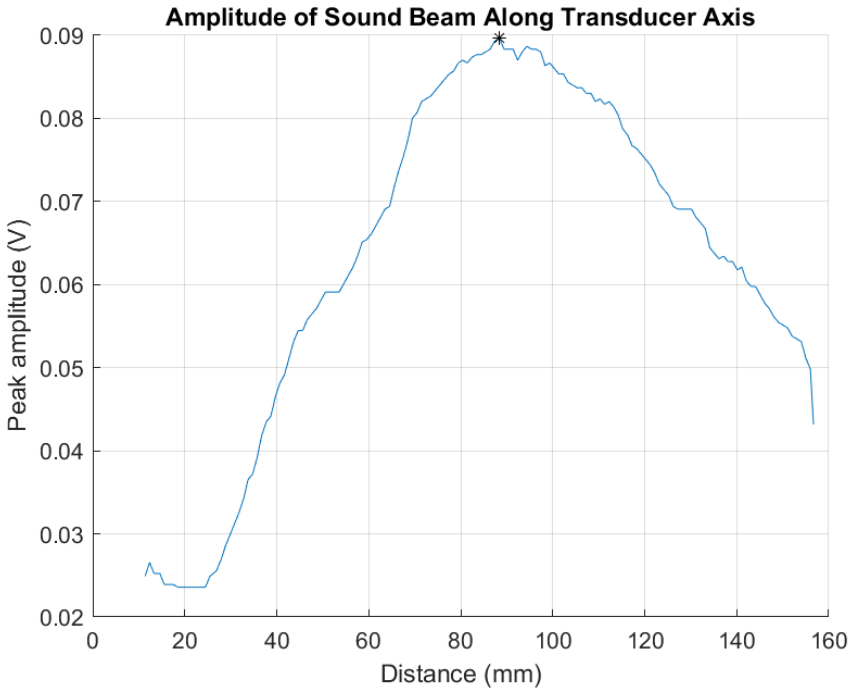

Figure A.23. Sound beam profile for Transducer #10.

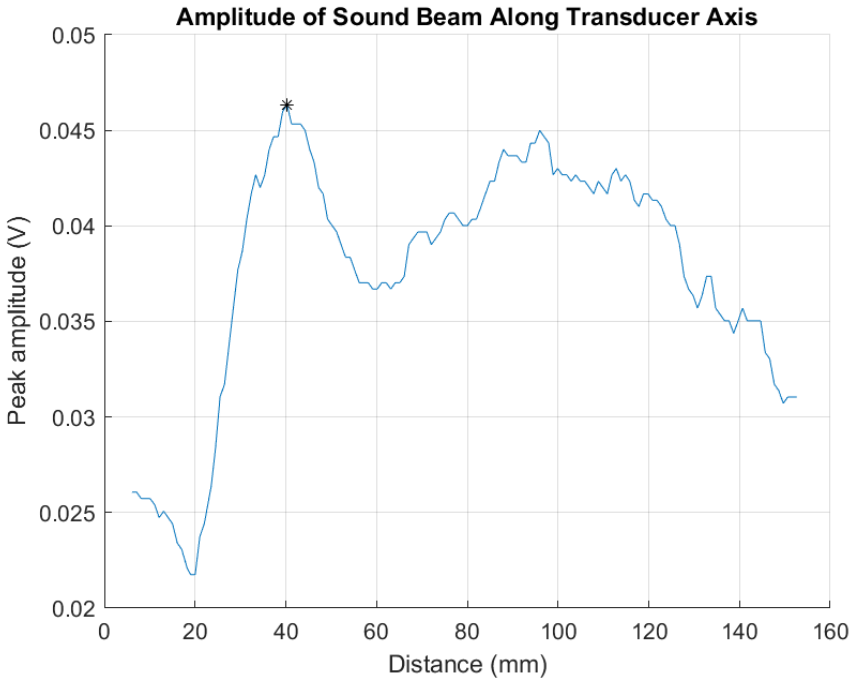

Figure A.24. Sound beam profile for Transducer #11.

A.3 Beam Profile Mapping Evaluation – Pinducer (Pencil Probe)

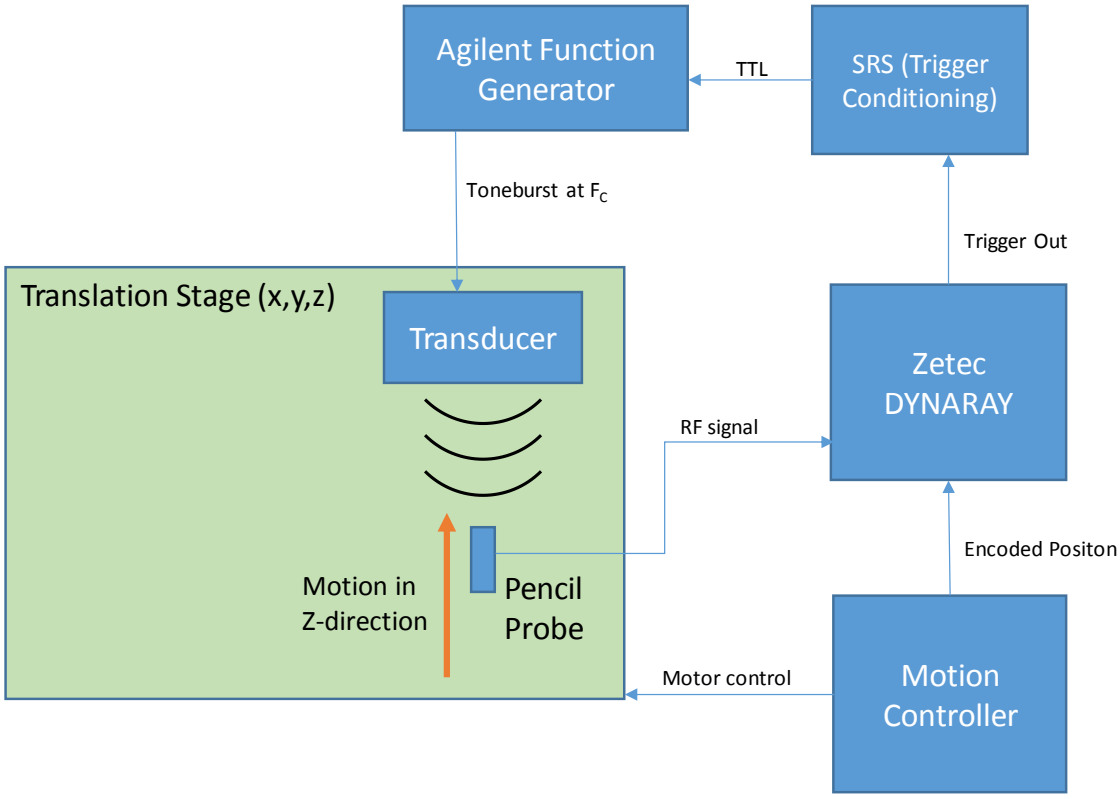

Figure A.25. Functional diagram of equipment setup in beam profile measurements.

A.3.1 Procedure

1. Power on all equipment, and verify the output of the function generator is not enabled. Assemble and immerse the receiving pinducer (pencil probe), checking that there are no air bubbles trapped within the sleeve fixture. Ensure water has degassed to prevent accumulation of bubbles during scans.
2. Mount the transducer being measured onto the scanner, taking care to make sure the face of the transducer is immersed and free of air bubbles. Verify the microdot connection gasket is in good condition and the connection to the probe is properly sealed. Avoid immersing the connection.
3. Physically align the pencil probe with the Z-axis of the scanner and adjust the transducer such that its face is normal to the Z-axis and parallel with the face of the pinducer. Jog the Z-axis to the top of its travel, adjusting the bar to create a known distance between the pencil probe and transducer faces within the estimated near-field of the transducer. Jog the motors in the X- and Y-axis to position the pencil probe under the approximate center of the transducer.
4. Configure the function generator to a toneburst at the measured center frequency of the probe (Appendix A.1) and to trigger externally. Enable the output of the function generator, and connect to the DYNARAY through UltraVision (UV) software, loading the setup file for transducer alignment. Verify at this point the A-scan response of the transducer observed by the pencil probe and displayed in UV.
5. Using the center of the probe face as the origin, set the known position in both the UV software and motion-control software as physically measured. Move controlled distances in all three axes, verifying the encoder calibration in UV.
6. Align the transducer with the Z-axis.
    a. Record an XY scan over a square area in the X- and Y-axis, extending ~20% beyond the theoretical aperture size of the transducer, with a resolution of 0.25 mm (0.010 in.).
    b. Once the scan is completed, adjust the axes origin to align with the measured center of the collected spot scan and reset the encoder positions in both UV and the motion control software.
    c. Move the Z-axis to a fixed point near the bottom of its travel.
    d. Record an XY scan using the same area and resolution as step (6a).
    e. Once the scan is completed, compare it to the scan taken at the top of the Z-axis travel. The measured distance between the spot centers, in both the X and Y axes, should result in no greater than a 0.5° alignment error of the probe in either axis. Adjust the alignment of the transducer to account for the angle error measured and move the Z-axis back to the previous point at the top of its travel.
    f. Repeat step 6 until the center of the two scans alignment error of no greater than 0.5° of the transducer in both the X- and Y-axis.
7. Move the scanner to the origin in both X- and Y-axis, and a point near the bottom of the Z-axis travel. Load the Profile Line setup file in UltraVision and verify the encoders are properly aligned and calibrated. Set the scan parameters to run the range of Z-axis travel with an increment of 0.1 mm (0.004 in.).
8. Record the encoded line scan data along the Z-axis.

9. Disable output from function generator and remove transducer being characterized. If additional probes are to be characterized, repeat procedure starting at Step 2. When finished, power down all equipment and remove the pencil probe from the water.

Following data acquisition, the transducer profile line scans were exported from UV and loaded into MatLab. An example of an A-scan, recorded from Transducer #10, is shown in Figure A.26. The magnitude of the A-scan responses were plotted with respect to position, and then smoothed using a moving average filter to reduce noise. Once filtered, each transducer profile was analyzed to find the peak, representing the distance of the near-field/far-field transition. Figures A.35 to A.36 show the raw and smoothed sound beam profiles of the transducer data collected (with the sign inverted so that distance from the probe is positive), as well as a blue line marking the transition point.

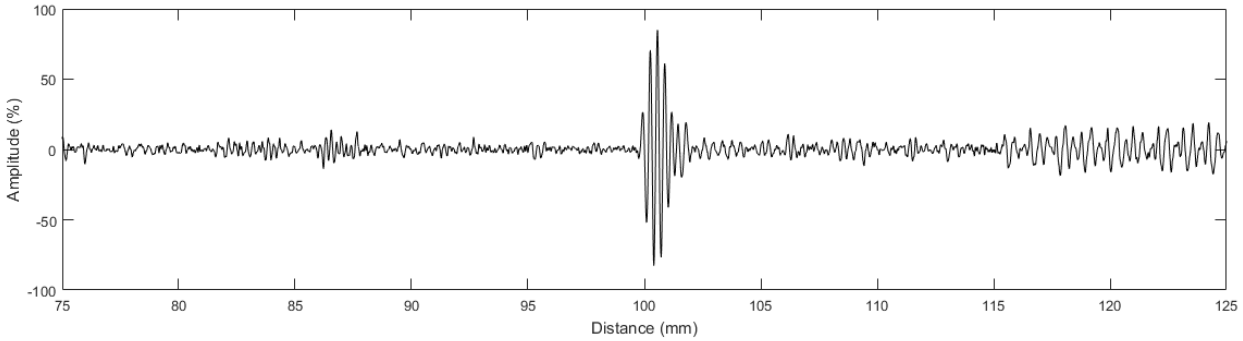

Figure A.26. A-scan from Transducer #10.

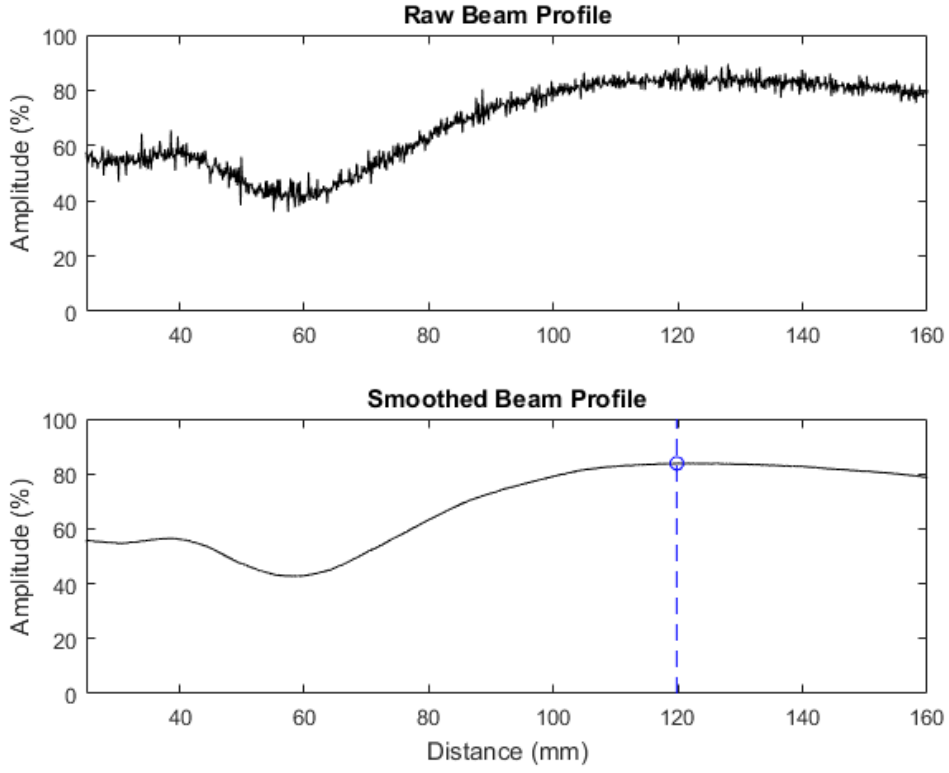

Figure A.27. Raw sound beam profile (top) and filtered (bottom) of Transducer #2.

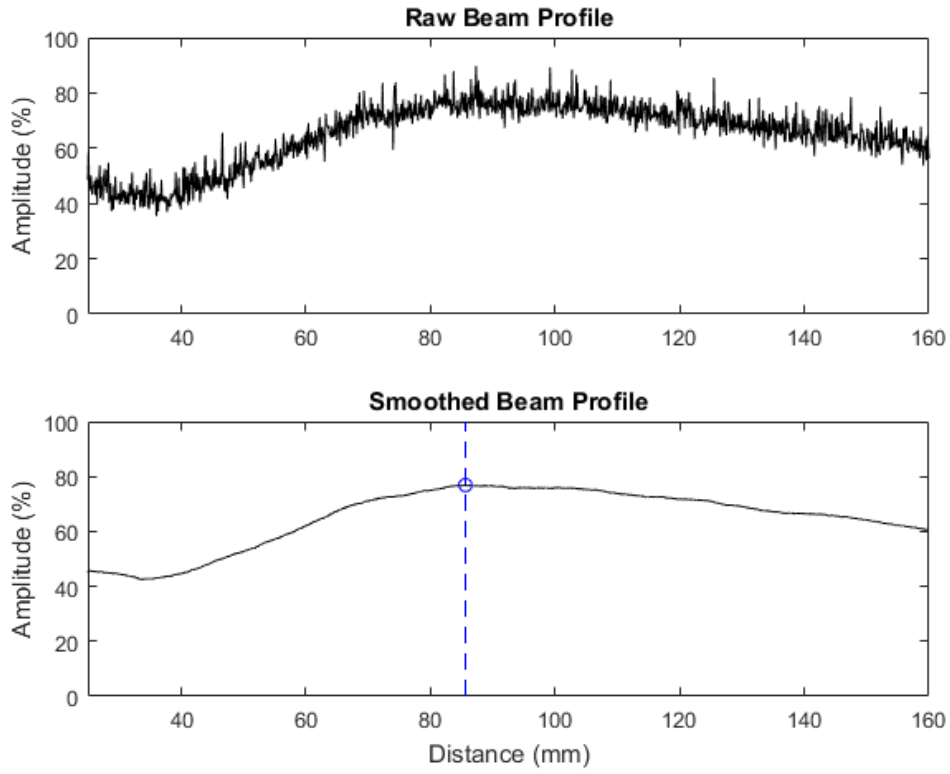

Figure A.28. Raw sound beam profile (top) and filtered (bottom) of Transducer #3.

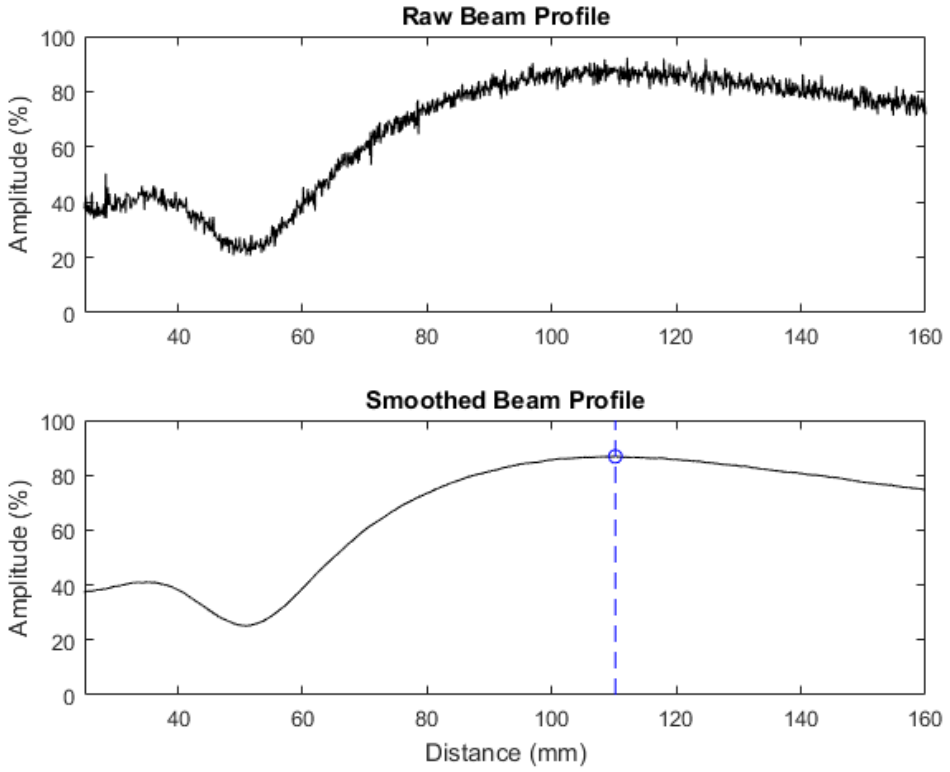

Figure A.29. Raw sound beam profile (top) and filtered (bottom) of Transducer #4.

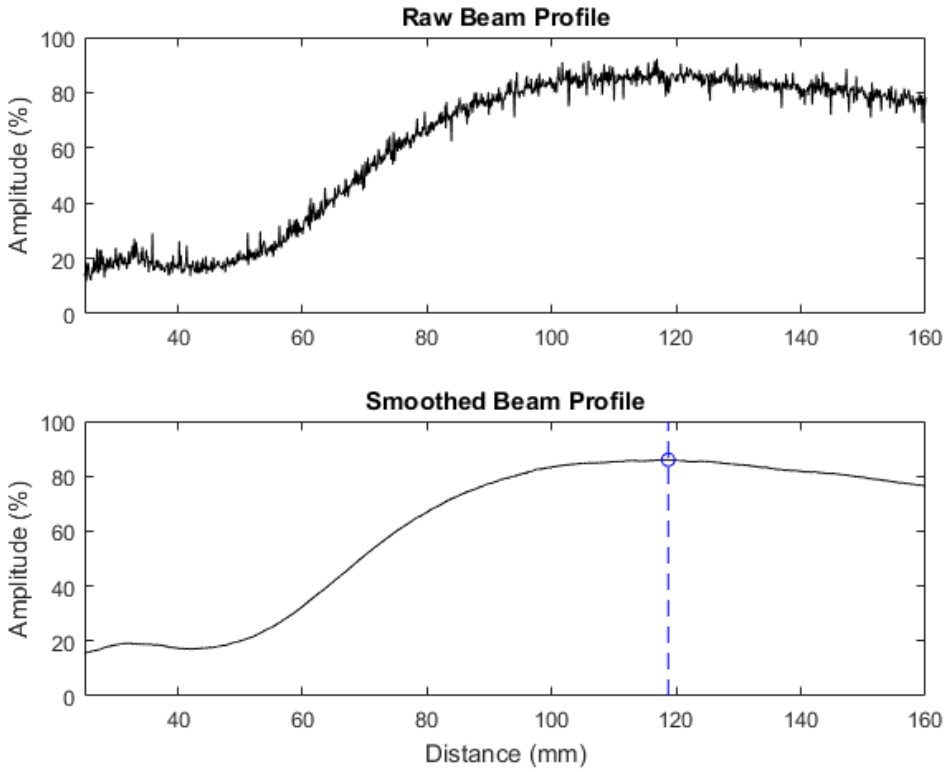

Figure A.30. Raw sound beam profile (top) and filtered (bottom) of Transducer #5.

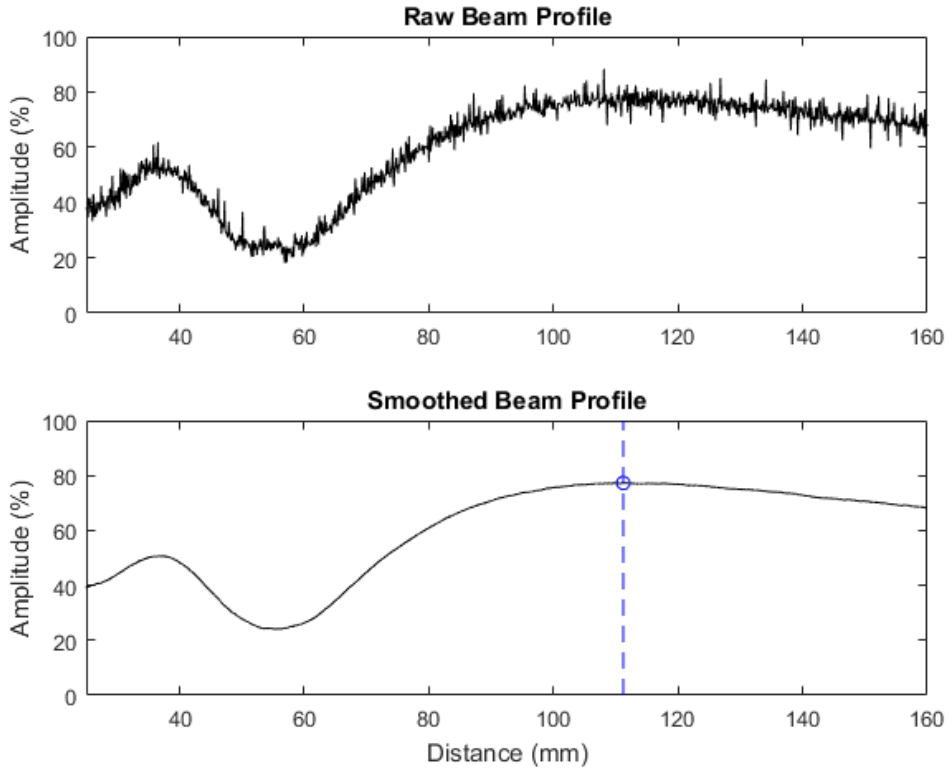

Figure A.31. Raw sound beam profile (top) and filtered (bottom) of Transducer #6.

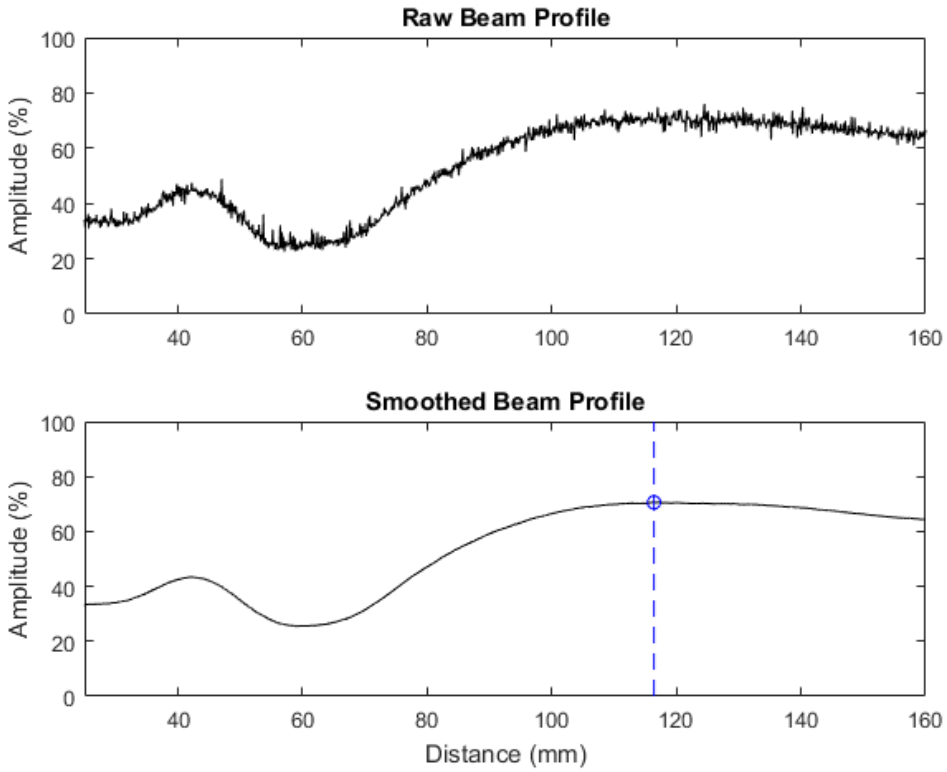

Figure A.32. Raw sound beam profile (top) and filtered (bottom) of Transducer #7.

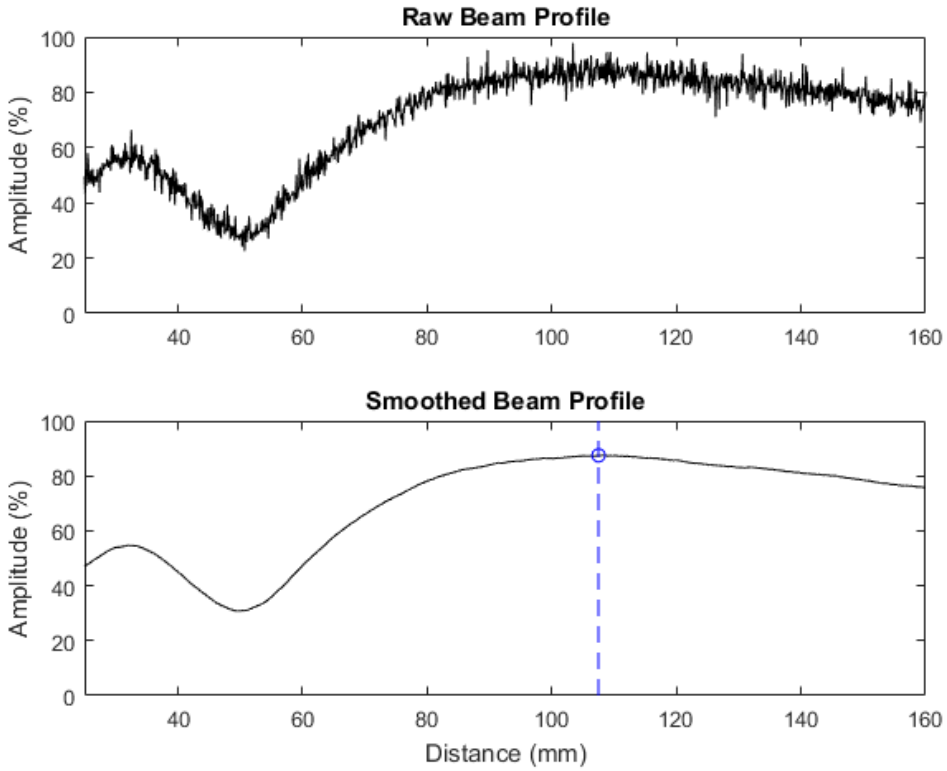

Figure A.33. Raw sound beam profile (top) and filtered (bottom) of Transducer #8.

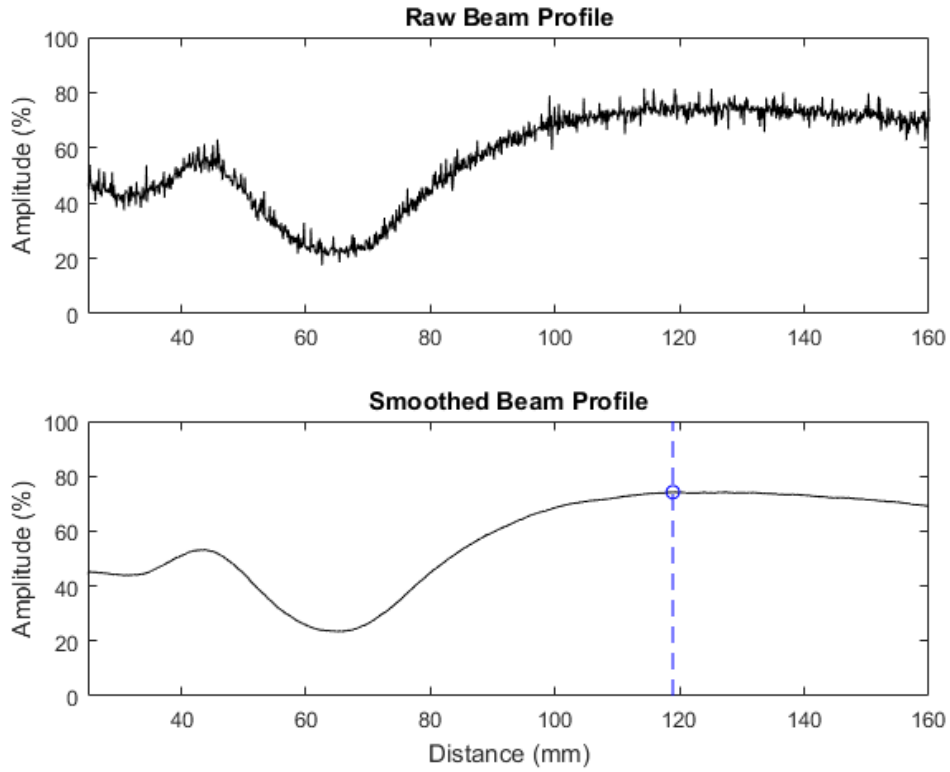

Figure A.34. Raw sound beam profile (top) and filtered (bottom) of Transducer #9.

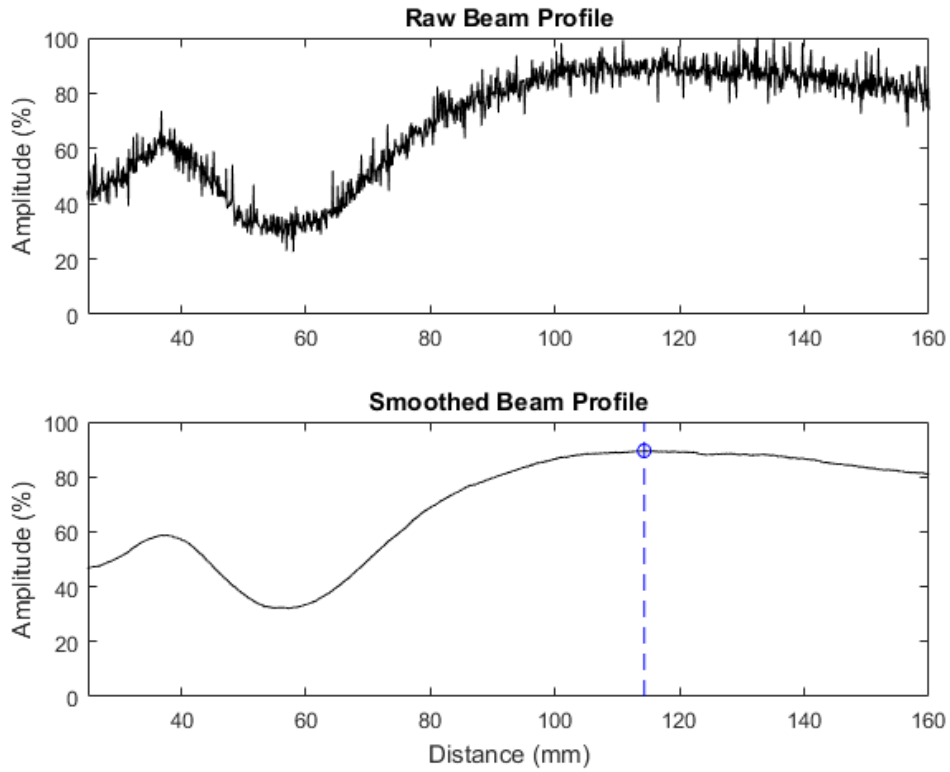

Figure A.35. Raw sound beam profile (top) and filtered (bottom) of Transducer #10.

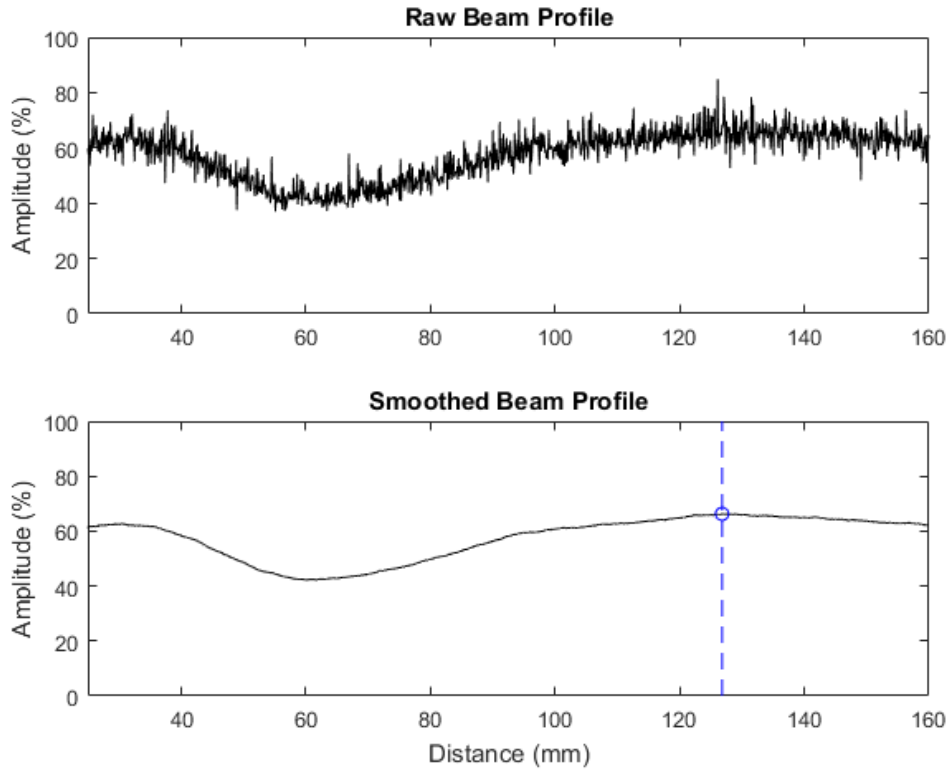

Figure A.36. Raw sound beam profile (top) and filtered (bottom) of Transducer #11.

A.4 Beam Face Maps

The soft gain of each face map was adjusted so that the peak signal was 100% full-screen-height. Altering the gain in this manner caused the noise background levels differ from image to image because the transducers emitted at different signal intensities. Each image is 16 mm x 16 mm (0.63 in. x 0.63 in.).

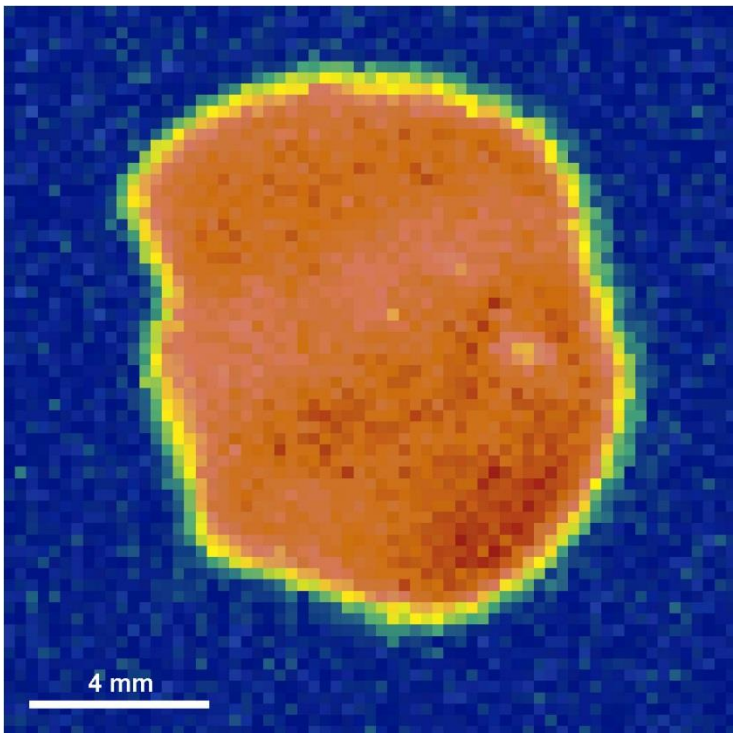

Figure A.37. Probe face scan of Transducer #2.

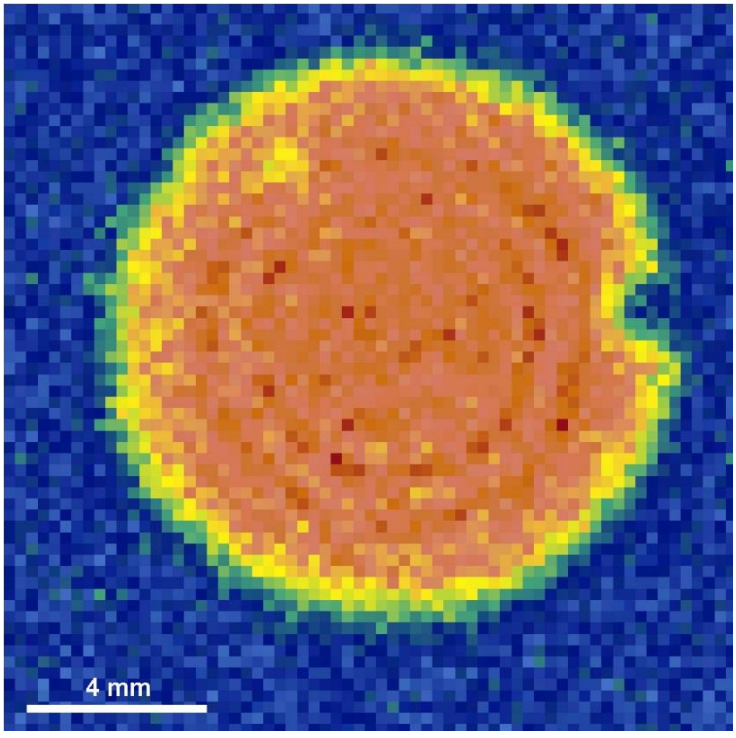

Figure A.38. Probe face scan of Transducer #3.

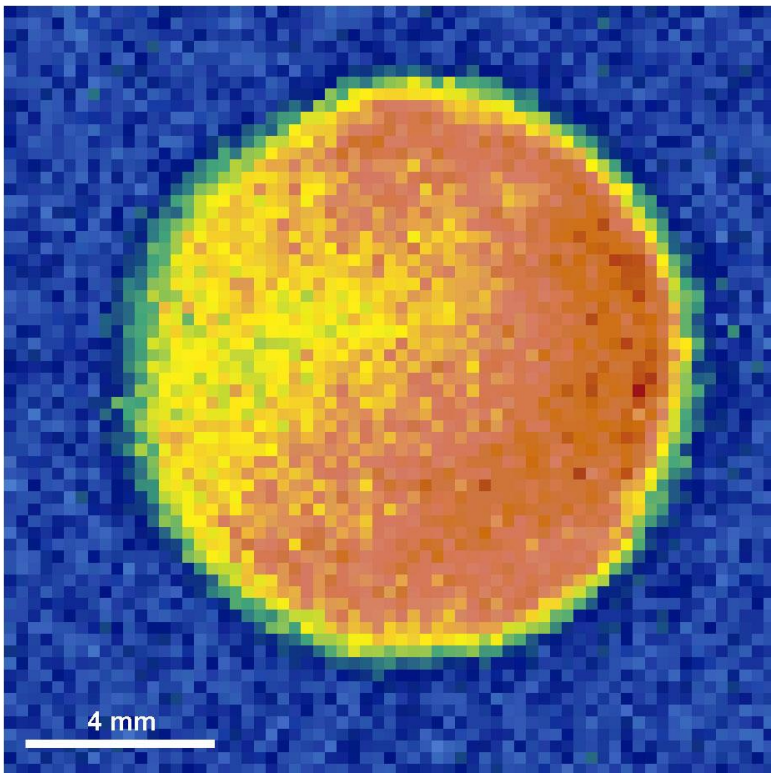

Figure A.39. Probe face scan of Transducer #4.

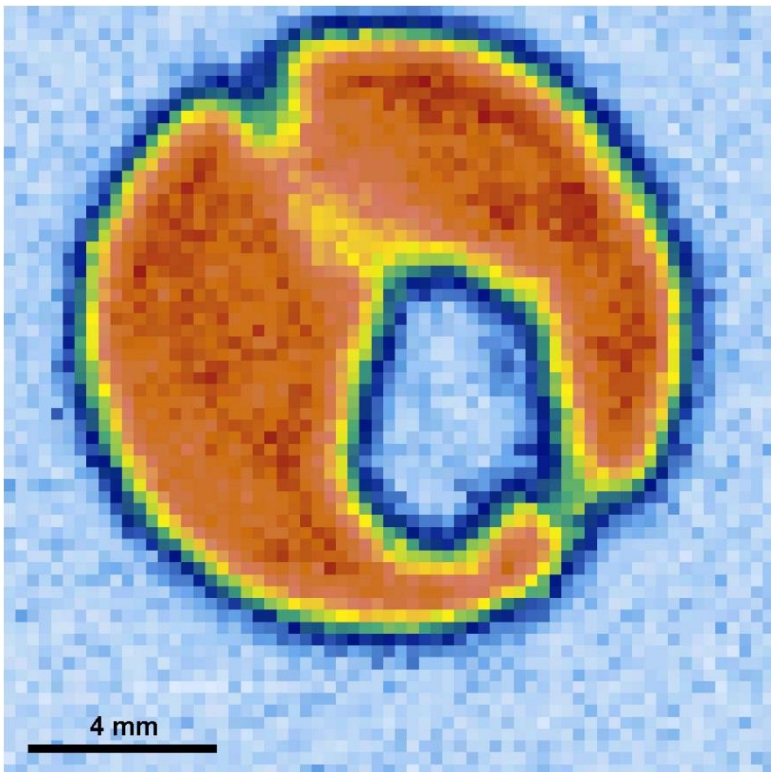

Figure A.40. Probe face scan of Transducer #5.

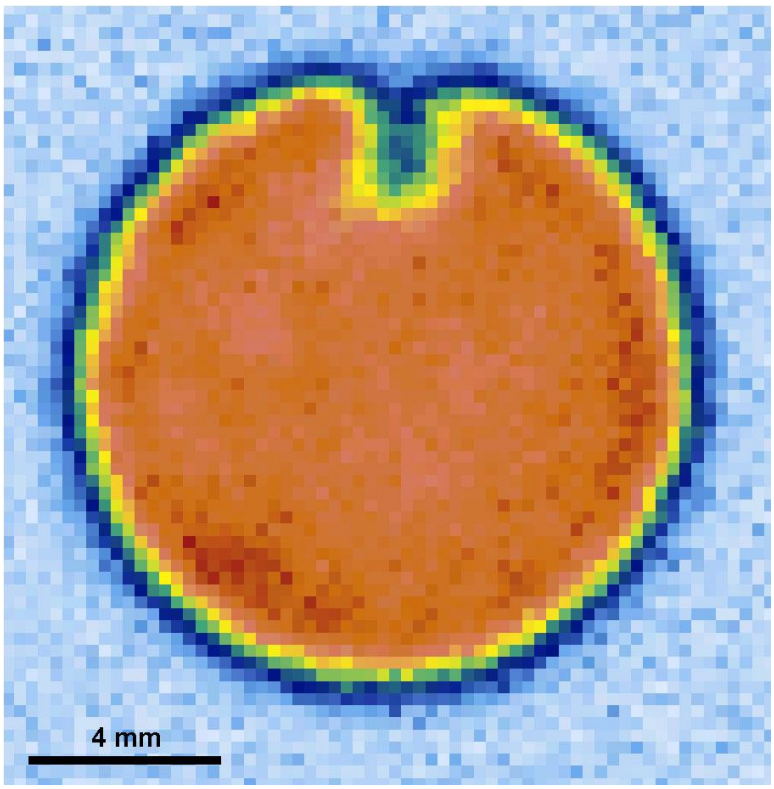

Figure A.41. Probe face scan of Transducer #7.

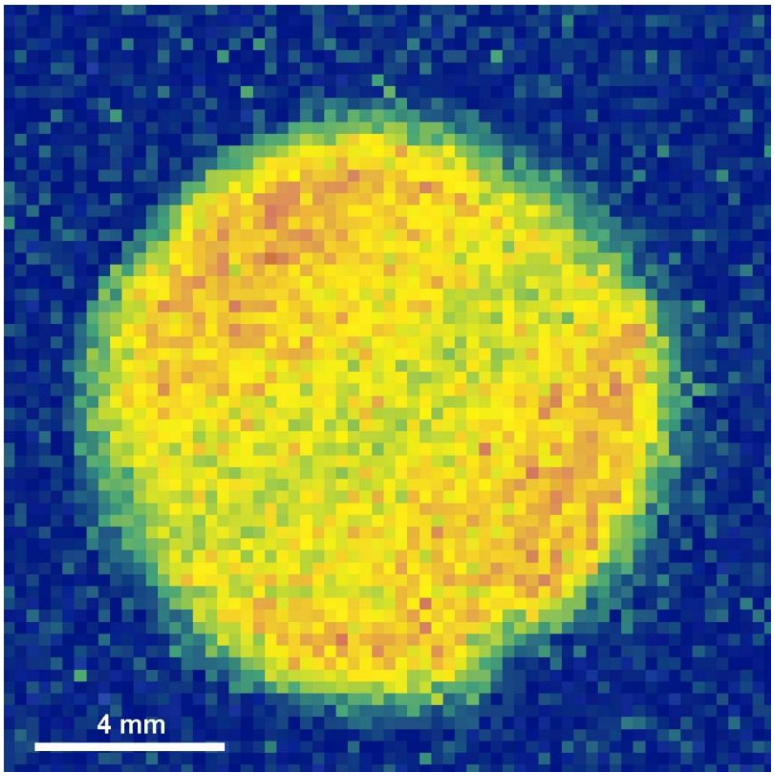

Figure A.42. Probe face scan of Transducer #8.

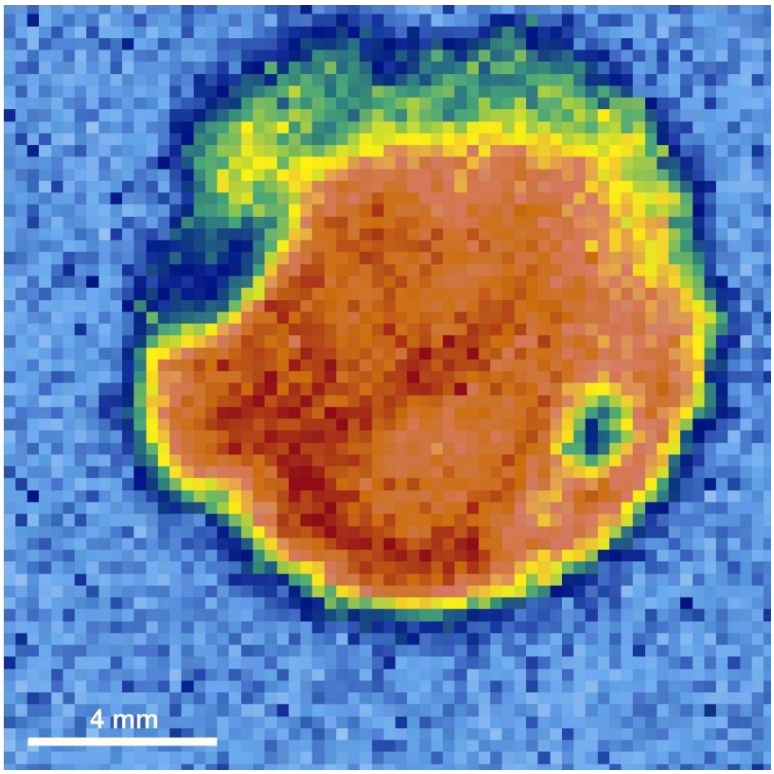

Figure A.43. Probe face scan of Transducer #11.

A.5 Beam Profile Mapping Evaluation – CIVA

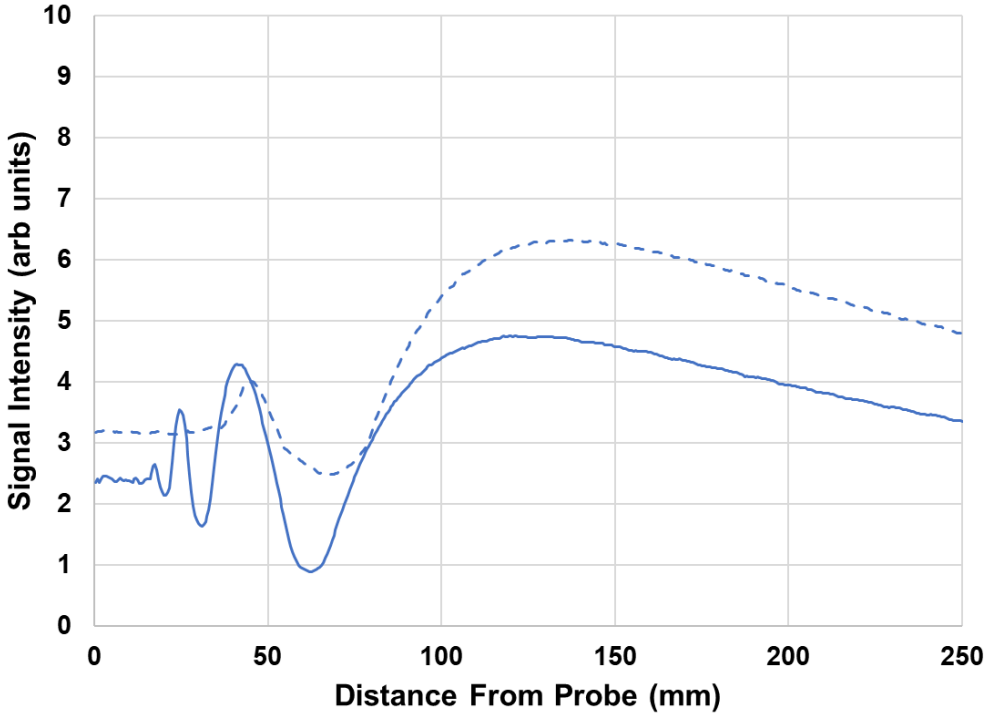

Figure A.44. Solid line: Beam profile generated in CIVA for Transducer #2. Dashed line: Beam profile generated in CIVA for the nominal transducer.

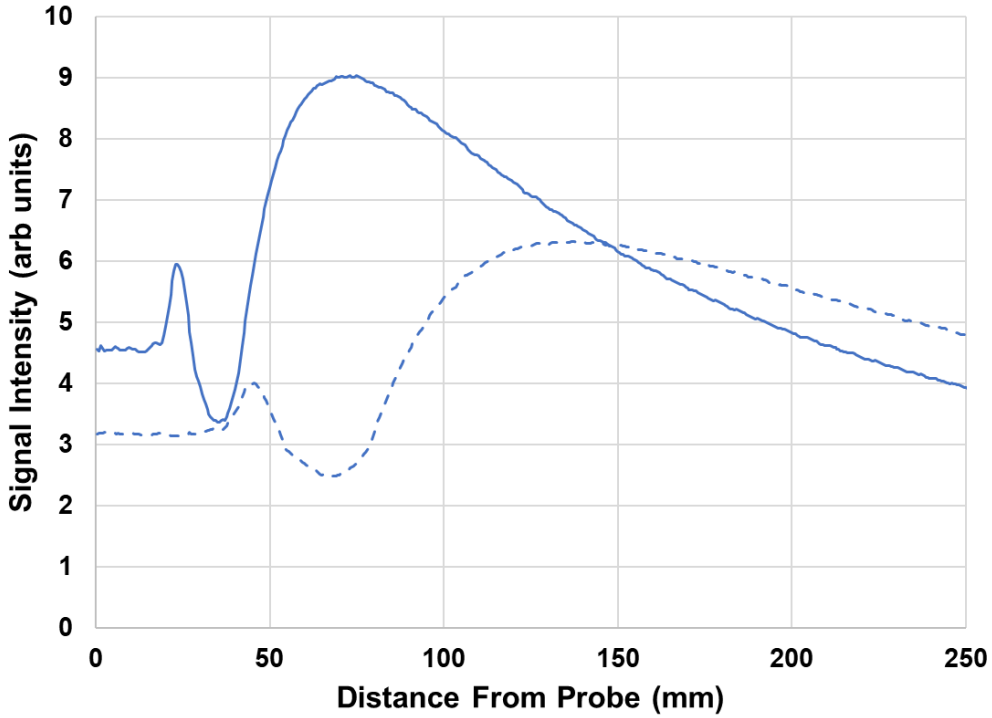

Figure A.45. Solid line: Beam profile generated in CIVA for Transducer #3. Dashed line: Beam profile generated in CIVA for the nominal transducer.

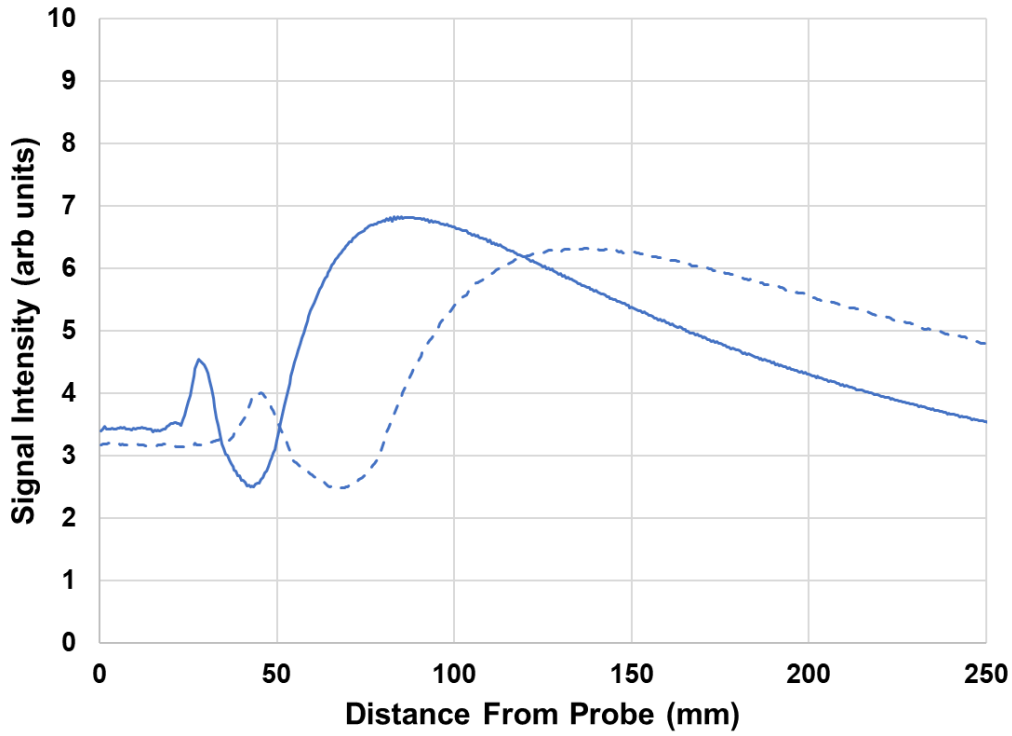

Figure A.46. Solid line: Beam profile generated in CIVA for Transducer #4. Dashed line: Beam profile generated in CIVA for the nominal transducer.

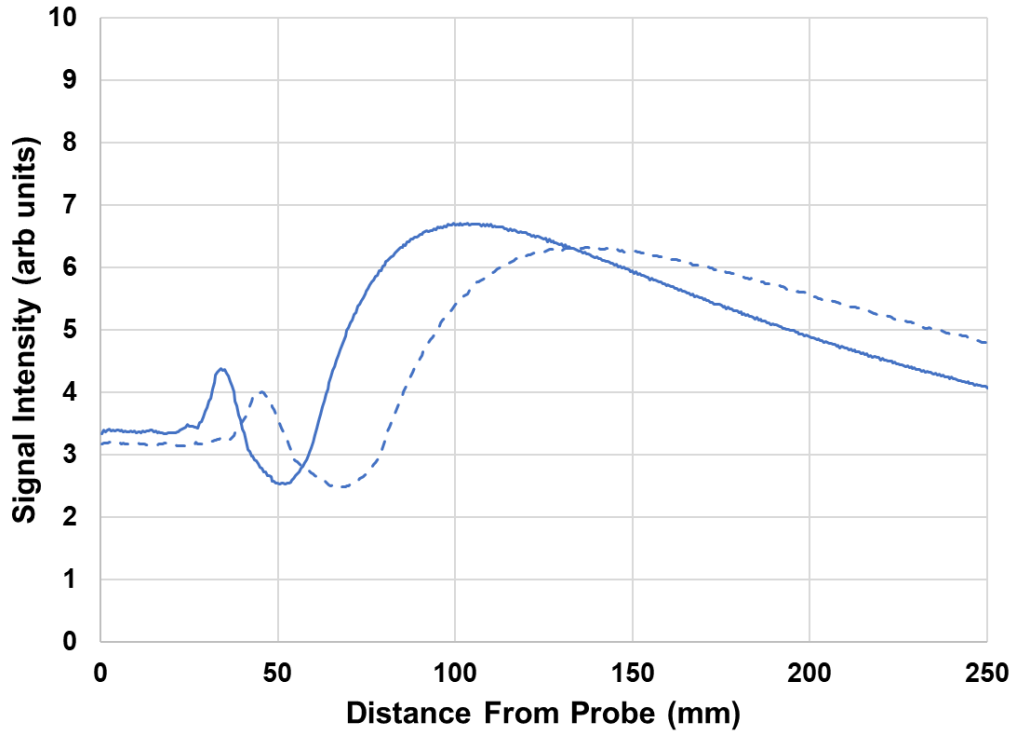

Figure A.47. Solid line: Beam profile generated in CIVA for Transducer #5. Dashed line: Beam profile generated in CIVA for the nominal transducer.

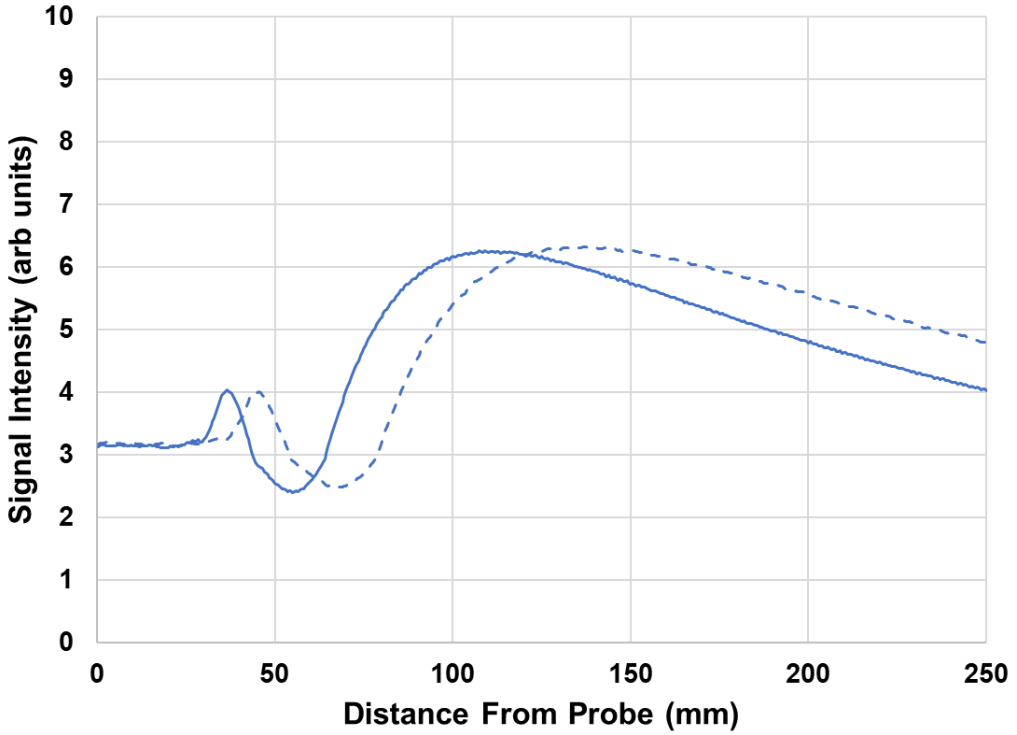

Figure A.48. Solid line: Beam profile generated in CIVA for Transducer #7. Dashed line: Beam profile generated in CIVA for the nominal transducer.

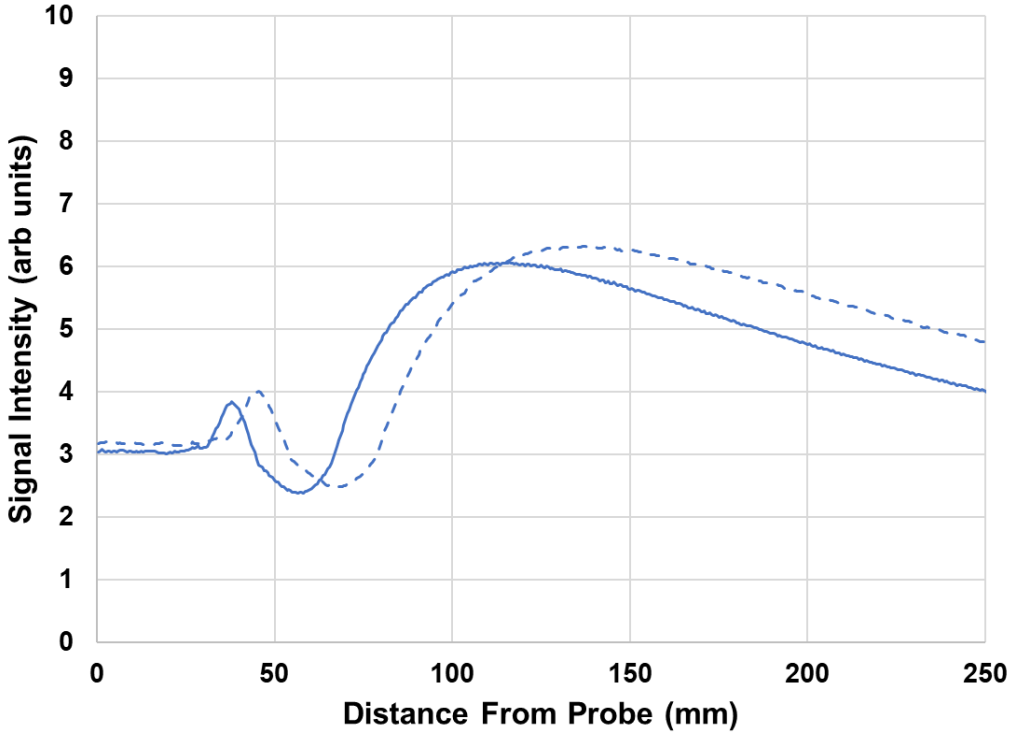

Figure A.49. Solid line: Beam profile generated in CIVA for Transducer #8. Dashed line: Beam profile generated in CIVA for the nominal transducer.

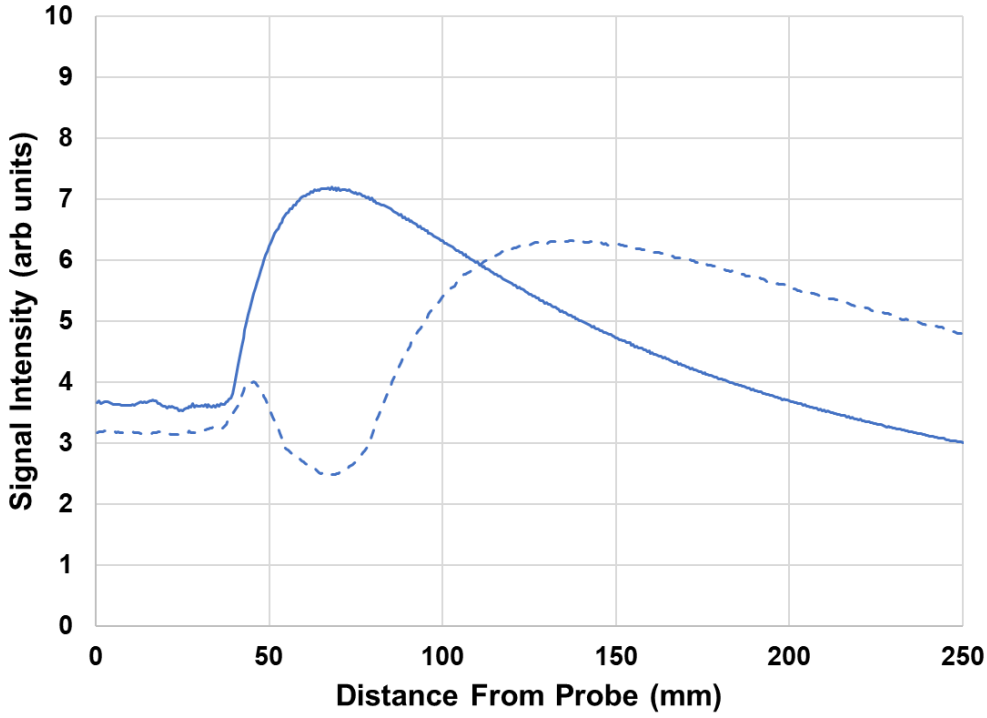

Figure A.50. Solid line: Beam profile generated in CIVA for Transducer #11. Dashed line: Beam profile generated in CIVA for the nominal transducer.

Pacific Northwest
NATIONAL LABORATORY

Proudly Operated by **Battelle** *Since 1965*

902 Battelle Boulevard
P.O. Box 999
Richland, WA 99352
1-888-375-PNNL (7665)

www.pnnl.gov

Prepared for the U.S. Nuclear Regulatory Commission
under a Related Services Agreement with the U.S. Department of Energy
CONTRACT DE-AC05-76RL01830

U.S. DEPARTMENT OF
ENERGY